Isolated propeller aeroacoustics at positive and negative thrust
Author links open overlay panel

Isolated Propeller Aeroacoustics at Positive and Negative Thrust

Jatinder Goyal*[,a], Francesco Avallone†[,b], Tomas Sinnige‡[,a]
[a] *Delft University of Technology, Kluyverweg 1, Delft 2629 HS, The Netherlands*
[b] *Politecnico di Torino, Corso Duca degli Abruzzi 24, Torino 10129, Italy*

Using propellers in negative thrust conditions can potentially result in many benefits, such as a steeper descent, a reduced landing run, reduced community noise, energy regeneration, etc. However, the aerodynamics and aeroacoustics of propellers in this regime are not well understood. This paper presents an aeroacoustic analysis of an isolated propeller operating in both positive and negative thrust conditions, using scale-resolved lattice-Boltzmann very large eddy simulations and the Ffowcs Williams & Hawkings analogy. The propeller was operated at a constant tip Mach number so that any differences in tonal noise between positive and negative thrust conditions were due to changes in blade loading. Results showed that the flow separation around the blades in the negative thrust case led to a 2 to 6 times higher standard deviation in integrated thrust compared to the positive thrust case. The blade loading in the negative thrust case shows the amplitude of fluctuations up to 18% for inboard sections and up to 30% near the blade tip compared to the time-averaged loads. The noise in the propeller plane is 10 dB higher in the positive thrust regime than in the negative thrust regime at a given absolute thrust level of $|T_C| = 0.08$. The lower noise at negative thrust is caused by two factors: the lower magnitude of the negative torque compared to the positive torque at a given thrust level and the shift of the blade loading inboard in the negative thrust condition due to the stall of the blade tip. Along the propeller axis, the negative thrust regime has 13-15 dB higher noise because of the increased broadband noise generated by the flow separation. In the negative thrust case, the noise along the propeller axis (89 dB) and propeller plane (92 dB) are comparable. However, this is not the case for the propulsive case. The comparison of noise in the vicinity of the propeller plane showed that using the propellers in negative thrust conditions allows for a steeper and quieter descent compared to a conventional descent; as long as the magnitude of the negative torque produced is equal to or less than the torque required to operate the propeller in a conventional landing.

*PhD candidate, Wind Energy Section, Faculty of Aerospace Engineering; J.Goyal@tudelft.nl.
†Assistant professor, Department of Mechanical and Aerospace Engineering; francesco.avallone@polito.it.
‡Assistant professor, Flight Performance and Propulsion Section, Faculty of Aerospace Engineering; T.Sinnige@tudelft.nl.

Nomenclature

B	number of propeller blades
c	section chord, m
c_o	speed of sound in dry air at 15° C, m/s
c_d	$D'/q_\infty c$, sectional drag coefficient
C_f	τ_w/q_∞, skin-friction coefficient
c_l	$L'/q_\infty c$, sectional lift coefficient
C_P	$P/\rho_\infty n^3 D_\mathrm{p}^5$, propeller power coefficient
c_q	$Q'/\rho_\infty n^2 D_\mathrm{p}^4$, sectional torque coefficient
C_T	$T/\rho_\infty n^2 D_\mathrm{p}^4$, propeller thrust coefficient
c_t	$T'/\rho_\infty n^2 D_\mathrm{p}^3$, sectional thrust coefficient
C_{P_t}	total-pressure coefficient, $(p_\mathrm{t} - p_\infty)/q_\infty$
D	propeller diameter, m
D'	sectional drag force, N/m
f	frequency, Hz
J	V_∞/nD_p, propeller advance ratio
L'	sectional lift force, N/m
L/D	lift-to-drag ratio
M_ht	$\sqrt{M_\infty^2 + M_\mathrm{tip}^2}$, helicoidal tip rotational Mach number
M_rot	$\Omega r/c_\mathrm{o}$, local radial rotational Mach number
M_tip	$\Omega R/c_\mathrm{o}$, tip rotational Mach number
M_∞	Freestream Mach number
n	propeller rotation speed, Hz
P	propeller power, W
p	static pressure, Pa
P'_C	$P'/\rho_\infty V_\infty^3 D_\mathrm{p}$, sectional power coefficient based on freestream dynamic pressure
p_ref	reference sound pressure, Pa
p_t	total pressure, Pa
P_C	$P/\rho_\infty V_\infty^3 D_\mathrm{p}^2$, propeller power coefficient based on freestream dynamic pressure
Q	torque, Nm
q	$\rho V^2/2$, dynamic pressure, Pa
R	propeller radius, m
r	radial coordinate, m
Re_c	Reynolds number based on chord of the propeller blade
T	propeller thrust, N
t	section thickness, m
T'_C	$T'/\rho_\infty V_\infty^2 D_\mathrm{p}$, sectional thrust coefficient based on freestream dynamic pressure
T_C	$T/\rho_\infty V_\infty^2 D_\mathrm{p}^2$, propeller thrust coefficient based on freestream dynamic pressure
V_∞	freestream velocity, m/s
V_a	axial velocity, m/s
V_t	tangential velocity, m/s
V_eff	sectional effective velocity, m/s
x	Axial coordinate, m
y^+	dimensionless wall distance
BPF	$B \cdot n$, blade passing frequency, Hz
N	No. of elements on a VR level
OSPL	overall sound pressure level, dB
PSD	power spectrum density, dB/Hz

Greek Symbols

α	angle of attack, deg
$\beta_{0.7R}$	blade pitch angle at 70% of the radius, deg
η_p	TV_∞/P, propeller efficiency
η_t	P/TV_∞, turbine efficiency
Ω	$2\pi n$, rotational speed in rad/s
ϕ	phase angle, deg
ρ	air density, kg/m^3
σ	standard deviation

τ_w	wall shear stress, Pa	∞	freestream
θ	axial directivity angle, deg	FWH	Ffowcs Williams & Hawkings
Subscripts/Superscripts		HM	Hanson's model
$'$	per unit span		

I. Introduction

The increasing need for sustainable aviation has triggered many new technologies in the field of aviation. The use of fuel cells, hydrogen combustion, and electric architectures are a few examples of these technologies. These technologies are generally coupled with open rotors because of their high propulsive efficiency (up to moderate Mach number and at low cruise altitudes) [1] to increase the system's overall performance. One additional benefit of electric propulsion is that propellers can be operated at a negative thrust settings that can be beneficial for achieving steeper descent, reduced landing run, better maneuverability [2, 3], reduced community noise [4], and regeneration of energy.

A propeller can produce negative thrust by adjusting the blade pitch and/or the rotational speed so that angles of attack at the blade sections become such that negative lift is produced (figure 1). The generation of negative thrust is accompanied by the production of torque, which can be converted to electrical energy to power the electrical systems onboard. Pipistrel has already proven the feasibility of the concept by optimizing a propeller simultaneously for both propulsive and regenerative regimes, leading to 19% energy savings for a small electric trainer aircraft [5]. Though propellers operating at negative thrust were already investigated in 1933 and 1944 to study their effectiveness as aerodynamic brakes [2, 3], the concept did not gain much attention. It became relevant again with the advent of electric flight and its potential as a control device for the descent/landing phase.

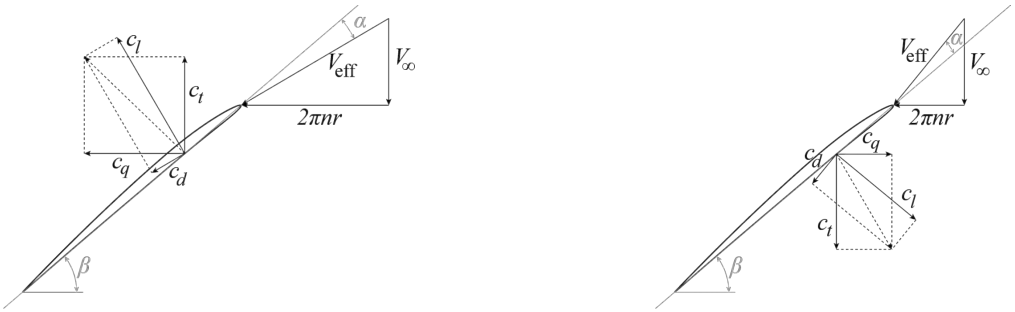

(a) Positive thrust mode **(b) Negative thrust mode**

Fig. 1 Velocity triangles at a fixed-pitch propeller blade section in positive and negative thrust modes [6]

For a typical aircraft configuration, the propeller design is expected to be dominated by the propulsive phases, i.e., climb and cruise. Therefore, operation in the negative thrust mode will represent an off-design condition. In previous papers [6–8], the aerodynamic phenomena of a conventional unducted propeller in the negative thrust regime have been investigated using RANS simulations and experiments. These studies have shown that negative thrust conditions lead to

almost fully separated flow around the blades of a conventional propeller. Due to limitations in terms of the extent of instrumentation, the experiments give limited information about the flow characteristics near the propeller blades and in the slipstream. Also, RANS simulations face difficulty in accurately predicting the flow separation due to the limitations of turbulence modeling [9, 10]. Therefore, higher-fidelity numerical simulations are needed to overcome these challenges. Such simulations can also provide information about the unsteadiness of the flowfield, which is expected to be relevant for aerodynamic and aeroacoustic interaction with a lifting surface immersed in the propeller slipstream.

Further, the literature on the aeroacoustics of propellers operating in the negative thrust regime is almost nonexistent. To the authors' best knowledge, only two studies [4, 7] exist that investigated the aeroacoustics of negative thrust propellers. In the ref. [4], the rotor aeroacoustics were not investigated in detail; instead, the main focus was the potential impact on community noise. In the ref. [7], only tonal noise characteristics were investigated using an analytical model (Hanson's model [11]), and no assessment was made for the broadband noise. As the propeller operates in the stall or near stall conditions in the negative thrust regime, it is expected that the relative importance of the tonal and broadband noise will change along with noise directivity and noise level compared to the propulsive regime. The flow separation on the blades could lead to a dominant broadband noise and even structural vibrations and associated structure-borne noise. However, no paper on these research gaps can be found in the literature.

This paper aims to investigate the aerodynamics and far-field acoustic characteristics of a conventional propeller operating in the negative thrust regime using lattice-Boltzmann (LB) very large-eddy simulations (VLES) coupled with the Ffowcs Williams and Hawkings (FWH) integral solution based on Farassat's formulation 1A [12]. The numerical setup has been validated using experimental data from ref. [8]. An analysis has been done at a constant freestream and tip rotation Mach number by varying propeller pitch to characterize the aerodynamics and aeroacoustics of the propeller at equal Mach number and Reynolds number in both positive and negative thrust regimes.

II. Computational Setup

The numerical setup was validated with the experimental data from ref. [8]. The data available from the experiments dictated the geometry and operating conditions used during the validation. For the subsequent analyses, the operational conditions were modified to be more similar to those experienced in free flight. The rotor geometry is given here first. Then, the methodology is explained, along with the computational setup.

A. Rotor Geometry

The rotor used in this study is TUD-XPROP, which is a scaled version of a propeller for a previous-generation regional turboprop aircraft. The rotor has a diameter of 0.4064 m and a hub diameter of 0.092 m. The nacelle of the rotor extended up to approximately $1.6D$ downstream. Originally, the propeller had six blades; however, only three

blades were used for this study due to limitations of the experimental facility [8]. The propeller can be seen in figure 2a along with its geometry parameters in figure 2b.

(a) Isolated propeller with three blades installed on a sting

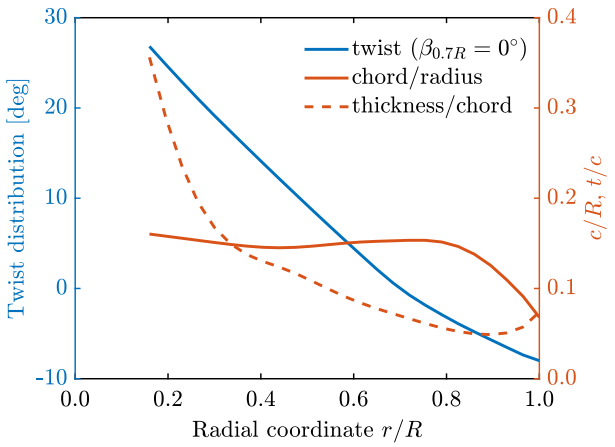

(b) Propeller blade geometry

Fig. 2 Propeller setup and geometry

B. Methodology

LB-VLES simulations have been chosen for this study for two main reasons. The first reason is the method's past proven record for capturing the tonal and broadband noise in similar applications [13, 14]. Secondly, due to the low dissipation and dispersion [15, 16], the LB-VLES simulations were deemed suitable for this study. A detailed description of the LBM can be found in the refs. [17] and [18]. For the simulations, the beta version of the commercial solver PowerFLOW 6-2021 by 3DS Simulia has been used, which has been introduced in ref. [19]. This beta version is especially suitable for the current application as it does not require a zig-zag trip to switch to the scale-resolving solver. Using a zig-zag trip can modify the flow separation and the broadband noise behavior [20, 21], which is relevant for this research and, therefore, a change in behavior due to the artificial introduction of turbulence is not desired. The volume of the domain is discretized using a Cartesian mesh. In total, 19 discrete velocities are used in three dimensions (D3Q19) for this study, including a third-order truncation of the Chapman-Enskog expansion. An explicit time integration approach is used to solve the equations at the Courant-Friedrichs-Lewy (CFL) number of 1 for stability. The particle distribution is obtained using a collision term based on a unique Galilean invariant [22], and equilibrium distribution of Maxwell-Boltzmann [23]. A very-large eddy simulation (VLES) model is implemented in PowerFLOW to take into account the effect of the subgrid unresolved scales of turbulence, which uses $k - \epsilon$ renormalization equations [24] to compute the turbulent relaxation time. The no-slip boundary condition on walls is approximated using a pressure-gradient extended wall model [25, 26]. The model is based on an extension of the generalized law-of-the-wall model [27] to take into account the effect of the pressure gradient on the boundary layer development.

A hybrid CFD/CAA approach has been used in this study to compute the far-field noise. Such an approach is an

ideal solution to avoid excessive computational costs related to resolving the propagation of acoustic waves to the far field. The FWH analogy was solved based on the forward-time solution [28] of Farassat's formulation 1A [12] using the post-processing software SIMULIA PowerACOUSTIC. This formulation includes surface integrals, i.e., acoustic monopoles (thickness noise) and dipoles (loading noise) terms. The volume integral, i.e., quadrupole term, is neglected in this formulation which accounts for the non-linear effects in the volume surrounding the integration surface. The quadrupole term was assumed to be negligible for the operating conditions considered in this paper as the convective Mach number of the propeller wake is less than 0.3 [29].

C. Computational Volume and Boundary Conditions

The computational domain is a cube with a domain size of $128D$ in all three directions (figure 3a). The boundary conditions were specified as a velocity inlet combined with a pressure outlet and slip walls. It was made sure that the total pressure profile was uniform at the inlet. Due to the large size of the domain, the impact of the boundary conditions on the solution is expected to be minimal. The no-slip condition was used for the propeller blades, spinner, and nacelle. For sliding mesh, a volume of revolution was defined around the propeller blades and spinner. In the radial direction, a clearance of $0.1R$ was defined between the blade tip and the outer edge of the rotating domain. Similarly, in the axial direction, a clearance of $0.05R$ was defined between the spinner edge and the edge of the rotating domain. In total, 13 variable resolution (VR) regions were used based on the ref. [30]. The cell volume changes by a factor of 8 between different VR regions. The finest three VR regions (VR13-11) were used around the propeller to accurately capture the flow around the propeller blades, as marked in figure 3b. VR10 was used in the sliding domain and downstream of the sliding domain up to $0.5R$. Further downstream, VR10 is used in a hollow cylinder to capture the strong gradients of tip vortices. VR9 was used in the cylinder encapsulating the propeller blades, spinner, and blade with a radius of $1.2R$ and extended $1R$ upstream and $3.5R$ downstream of the propeller. Other VR regions (1-8) were there to ensure that the domain was large enough to minimize any spurious acoustic reflections from the boundaries of the domain. Further, an acoustic sponge was used to absorb any remaining acoustic reflections coming from the boundaries by exponentially varying the kinematic viscosity per unit temperature from 0.005 $m^2/(s.K)$ at $15R$ up to 0.5 $m^2/(s.K)$ at $30R$ as shown in figure 3a. As the acoustic sponge starts at a $15R$ distance from the propeller, its effect on the aerodynamic results is assumed to be minimal.

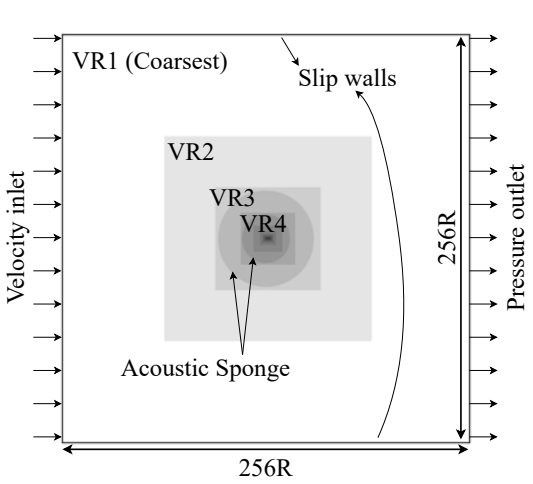

(a) Full computational domain

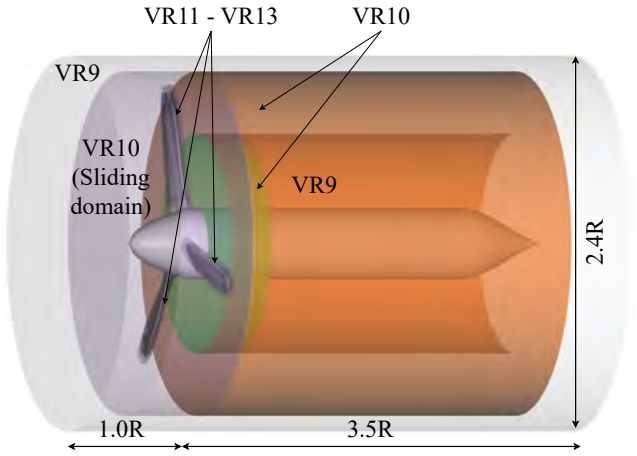

(b) Zoomed view of domain showing the distribution of VR regions near the propeller

Fig. 3 Computational domain and boundary conditions along with the VR regions

III. Grid Dependence Study and Comparison with Experiments

For the grid dependence study, two operating conditions have been chosen with a pitch angle of 15° at $0.7R$ of the blade, for which extensive experimental data were available for validation [8]. The two conditions were chosen as the most challenging ones to reproduce numerically. The first one is a positive thrust condition with a moderate thrust at an advance ratio (J) of 0.60. The given pitch angle is not optimal for propulsive operation and leads to separation near the trailing edge [7]. Therefore, if the grid results are converged for such an operating condition, it can be safely assumed to be converged for other positive thrust conditions with fully attached flow. However, the grid convergence in the positive thrust regime does not ensure the convergence in the negative thrust regime because of significant flow separation around the blades in that condition[6, 7]. The second condition is the negative thrust condition at $J = 1.10$, close to the maximum power output point. The details of these operating conditions can be found in table 1.

Table 1 Operating conditions for grid dependence study

J	V_∞ [m/s]	n [Hz]	M_{ht}	max Re_c
0.60	30	123.03	0.47	3.5×10^5
1.10	30	67.11	0.27	2.0×10^5

Five different grids were compared for the grid dependence study with fine equivalent voxels varying from 1 million to 100 million, based on the previous study by Avallone et al. [30]. The fine equivalent elements represent the number of elements (N) weighted by the time stepping rate, which is proportional to the mesh resolution level (VR level) and is

calculated as follows:

$$\text{Fine equivalent} = \frac{\text{N(finest scale)}}{2^0} + \frac{\text{N(2nd finest scale)}}{2^1} + \frac{\text{N(3rd finest scale)}}{2^2} + ... + \frac{\text{N(coarsest)}}{2^{\text{(n grid levels-1)}}}$$

The details of the grids can be found in table 2, where resolution is defined as the number of fine equivalent voxels per characteristic length. The characteristic length is chosen to be chord at $0.7R$ blade span, which is approximately 31 mm.

Table 2 Grids used for the grid dependence study

		Positive thrust ($J = 0.60$)			Negative thrust ($J = 1.10$)		
Grid name	Grid label	Fine equivalent voxels	Resolution	$y^+_{0.7R,0.5c}$ (Front side)	Fine equivalent voxels	Resolution	$y^+_{0.7R,0.5c}$ (Front side)
very coarse	5	1,231,315	76	108	1,694,093	87	54
coarse	4	8,229,841	152	55	5,244,431	130	37
medium	3	26,780,737	228	34	23,134,459	217	22
fine	2	62,314,804	304	24	62,029,252	304	15
very fine	1	120,353,406	380	16	92,072,521	347	12

The setup was defined such that the blade-passing period of the propeller was an integral multiple of the time-step, which helps to avoid interpolation error in phase-locked and per-rotation averaged measurements. As the rotational speeds of the propeller are different at the chosen operating conditions, the chosen time-step is also different, resulting in a different resolution and mesh sizes. The flow was simulated for twelve revolutions for the medium grid (Grid 3) and used for seeding all the other resolutions. All the other resolutions were simulated for ten revolutions. For all the grids, the last eight revolutions were used for the measurements after ensuring that the transient period was over.

A. Convergence and Validation Study of Aerodynamic Properties

The integrated performance parameters, thrust coefficient C_T and power coefficient C_P, were used to verify the convergence of the integrated performance of the propeller and were compared with the experimental values. Further, the radial distributions of the time-averaged total pressure coefficient have been used to verify the convergence of the slipstream flowfield. Additional validation of the setup has been performed by comparing the phase-locked axial and tangential velocity fields in the slipstream with the experimental data.

1. Integral Performance Parameters

The figure 4 shows the C_T and C_P time-averaged over the last eight revolutions for the different grids compared to the experimental value. The uncertainty of the experimental data is indicated using the shaded areas around the mean results. The standard deviation of the simulated thrust values is also shown using the shaded areas with an averaging period of six revolutions to provide a measure of the load fluctuations over the averaged rotations. The trends of the grid-dependence study have been supported with the help of skin friction contours and shearlines along the blade surface shown in figure 5 for the fine grid (Grid 2). The streamlines are also shown around three blade sections at radial coordinates of $0.3R$, $0.6R$, and $0.9R$, respectively.

In the positive thrust condition shown in Figure 4a, the experimental thrust coefficient has an uncertainty of 2.5%, and the power coefficient has an uncertainty of 1.5%. The standard deviation of the simulated values is almost negligible, indicating the steadiness of the loads on the propeller blades. It is observed that C_T stays almost constant for Grid 4, Grid 3, and Grid 2 (coarse, medium, and fine, respectively). However, for Grid 1 (very fine), the thrust coefficient is increased by approximately 4% compared to Grid 2, 3, and 4. This trend can be explained as follows. As the propeller is operating at a comparatively low Reynolds number (3.5×10^5 based on the propeller chord at $0.7R$), a leading-edge separation bubble exists on both sides of the propeller blade as can be seen in figure 5a. The blade sections between $0.4R$ - $0.7R$ radial coordinate are on the verge of the trailing-edge separation on the pressure side, as indicated by the outward motion of shearlines at these locations. However, the prediction of the location of the separation bubble along the chord is very sensitive to the resolution of the boundary layer (y^+) besides the other parameters, such as incoming turbulence, surface roughness, and subgrid-scale modeling [31–34]. For such cases, having $y^+ \leq 1$ would be the ideal solution. However, as octree meshes are used in PowerFLOW, it becomes practically challenging to reach such y^+ values. Upto Grid 2, the y^+ values are greater than 20 on almost the whole blade surface on the suction side (front), see Table 2. However, the y^+ values are below 20 for Grid 1, which improves the prediction of laminar to turbulence transition [19], leading to a better thrust match with the experimental value for Grid 1 (very fine). The differences in the predicted trailing and leading edge separations along the blade span between different grids result in fluctuations in power coefficient (C_P) values between Grid 3, 2, and 1. The C_T predictions by LBM simulations are in good agreement with the experimental thrust for all the grids except Grid 5. However, the prediction of C_P is off by 10-11%., indicating that the drag is underpredicted by the LBM simulation leading to a low power value.

For the negative thrust condition shown in Figure 4b, the uncertainty in experimental measurements and the standard deviation of simulation values are less than 1%. The convergence of thrust and power is achieved for the fine grid (Grid 2) with 10% underprediction in thrust and 10% overprediction in power compared to the experiment. The significant difference in the simulated integrated performance compared to the experimental data comes from the fact that there is a leading-edge separation bubble on the suction side (back) around the blade sections starting from the root until the radial coordinate of $0.85R$, see figure 5b. Further outboard, the blade sections are fully separated. It is known from literature

[31–34] that even the separation-bubble length is very sensitive to subgrid-scale modeling and grid quality, making it extremely difficult to capture this condition accurately in the numerical simulation. Moreover, the low Reynolds number in this operating condition (2.0×10^5 based on the propeller chord at $0.7R$) results in a trailing-edge separation on the pressure side (front) of the propeller blade. As there is a significant difference in the extent of flow separation between the two regimes (figure 5), Grid 2 was considered good enough to understand the relative change in aerodynamic and aeroacoustic characteristics between the positive and negative thrust regimes.

The slipstream characteristics have been compared with the experimental data in the next subsection to scrutinize further the results obtained from LBM simulations. The very coarse grid (Grid 5) has been omitted in further comparisons to keep the discussion clear and concise.

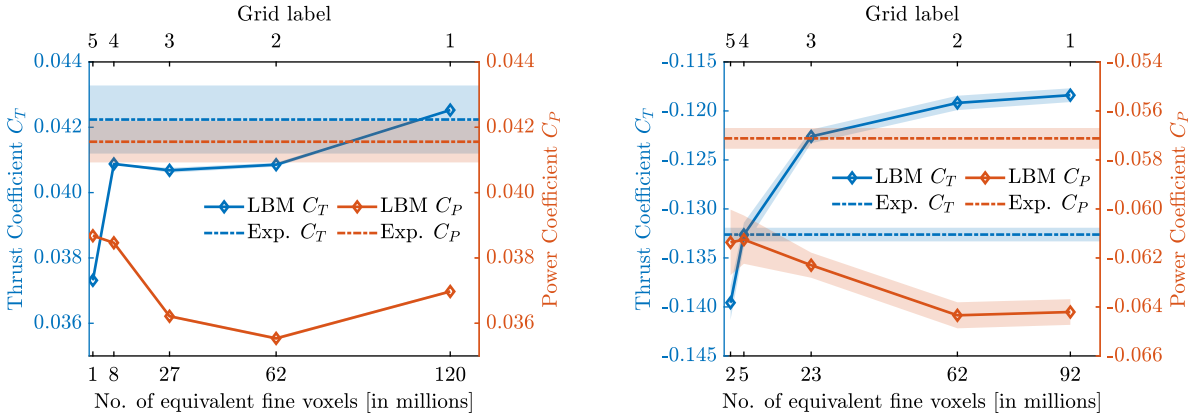

(a) Positive thrust condition (J = 0.60) **(b) Negative thrust condition (J = 1.10)**

Fig. 4 Effect of mesh refinement on the predicted integrated thrust and power

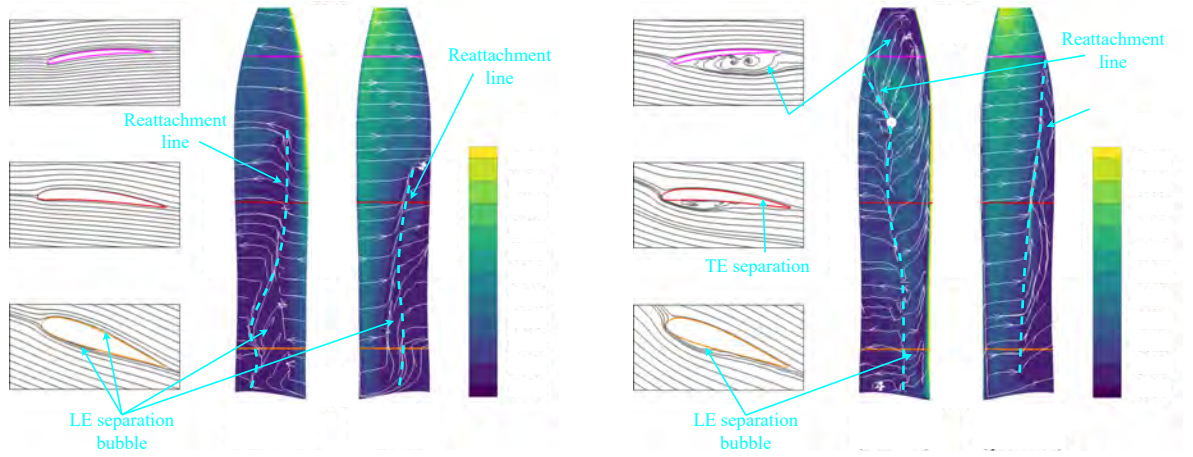

(a) Positive thrust Condition (J = 0.60) **(b) Negative thrust Condition (J = 1.10)**

Fig. 5 Visualization of flow around the propeller blade using skin friction coefficient and shear lines (fine grid)

2. Slipstream

The radial distributions of the time-averaged total pressure coefficient obtained from LBM simulations in the slipstream at $0.15R$ downstream of the propeller (figure 6) have been compared with the experimental data [8] to evaluate the validity of LBM simulations. For $J = 0.60$ in figure 6a, The total pressure coefficient profile is similar for different grids except between the radial coordinate of $0.5R$ - $0.7R$. Besides the fluctuating peak values at the radial coordinate of $0.6R$ between different grids, the medium grid shows different radial gradients between $0.5R$ to $0.6R$. This is expected to be a consequence of the presence of a leading-edge separation bubble along with the trailing-edge separation onset as shown in figure 5a. At this operating condition, the blade tip is negatively loaded due to local negative angles of attack (figure 6a), as explained by ref. [8]. The experimental data shows a negative total pressure coefficient for $0.92 \leq r/R \leq 1$. However, in the simulations, the total pressure coefficient is negative only between $0.98 \leq r/R \leq 1$, resulting in a lower power requirement for a given thrust. The simulations underestimate the maximum value of the total pressure distribution, which is offset by overestimation in the outboard sections, resulting in a thrust value close to the experimental value. Thus the blade loading distribution obtained from the simulations is expected to differ from that obtained in the experiments.

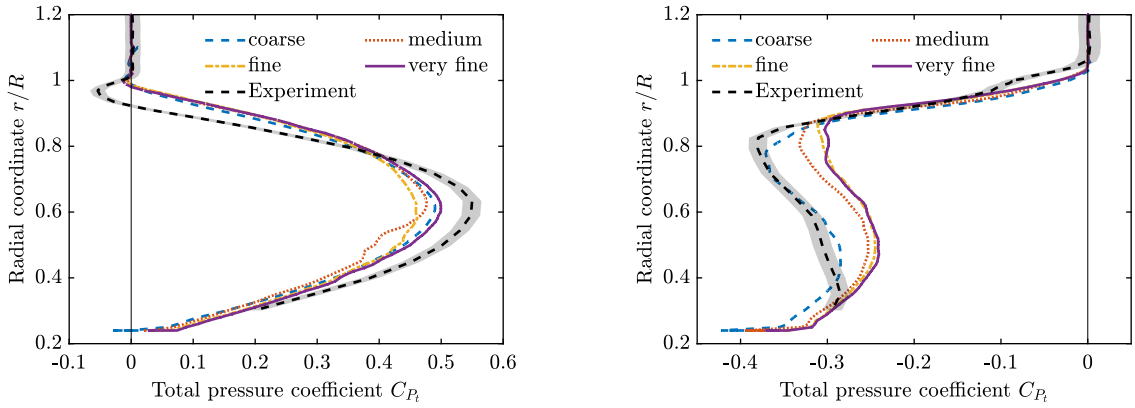

(a) Positive thrust condition ($J = 0.60$) **(b) Negative thrust condition ($J = 1.10$)**

Fig. 6 Radial distributions of time-averaged total pressure coefficient at $0.15R$ downstream of the propeller centre

Figure 6b shows the time-averaged total pressure profile for the negative thrust condition ($J = 1.10$). Looking at the convergence behavior, it is evident that the slipstream converges to a similar profile for fine and very fine grids. Except near the root (below the radial coordinate of $0.4R$), the total pressure distributions are similar in terms of gradients in the radial direction between simulations and experiments. Quantitatively, the total pressure distribution over the 10% most outboard blade radius matches with the experiment. At 40%-90% of blade radius, there is an overprediction of the total pressure, which agrees with the underprediction of the negative thrust observed in figure 4b. As the blade tip is completely separated (figure 5b), it is comparatively easier to predict in numerical simulations than a separated region

with reattachment. It results in a good agreement for the outboard blade span for all the grids. However, the blade span between the root and the radial coordinate of $0.85R$ has separation at the leading edge with reattachment near the trailing edge. As the reattachment location is sensitive to the grid, it results in differences between the simulation and the experiment [31–34]. The gradients of total pressure coefficient profiles in the radial direction are almost insensitive to the choice of the considered grids for both positive and negative thrust regimes, except for the medium grid between $0.5R$ - $0.6R$ for the positive thrust condition. Based on these comparisons, the fine grid was considered a good choice for this study and has been used for further comparison with the phase-locked PIV data [8].

The simulated phase-locked axial and tangential velocity fields have been compared with particle image velocimetry (PIV) data at 0° phase angle (ϕ) with respect to the propeller blade. The definition of the phase angle is shown in figure 7. Figure 8 and 9 show the comparison of phase-locked axial and tangential velocities for the positive ($J = 0.60$) and negative thrust condition ($J = 1.10$), respectively. In these figures, the contours of axial and tangential velocity components in the slipstream of the propeller are shown on the right part of the figure, along with the radial line plots at three different axial locations shown on the left. The contours on the top are obtained from PIV data, while those on the bottom are obtained from the current numerical simulations. The first radial line is close to the propeller blades ($x/R = 0.10$) for both operating conditions. The remaining two axial positions have been chosen such that one cuts the tip vortex, and the other is between two tip vortices. These radial lines are located at $x/R = 0.37$ and 0.60 for positive thrust and at $x/R = 0.40$ and 0.70 for negative thrust. The chosen axial positions are different between the two operating conditions due to their different advance ratios leading to a different pitch between the tip vortices (i.e., different helix angles of the slipstream).

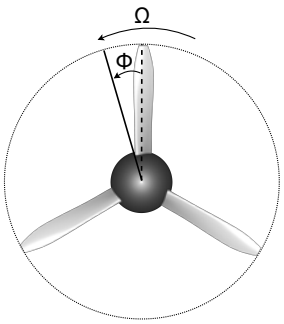

Fig. 7 Definition of phase angle (ϕ)

In figures 8a and 8b, the velocity gradients near the tip vortices are larger in LBM simulations compared to the PIV data, and the tip vortices are shifted slightly outwards in the LBM results compared to the PIV data. These differences could originate from the slightly different blade loading. Such differences would lead to a difference in the local velocity in the slipstream, which means that the flow structures would also convect downstream at different velocities. Since the contours are shown at a fixed streamwise position in figures 8a and 8b, their position relative to the flow structures would

differ, resulting in a relatively large offset in induced velocities. Other reasons could be a possible uncertainty in the blade position or minor inaccuracies in the calibration of the PIV setup leading to a slight displacement of the data with respect to the actual physical coordinates. The line plots show that the gradients in the radial direction are adequately captured by LBM simulations, though the peak is slightly underpredicted, which is consistent with observations from figure 6.

Figure 9 shows the same comparison for the negative thrust condition. The edge of the slipstream is at a higher radial coordinate in the LBM results compared to the PIV data, as seen in the contours and the left-down corner line plot ($x/R = 0.7$). Again the gradients in the radial direction from the LBM data are in agreement with the PIV data. LBM simulations overpredict the peak of phase-locked axial velocity compared to experiments at $x/R = 0.1$ (figure 9a), which contradicts the time-averaged total pressure profile seen in figure 6b and the time-averaged axial velocity results shown in figure 10a. This apparent inconsistency is suspected to be a consequence of uncertainty in the phase-locked blade position in the experiment. To validate this hypothesis, a new comparison with the phase-locked PIV data at $x/R = 0.1$ is shown with arbitrary phase angles of 1°, 2°, and 5° in figure 10b. The LBM simulation no longer overpredicts the peak at $x/R = 0.1$; instead, there is an underprediction that agrees with figure 10a, supporting the validity of the hypothesis.

Based on the comparison of the total pressure coefficient and axial and tangential velocities in the propeller slipstream, it has been proven that the fine grid (Grid 2) is able to predict the slipstream characteristics in terms of gradients in the radial and axial direction. Thus the fine grid is deemed suitable for the further comparison of the aerodynamic characteristics of the positive and negative thrust regimes.

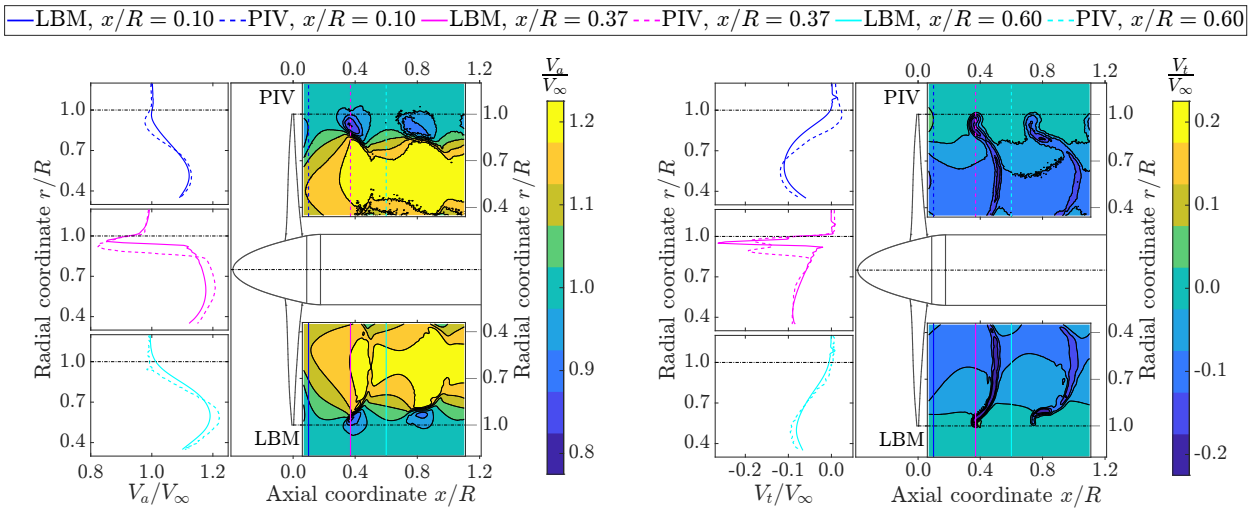

(a) Axial velocity **(b) Tangential velocity**

Fig. 8 Comparison of the phase-locked slipstream from PIV data and LBM simulations for the positive thrust condition at $\phi = 0°$ ($J = 0.60$, fine grid)

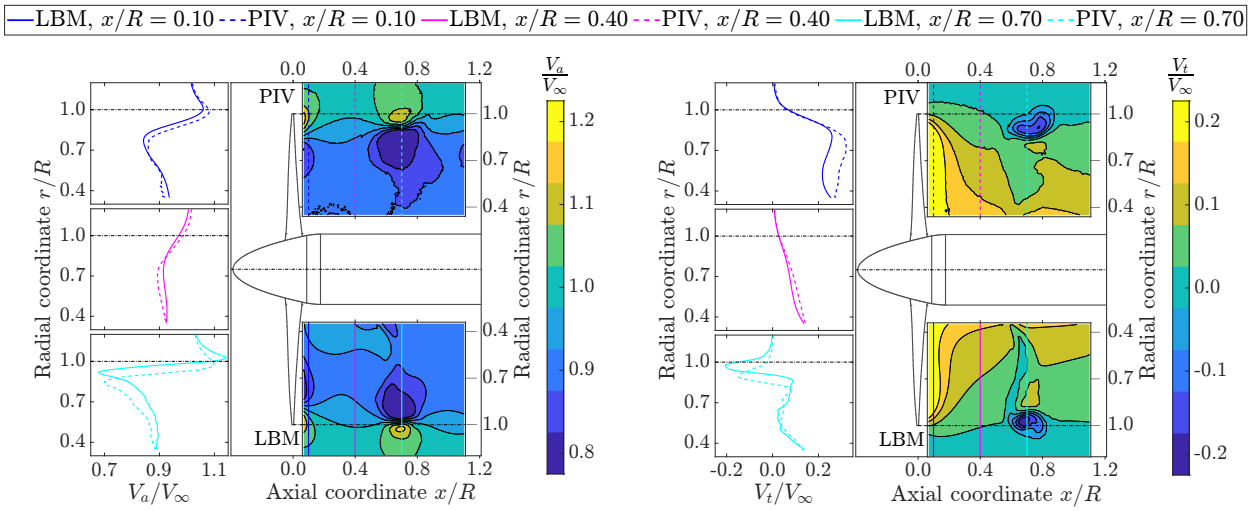

(a) Axial velocity **(b) Tangential velocity**

Fig. 9 Comparison of the phase-locked slipstream from PIV data and LBM simulations for the negative thrust condition at $\phi = 0°$ ($J = 1.10$, fine grid)

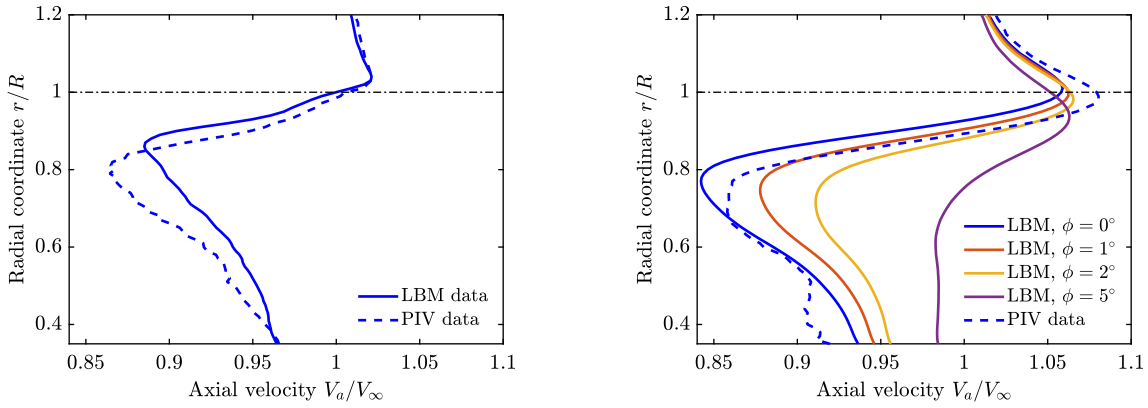

(a) Time-averaged **(b) Phase-locked**

Fig. 10 Time-averaged and phase-locked axial velocity profile at $x/R = 0.10$ for the negative thrust condition ($J = 1.10$, fine grid)

B. Convergence Study of Far-field Aeroacoustics

As the dominant noise sources are anticipated to be within the first 10 BPFs [35], the aeroacoustic convergence has been determined by comparing the directivity patterns of overall sound pressure level (OSPL) for the range of 0.5 - 10 BPF. As LBM simulations work with a cartesian mesh, the three blades of the propeller have different discretization resulting in a different blade loading. This difference was up to ±4% for the positive thrust condition ($J = 0.60$) compared to the blade-averaged loading and up to ±1% for the negative thrust condition ($J = 1.10$). This difference in the blade loading leads to tonal noise at a frequency of (1/3) times the BPF in the power spectrum density (figure 12b); therefore, the lowest frequency is chosen to be 0.5 BPF to eliminate the contribution from this numerical noise source.

The OSPL was calculated using the FWH analogy on a ring with a radius of $20R$, with the axis aligned with the propeller plane and the center coinciding with the propeller center to ensure that the observer is in the far field. The OSPL directivity patterns for both configurations are shown in figure 11. The trends are shown for half of the ring ($\theta = 0^\circ - 180^\circ$) because of the axisymmetric inflow condition, where $\theta = 0^\circ$ lies along the propeller axis in front of the propeller and $\theta = 90^\circ$ lies in the propeller plane. Additionally, the power spectrum density (PSD) is shown for the fine grid (Grid 2) in figure 12 for two locations - propeller plane ($\theta = 90^\circ$) and propeller axis ($\theta = 0^\circ$).

For the positive thrust condition (figure 11a), the OSPL between 45° and 150° is almost identical between the different grids with differences below 1 dB as a consequence of similar blade loading along the blade span. For the negative thrust condition (figure 11b), the difference in OSPL for different grids is below 1 dB at all the directivity angles except the coarse grid. In the propeller plane, tonal noise is the most dominant noise source, as seen in figure 12b. Since there are minute differences in blade loading between different grids, as previously shown in figure 6, the match of OSPL levels in the propeller plane between different grids is an expected trend. In the propeller plane, the first three BPFs are dominant for the positive thrust condition compared to only the first BPF in the negative thrust condition; see figure 12b. The 1/3 BPF caused by the different meshing of the three blades of the propeller is about 25-30 dB lower than the first BPF and thus did not affect the interpretation of the aeroacoustic results.

The broadband noise is expected to be the most dominant source along the propeller axis [35], which is indeed the case (figure 12a) for the given operating conditions. In the positive thrust condition, the main sources of broadband noise are expected to be trailing-edge noise and vortex shedding due to flow separation (figure 5a). The prediction of broadband noise levels is sensitive to the resolution of the relevant turbulent scales. The coarse grid does not sufficiently resolve these turbulent scales, resulting in low (broadband) noise along the propeller axis. However, the medium and the other grids are fine enough to capture these effects, as visible in OSPL levels. The OSPL increases from the medium to the fine grid due to the better resolution of the turbulence on the latter. A further refinement in the grid results in a decrease of 3 dB along the propeller axis from the fine grid to the very fine grid. Therefore, there is an oscillatory convergence. For noise along the propeller axis, prediction within 3 dB is considered enough for this study. Flow separation is the main source of broadband noise for the negative thrust condition. Due to strong flow separation in this condition (figure 5b), the turbulent scales are expected to be larger than for the positive thrust case. The medium and finer grids predict similar noise levels along the propeller axis with differences below 1 dB.

In the positive thrust condition, the noise in the propeller plane is about 12 dB higher than the noise along the propeller axis, which is an expected trend for conventional operation. However, the trend is reversed for the negative thrust condition, i.e., the noise along the propeller axis is 11-12 dB higher than the noise in the propeller plane. This change in directivity is because of two reasons: a) the flow separation in the negative thrust condition significantly increases the broadband noise compared to the positive thrust condition (4-7 dB along the propeller axis); b) lower tonal noise in the negative thrust condition compared to the positive thrust condition (20 dB in the propeller plane), because

of the lower blade-tip rotational Mach number and the lower absolute blade loading.

From the above comparisons, it is observed that the fine grid (Grid 2) is able to determine the changes in the noise source characteristics between the positive and negative thrust regimes. Hence, it is considered good enough for further analysis.

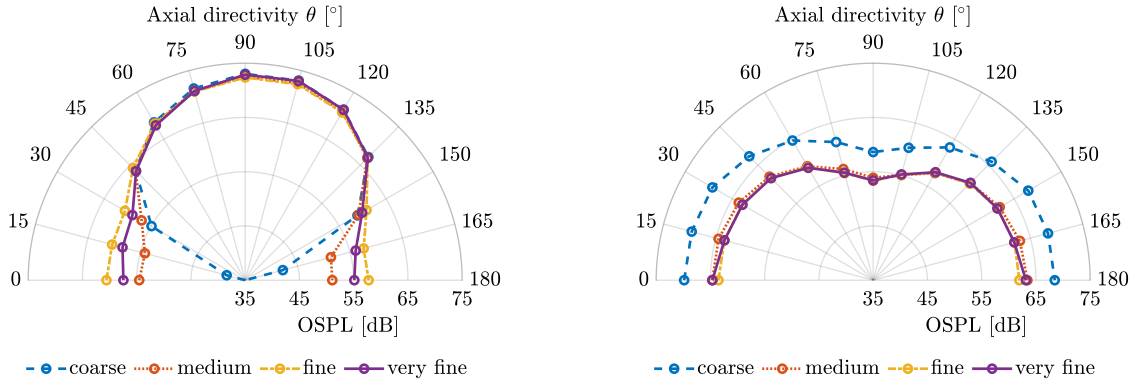

(a) Positive thrust condition (J = 0.60) **(b) Negative thrust condition (J = 1.10)**

Fig. 11 Effect of different grids on the OSPL directivity patterns

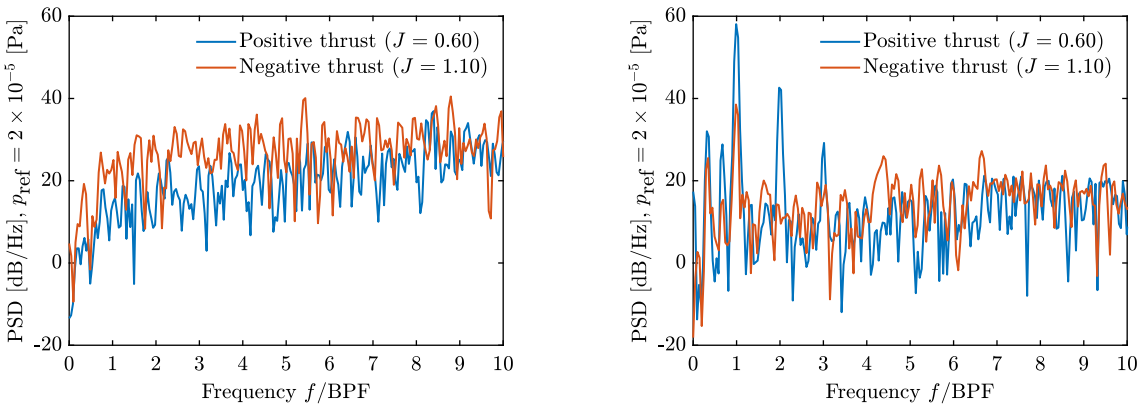

(a) Upstream along propeller axis (θ = 0°) **(b) Propeller plane (θ = 90°)**

Fig. 12 Power spectrum density at θ = 0 and 90° for positive thrust and negative thrust conditions (fine grid)

IV. Results

A propeller operating at a constant speed was used to study the far-field aeroacoustics of the negative thrust regime compared to the conventional positive thrust regime. Given the constant helical tip Mach number, the thickness noise does not change between the operational modes; therefore, it is easier to identify the changes in various noise sources due to the change in thrust and power (both direction and magnitude). The operational conditions were chosen based on a preliminary mission analysis of an ATR-42 aircraft with a relatively steep descent (5.5°). The resulting freestream Mach

number was 0.29. The helicoidal tip Mach number was set to 0.74 to achieve reasonable similarity with a full-scale turboprop propeller. For this study, the simulations were performed at 0° angle of attack with respect to the propeller so that there was no periodic unsteady loading on the blades. In a realistic configuration, this would be an additional noise source. However, it was decided to eliminate this noise source in this study for ease of interpretation of the results. The pitch angle of the blade was changed from 10° to 45° with a step of 5° to vary the propeller loading. As the propeller is operated at a fixed advance ratio, there was only a single operating point at which the propeller operated at its peak efficiency for the selected advance ratio. However, this was deemed acceptable because a difference in tip Mach number would affect the comparison more significantly than the obtained differences in propeller efficiency. An additional pitch setting with $\beta_{0.7R} = 37.57°$ was evaluated to match the absolute thrust obtained at $\beta_{0.7R} = 20°$, which has been used to evaluate the changes in noise sources due to the change in the operating regime (negative to positive thrust condition). The choice of $\beta_{0.7R} = 20°$ as the reference for comparing the two regimes at an absolute thrust level was based on the earlier-mentioned preliminary mission analysis of an ATR-42 aircraft.

A. Aerodynamic Performance

Figure 13 shows the differences in the instantaneous flow features around the propeller blades between the positive and negative thrust regimes for $T_C = \pm 0.08$ at 37.57° and 20° pitch settings respectively. These figures show the skin friction coefficient contours and shearlines at the blade surface for the two conditions. In addition, streamlines are shown around three blade sections located at $0.3R$, $0.6R$, and $0.9R$. Figure 13a shows that the flow is attached along the whole blade span on the back side of the propeller for $T_C = +0.08$, except for the inboard sections that exhibit the presence of a separation bubble. The front side of the propeller shows a separation bubble at the mid-chord position, which can also be seen in the streamlines around the $0.3R$ blade section. This separation bubble is present from the root until around $0.35R$ and moves towards the trailing edge with increasing radial coordinate. For the blade sections present outboard of $0.35R$, the separation bubble extends up to the trailing edge resulting in trailing-edge separation as seen in the streamlines around the blade sections at $0.6R$ and $0.9R$.

For the negative thrust condition ($T_C = -0.08$), the flow is attached on the front (pressure) side of the propeller, except near the trailing edge on the inboard sections (around $0.5R$- $0.8R$), see figure 13b. There is a trailing edge separation at these blade sections, as also indicated by the streamlines around the $0.6R$ blade section. On the back side of the propeller, the flow is attached only for a small portion of the chord near the leading edge, as indicated by the separation line. This leading-edge separation is a consequence of the operation of the blade sections at high negative angles of attack (as shown using streamlines around $0.3R$, $0.6R$ and 0.9). This trend is consistent with previous studies [6, 7].

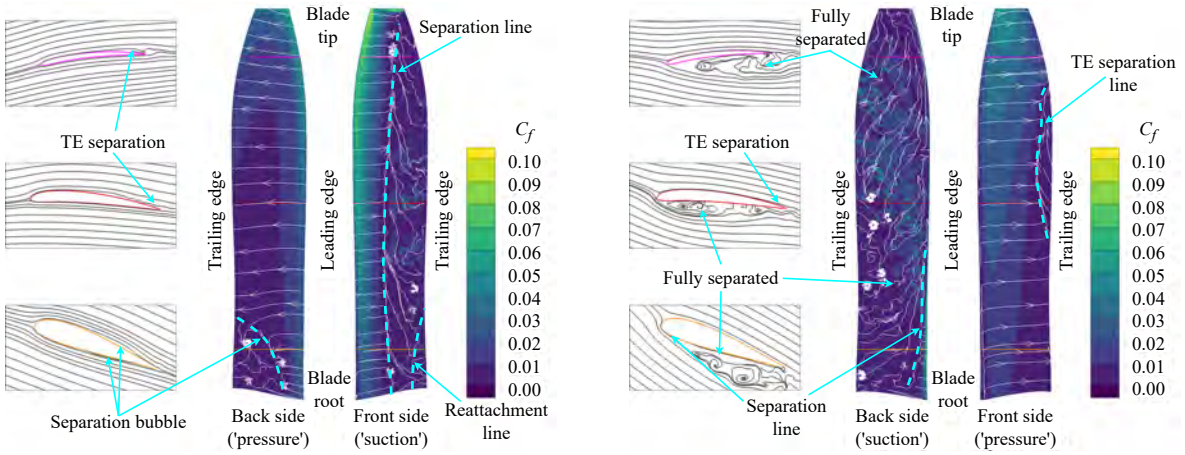

(a) $T_C = +0.08, \beta_{0.7R} = 37.57°$ **(b) $T_C = -0.08, \beta_{0.7R} = 20.00°$**

Fig. 13 Visualization of instantaneous flow around the propeller blade using skin friction coefficient and shear lines for $T_C = \pm 0.08$

1. Time-Averaged Performance Analysis

Figure 14 shows the effect of the varying pitch on the propeller performance. As the advance ratio and freestream Mach number are constant for the analysis, the inflow angle is also constant (31.4° at $r/R = 0.7$, ignoring induction), see figure 15. Therefore, the lower the pitch angle, the more negative the angle of attack (AoA). Similarly, the higher the pitch angle, the higher the AoA. For the pitch angles up to 30°, the blade section at $r/R = 0.7$ operates at negative angles of attack. As the pitch angle is increased from 10° to 30°, the negative angles of attack at blade sections are reduced, which in turn reduces drag and negative lift. As both lift and drag contribute to the negative thrust, a monotonic trend of T_C is seen in figure 14a. On the other hand, the negative power magnitude is reduced by reducing the negative lift and increased by reducing the drag. The opposite nature of these effects results in a maximum power obtainable at a certain pitch for a given operating condition, around 15° in this case, as shown in figure 14a. The transition from negative to positive power occurs around 27.5° (figure 14a). In the positive thrust regime, the drag component opposes the lift component in the thrust direction, whereas both components contribute positively to the power. As the pitch is increased from 30° to 45°, the positive angles of attack increase at the blade sections, increasing lift and drag. Therefore, a monotonic trend is obtained for power in the positive thrust regime. As the flow is still attached around most of the blade for the considered operating conditions (figure 13a), the increase in lift is more than the increase in drag, resulting in an increase of T_C with the increase in pitch angle.

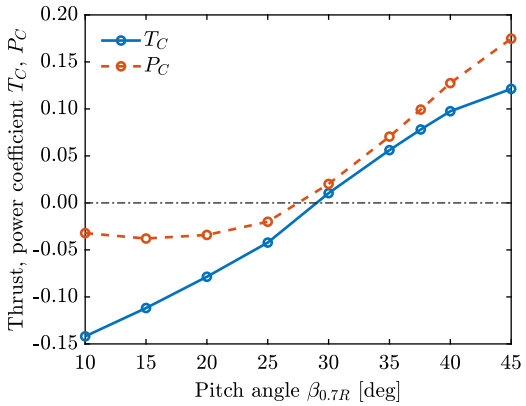

(a) Effect of pitch setting on thrust and power coefficient

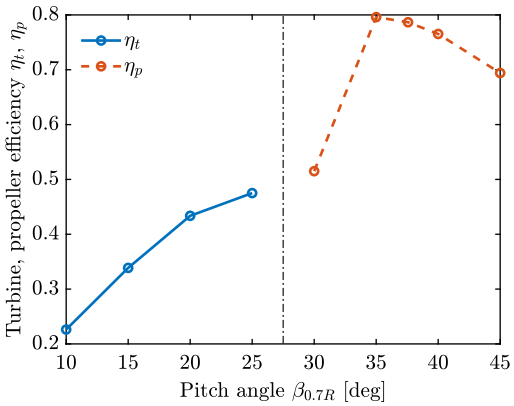

(b) Effect of pitch setting on turbine and propeller efficiency

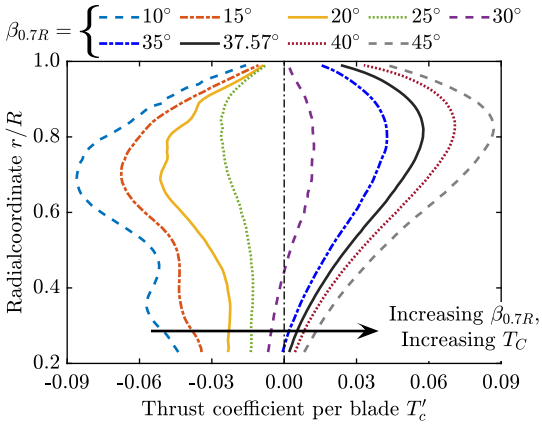

(c) Thrust distribution along the blade span

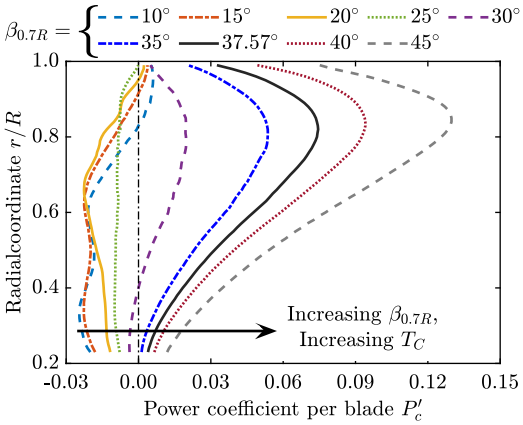

(d) Power distribution along the blade span

Fig. 14 Effect of pitch change on propeller performance at $M_\infty = 0.29$, $M_{ht} = 0.74$ (Time-averaged)

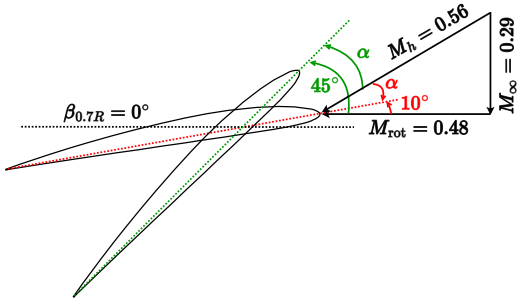

Fig. 15 Velocity triangle for the constant operating condition at different pitch settings at $r/R = 0.7$ (ignoring induction)

Figure 14b shows the variation in the efficiency of the propeller as a function of the pitch setting. Different definitions of efficiency are used for the positive and negative power regimes. The turbine efficiency (η_t), the inverse of the propeller efficiency, has been used for the negative thrust regime. It relates to the shaft power regenerated per unit of negative-propulsive power (TV_∞) produced, while the propeller efficiency (η_p) relates to the propulsive power (TV_∞)

produced per unit of shaft power consumed. A higher turbine efficiency does not necessarily mean higher absolute power regeneration, which can be observed in the current case. The 25° pitch setting gives the highest turbine efficiency (figure 14b), while the 15° pitch setting results in maximum negative power magnitude (figure 14a). At the 25° pitch setting, the flow is still attached on the inboard part of the blade and is separated only on the outboard part. However, as the pitch angle is reduced to 20°, the flow is separated around a larger part of the blade span, resulting in a larger drag increase compared to the lift increase. This results in a larger increase in the negative thrust magnitude compared to the increase in the negative power magnitude resulting in reduced turbine efficiency. As the pitch angle is reduced even further, there is no increase in the regenerated power; however, there is a significant increase in the negative thrust, further steepening the turbine efficiency slope. At 30° pitch, the propeller operates at a very inefficient positive thrust condition due to inboard sections operating in the negative thrust regime (figure 14c). As the pitch angle is increased to 35°, the propeller efficiency increases significantly (80%). With the further increase of pitch angle, the blade sections operate at higher loading and a sub-optimal L/D ratio, especially at 45° pitch, where the efficiency drops to 69%.

The thrust distribution along the blade span in figure 14c shows that the inboard part of the blade has a higher loading in the negative thrust regime than the positive thrust regime. The higher loading near the root is a consequence of higher absolute AoA at negative thrust conditions leading to higher lift and drag. The loading peak is around a radial coordinate of $0.7R$ in the negative thrust operations, in contrast to the positive thrust regime, where the maximum is around $0.85R$. The flow separation around the blade tip shifts the peak inwards in the negative thrust regime; that is why the loading peak is located around $0.8R$ at 25° pitch, which shifts to $0.7R$ at 10° with the increase in flow separation. A local maximum is observed in the thrust distribution around $0.45R$ for the 10° and 15° pitch settings. The local lift magnitude in the negative thrust cases is negatively influenced by the flow separation (reduced Cl) and positively influenced by the increasing dynamic pressure with the increasing radial coordinate. Around $0.45R$, the decrease in the lift due to the flow separation is more than the corresponding increase in dynamic pressure due to the increasing rotational speed with the increasing radial coordinate. Though the drag also adds to the negative thrust magnitude, the major contribution comes from the lift (around 80%). Therefore, the local decrease in the lift magnitude results in a local maximum in the thrust distribution at the radial coordinate of $0.45R$ for 10° and 15° deg pitch settings seen in the figure 14c. The loading distribution for the 30° pitch setting shows that the inboard part of the blade operates in the negative thrust regime with AoA lower than the zero lift AoA. In contrast, the outboard part of the blade operates in the positive thrust regime with AoA higher than the zero lift AoA, resulting in a small positive thrust and power overall.

Figure 14d shows the power distribution along the blade span for different pitch settings. For the positive thrust conditions, the radial loading distribution resembles that of a minimum-induced loss design, with a peak around a radial coordinate of $0.85R$. For the negative thrust conditions, a completely different distribution is obtained where most of the contribution comes from the inboard section with a relatively flat distribution up to the radial coordinate of $0.6R$. The power at outboard sections drops to zero and even goes to positive values at the tip. The positive power at the

tip, along with the negative thrust, indicates that the tip is separated to the extent that the power is consumed by that specific part of the blade (instead of being extracted from the flow) to drag the tip along with the rest of the blade. As the pitch angle is decreased from 25° to 10°, the increased flow separation around the blade tip increases the fraction of the span operating at positive power. The negative power magnitude increases along the whole span from 25° to 20° pitch. The further decrease in pitch from 20° to 15° only redistributes the power along the blade span. The power contribution from the inboard part of the blade increases and from the outboard part decreases with the decrease of the pitch angle, resulting in almost similar power levels at 15° and 20° pitch settings as already seen in figure 14a. A further decrease from 15° to 10° results in a decrease in negative power magnitude from the outboard sections; however, there is a negligible increase in power from the inboard sections, resulting in a lower negative power magnitude overall. The local maxima around $0.45R$ can also be seen in the power distribution of the 10° pitch setting, which results from a decrease in local lift magnitude, as explained before.

2. Unsteady Aerodynamic Performance Analysis

As the propeller is operating at 0° inflow angle, the blade loading is expected to be axisymmetric. That is indeed the case for the positive thrust regime as shown in figure 16a, in which the radial distribution of instantaneous thrust coefficient (T_c') along the blade span is shown as a function of circumferential position. However, the same is not true for the negative thrust regime, as shown in figure 16b. It should be noted that the sign of the instantaneous thrust coefficient (T_c') has been reversed in figure 16b to make the comparison easier with figure 16a. The thrust distribution for the 20° pitch angle shows significant fluctuations over the rotation (amplitude of up to 18% for inboard sections and up to 30% for the blade tip compared to the time-averaged loads). These fluctuations are the result of the flow separation on the back side (suction) of the propeller (figure 13b). The high amplitude and frequency of these fluctuations in the negative thrust regime make the blade loads dynamic rather than static. These changes in the loading may have an impact on the structural integrity of the propeller blades in the negative thrust regime.

The effect of the load fluctuations on the integrated thrust performance (from all blades together) is shown in figure 17a for a total of six rotations. In the positive thrust regime, the fluctuations in the integrated thrust coefficient are below ±1% of time-averaged thrust coefficient, in contrast to the negative thrust regime fluctuations, which are up to ±3%. The fluctuation in the integrated thrust might lead to additional requirements in the power train due to the excitation of the shaft. The amplitude of these fluctuations depends upon the negative thrust level (or the pitch setting in this case). As the negative thrust level increases (i.e., a decrease in pitch angle in this case), the flow separation around the blades increases, leading to an increase in load fluctuations. Figure 17b shows the standard deviation of the integrated thrust normalized with the time-averaged thrust value. The average fluctuation amplitude increases from 0.7% to 1.5% as the negative T_C increases from -0.04 to -0.14. In the positive thrust regime, the sudden increase of the average fluctuation amplitude to 1.2% for $T_C = 0.01$ results from the low normalizing value (T_C). In contrast to the

negative thrust regime, the amplitude of fluctuation is below 0.5% for all the positive thrust conditions. Eventually, the fluctuations in the positive thrust regime would increase once significant flow separation is encountered (at higher pitch settings); however, those settings are considered irrelevant in the current study.

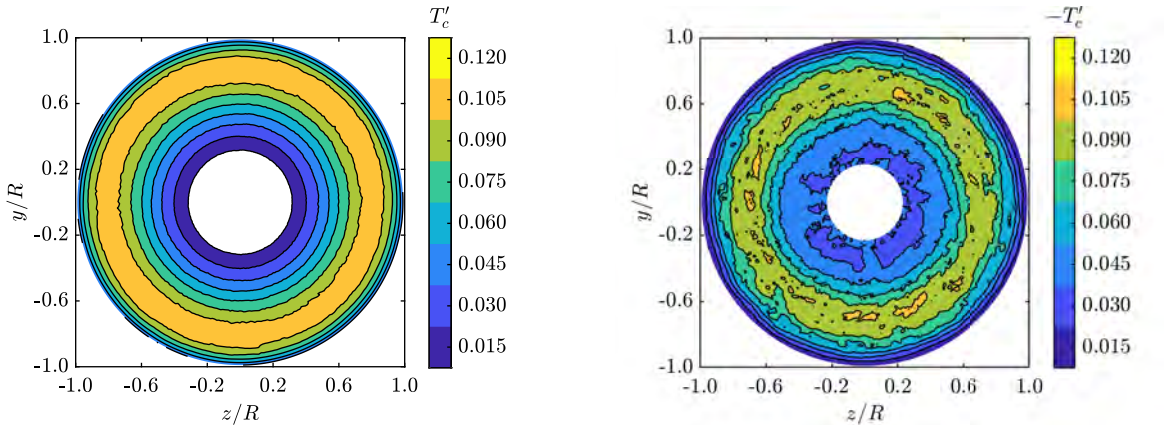

(a) T_C = +0.08, $\beta_{0.7R}$ = 37.57° **(b) T_C = −0.08, $\beta_{0.7R}$ = 20°**

Fig. 16 Radial distribution of instantaneous thrust coefficient (T_c')along the propeller blade span over a rotation as a function of circumferential position for T_C = ±0.08 at J = 1.34, M_∞ = 0.29

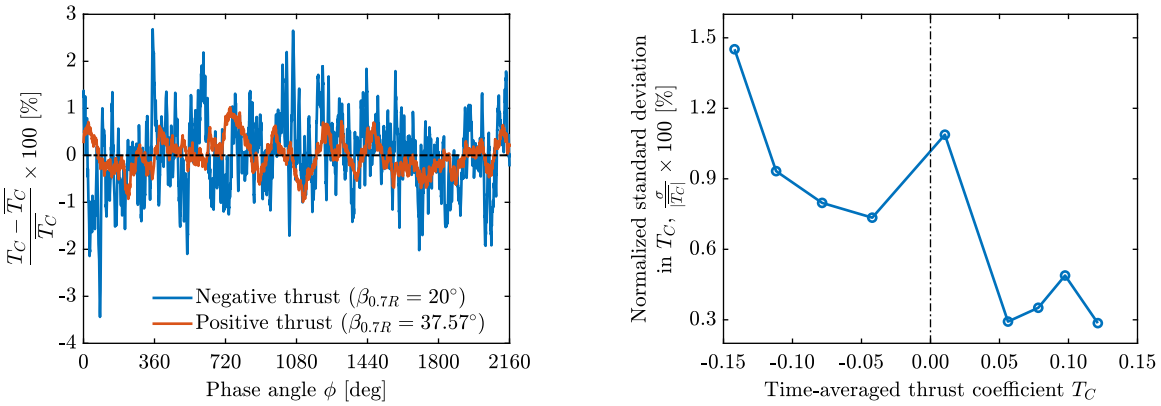

(a) Variation in integrated thrust over multiple rotations for $|T_C|$ = 0.08 **(b) Normalized standard deviation in thrust over six rotations for different pitch settings**

Fig. 17 Time-accurate integrated thrust performance at J = 1.34, M_∞ = 0.29

3. Slipstream

The slipstream in a negative thrust condition is expected to have significantly different characteristics than in a conventional positive thrust condition. The time-accurate data in the slipstream was available from simulations with a 5° resolution for one propeller rotation leading to 72 time instances. From each time instance, three slices aligned with the three propeller blades were extracted. The resulting 216 slices were averaged (given their expected symmetry for uniform inflow) to obtain the final phase-locked results. The phase-locked axial and tangential velocity contours in the

propeller slipstream have been compared in figures 18 and 19 at an absolute thrust level of $|T_C| = 0.08$, corresponding to pitch angles of 20° and 38.93° for negative and positive thrust respectively. Figure 18a and 19a show the contours of the mean of the phase-locked velocities and figures 18b and 19b show contours of the standard deviation of the phase-locked velocities. In these figures, the slipstream contours on the top side of the nacelle show the negative thrust condition, and the slipstream in the positive thrust condition is shown on the bottom side.

As expected, the operation at negative thrust results in decreased axial velocity in the slipstream compared to the freestream condition, whereas the positive thrust results in increased axial velocity. This difference in the axial velocity causes an axial shift of the tip vortex between the two conditions; see figure 18a. Also, the radial gradients where the tip vortex cuts the measurement plane are much higher in the positive thrust case than in the negative thrust condition. As the radial gradients due to the tip vortex at $x/R \approx 1.0$ are diffused over a larger region in the negative thrust case, the region with a higher standard deviation is also spread over a larger region compared to the positive thrust case, as can be seen in figure 18b. These plots also highlight the difference in the shape of the blade wake and tip vortex between the two thrust conditions. In the positive thrust condition, the blade wake is downstream of the tip vortex due to the increased axial velocity. However, the axial velocity is reduced in the negative thrust condition, leading to the tip vortex being downstream of the blade wake.

From the results shown in figure 18, three main inferences can be drawn regarding the nature of fluctuations experienced by a wing surface immersed in such a slipstream. Firstly, an aerodynamic surface immersed in a slipstream at a negative thrust setting would experience reduced dynamic pressure resulting in a reduction in local lift. In contrast, an aerodynamic surface immersed in a slipstream at a positive thrust would experience an increase in local lift. Secondly, as the vortices in the negative thrust regime are expected to be closer to each other due to reduced pitch between the tip vortices (figure 18a), this results in more pressure fluctuations over a wing immersed in a slipstream with negative thrust condition than the positive thrust condition over a given axial distance. Lastly, as can be noticed in figure 18b, the fluctuations due to the tip vortex are concentrated over a small region compared to the negative thrust condition. Therefore, a wing immersed in a slipstream at a positive thrust condition would experience high-amplitude periodic impingement of the tip vortex. On the other hand, a wing immersed in a slipstream at a negative thrust condition would experience comparatively low-amplitude periodic impingement scattered over a comparatively larger area. These inferences will be tested in the follow-up work with the installed configuration.

Figure 19 shows the tangential velocity in the slipstream. This study defines the tangential velocity as positive in the clockwise direction. As expected, the direction of the propeller-induced swirl is in the direction of the rotation of the propeller (anti-clockwise) in the conventional positive thrust regime, see figure 19a. In contrast, as the direction of the torque is reversed in the negative thrust condition, the direction of the propeller-induced swirl is also reversed, i.e., opposite to the propeller rotation. Therefore, the interaction effects with a body immersed in the propeller slipstream operating at negative thrust would be reversed compared to the effects in the positive thrust condition. Moreover, the

gradients in the axial direction near the propeller plane are stronger in the negative thrust condition compared to the positive thrust condition. These differences between the two regimes originate from the differences in blade loading distribution resulting in a different vortex system leading to different inductions in the slipstream. Figure 19b shows the contours of the standard deviation of the phase-locked tangential velocity in the propeller slipstream. The trends are similar to those shown in figure 18b, i.e., the strong fluctuations in the tangential velocity are concentrated in the region where the tip vortex cuts the measurement plane. Similar to figure 18b, figure 19b also shows that the high fluctuation region (around $x/R = 1.0$) is spread over a larger region in the negative thrust condition compared to the positive thrust condition.

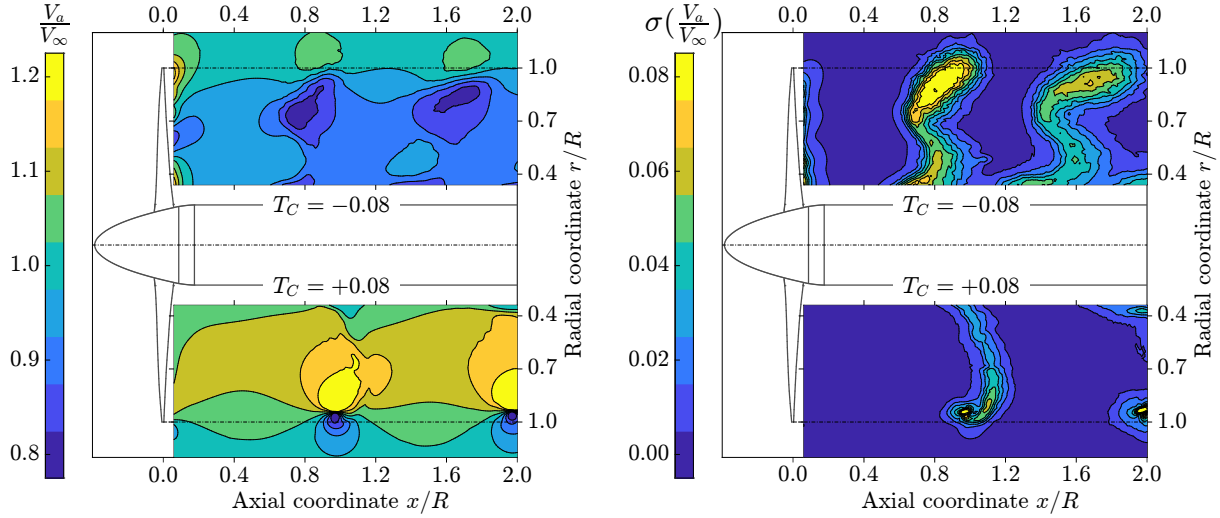

(a) Averaged phase-locked axial velocity

(b) Standard deviation of phase-locked axial velocity

Fig. 18 Comparison of axial velocity contours in negative ($\beta_{0.7R} = 20°$) and positive ($\beta_{0.7R} = 38.93°$) thrust condition at absolute thrust level of $|T_C| = 0.08$ (Phase-locked)

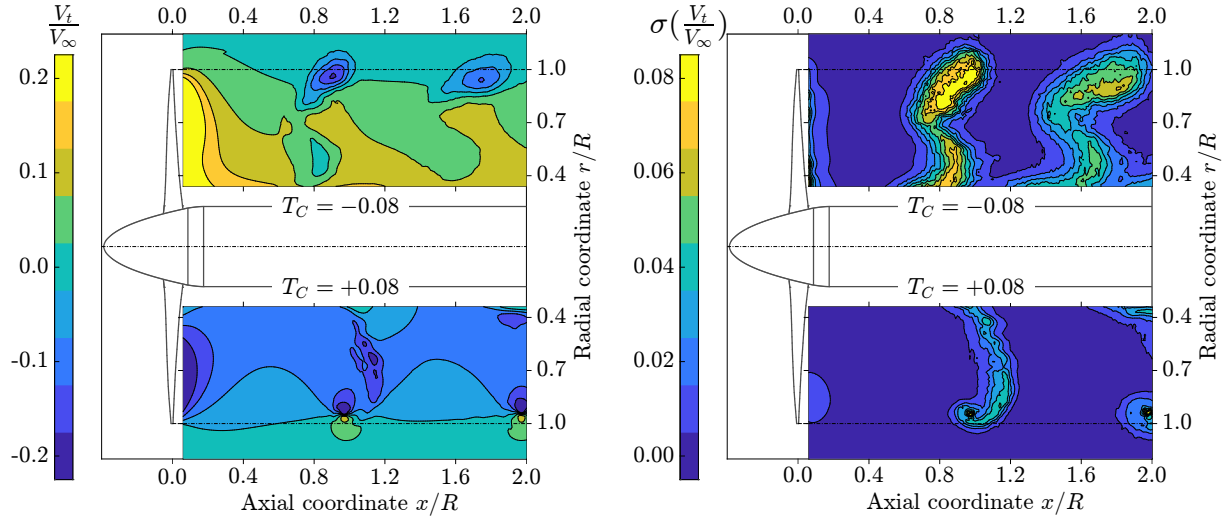

(a) Averaged phase-locked tangential velocity **(b) Standard deviation of phase-locked tangential velocity**

Fig. 19 Comparison of tangential velocity contours in negative ($\beta_{0.7R}$ = 20°) and positive ($\beta_{0.7R}$ = 38.93°) thrust condition at absolute thrust level of $|T_C|$ = 0.08 (Phase-locked)

Figure 20 shows the radial distributions of time-averaged axial and tangential velocity in the slipstream at $1R$ downstream of the propeller center. The axial location for the comparison was based on its relevance for an installed case. The radial distributions of axial velocity in figure 20a display the expected increase in velocity with the increase in thrust for the positive thrust conditions with pitch settings between 30° and 45°. Similarly, the negative thrust conditions show an expected decrease in axial velocity with the increasingly negative thrust value. The radial distributions of axial velocity for 10° and 15° show a local maximum similar to the one seen in the blade loading distributions in figure 14c. In the positive thrust regime, the strong radial gradients of the axial velocity near $r/R = 1$ result from the high spanwise gradients of the loading distribution seen in figure 14c. In contrast, as the spanwise loading gradients are comparatively lower in the negative thrust regime near $r/R = 1$, the corresponding radial gradients of the axial velocity are also lower. The slope steepens with an increase in the magnitude of the negative thrust due to the increase in the corresponding spanwise loading gradients. The increasing blade loading at the inboard sections with the decreasing pitch settings results in decreasing axial velocities in the wake at the corresponding radial coordinates in figure 20a.

As expected, the tangential velocities are opposite in negative thrust conditions compared to the positive thrust condition due to the opposite direction of torque, see figure 20b. High loading at the inboard blade sections in the negative thrust regime results in high tangential velocities at the corresponding radial coordinates in the wake. With the increasing radial coordinate, though the dynamic pressure increases, the power coefficient stays almost constant (figure 14d), resulting in decreasing tangential velocities in the wake. Hence explaining the large radial gradients observed in the negative thrust conditions in figure 20b. In contrast, in positive thrust conditions, the power coefficient increases with the increasing radial coordinate resulting in almost constant tangential velocities in the wake at a given

axial location, as can be seen in figure 20b. At the radial coordinate of 0.9, the power coefficient becomes positive in the negative thrust conditions resulting in negative tangential velocities. From these trends, it becomes clear that a wing immersed in the slipstream of a negative thrust condition will perceive a changed effective angle of attack compared to a positive thrust condition.

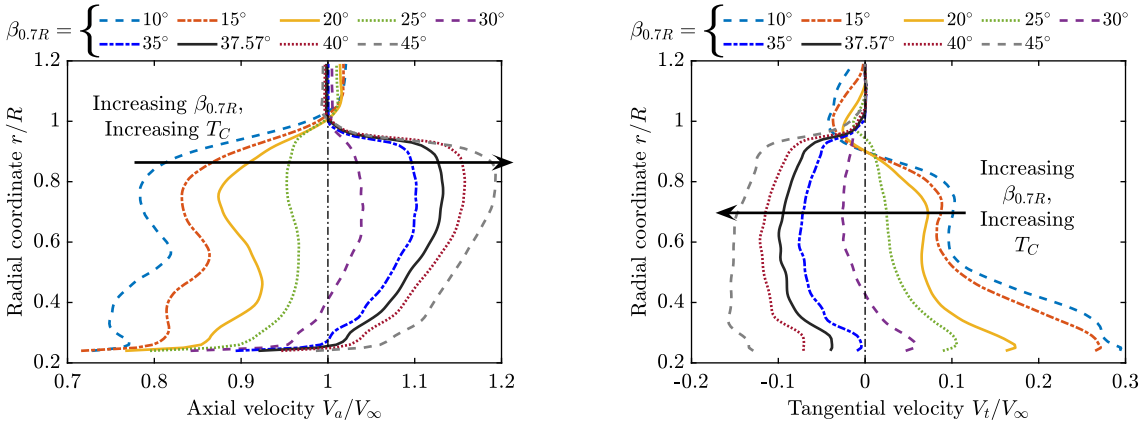

(a) Axial velocity **(b) Tangential velocity**

Fig. 20 Radial distributions of time-averaged axial and tangential velocity in the propeller slipstream at 1*R* downstream of the propeller center

B. Far-field Acoustic Characteristics

The changes in the aerodynamics of the negative thrust regime compared to the conventional positive thrust regime are expected to modify the resulting acoustic emissions. The tonal noise is sensitive to both blade loading and thickness, making it difficult to isolate the changes in the noise sources between the two regimes (positive and negative thrust). Building upon the previous section's discussion, the current section also analyzes the cases with the fixed tip Mach number (different thrust settings achieved through variation in blade pitch setting). This strategy allows studying the changes in the noise characteristics solely due to the change in the blade loading characteristics and not due to a change in thickness noise. The convection effects have been neglected in this analysis as the main interest is in the change of noise mechanism.

1. Far-field Noise Directivity and Power Spectrum Density (PSD)

Figure 21a shows the resulting far-field noise directivity at a distance of 20*R*. The noise directivity has been calculated in two ways. The dash lines with markers are obtained by propagating the pressure signal captured at the blade surface to the far field using the FWH analogy. Therefore, these lines represent the total noise generated by the propeller blades, i.e., the sum of tonal and broadband noise. The solid lines (without markers) are obtained by feeding the time-averaged blade loading shown in figures 14c and 14d to Hanson's model [11] to calculate the tonal noise due to the time-averaged blade loading. The noise can be decomposed into two components using the FWH analogy: loading

noise and thickness noise, based on their respective integral terms [36]. The advantage of using Hanson's model is that it further decomposes the loading noise into the noise due to the thrust and torque.

The dashed black line shows the thickness noise obtained from the FWH analogy, whereas the dotted black line shows the thickness noise obtained using Hanson's model. The FWH analogy gives the total noise obtained from the high-fidelity simulations, whereas Hanson's model gives further insight into the loading noise sources. Comparing the noise levels obtained from the two approaches shows that Hanson's model overpredicts the tonal noise by 2-3 dB for both positive and negative thrust conditions, which originates from the simplifications inherent in Hanson's model [11]. The thickness noise is also overpredicted by 3 dB in the propeller plane. As broadband noise is the primary source of the noise near the propeller axis, the total noise level (predicted by FWH analogy) is higher than the tonal noise levels (predicted by Hanson's model) for $0^\circ \leq \theta < 30^\circ$ and $150^\circ < \theta \leq 180^\circ$. For approximately $30^\circ \leq \theta \leq 150^\circ$, Hansons's model agrees qualitatively with the FWH analogy and can be used to understand the relative importance of different tonal noise sources. Therefore, this analysis with the Hanson model has been used to gain more insight into these noise sources.

The positive thrust condition has 10 dB higher noise in the propeller plane than the negative thrust condition, which is also reflected in the power spectrum density plot shown in figure 22b. This difference in the tonal noise is expected to originate from two sources: a) higher noise due to torque in the positive thrust condition (due to higher torque, see figure 14d); b) differences in blade loading distribution between the two conditions as seen in figure 14c. These sources of difference between the loading noise at positive and negative thrust have been analyzed further by decomposing the loading noise into noise produced by thrust and torque using Hanson's model, see figure 21b. Though the absolute thrust level is the same for both conditions, the more outboard loading in the positive thrust condition leads to a 4 dB higher noise due to thrust. Despite the constant absolute thrust level, the magnitude of the torque is approximately three times higher in the positive thrust condition than in the negative thrust condition. The higher torque amplitude results in up to 12 dB higher noise in the positive thrust condition than in the negative thrust condition. As evident from figure 21b, noise due to torque is the dominant noise for the positive thrust condition for the given operating condition. In contrast, the noise produced by thrust and torque is comparable in the negative thrust condition. For both regimes, the noise due to thrust has two lobes, with the front lobe interfering destructively with the noise due to torque and the back lobe interfering constructively with the noise due to torque, irrespective of thrust direction. This interference trend between noise produced by thrust and torque agrees with the previous studies [7, 35]. As noise levels produced by thrust and torque are comparable in the negative thrust condition, the destructive interference results in a decreased loading noise in front of the propeller plane, as can also be seen in the FWH analogy results in figure 21a. In the positive thrust condition, the noise due to thrust has a small effect on the overall loading noise.

Along the propeller axis ($0^\circ \leq \theta \leq 30^\circ$ and $150^\circ \leq \theta \leq 180^\circ$), the negative thrust condition results in 13-15 dB higher noise than the positive thrust condition along the propeller axis; see the FWH analogy results in figure 21a. This

is an expected result of the increased flow separation in the negative thrust condition compared to the positive thrust condition, as seen in figure 13. The increased broadband noise can also be seen in the power spectrum density plot shown in figure 22a.

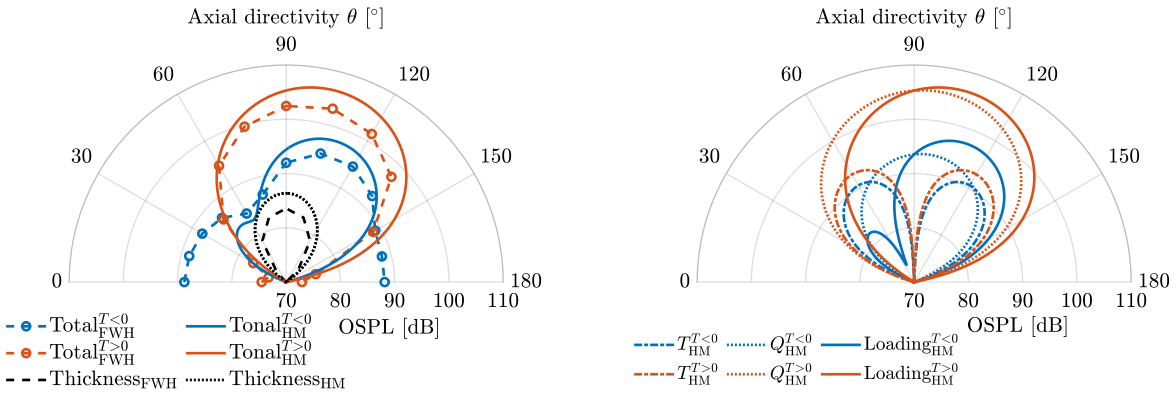

(a) Noise directivity at positive and negative thrust based on FWH analogy and Hanson's model

(b) Contribution of noise produced by thrust and torque to the loading noise based on Hanson's model

Fig. 21 Far-field noise directivity of the propeller in positive and negative thrust regimes at absolute thrust level of $|T_C| = 0.08$

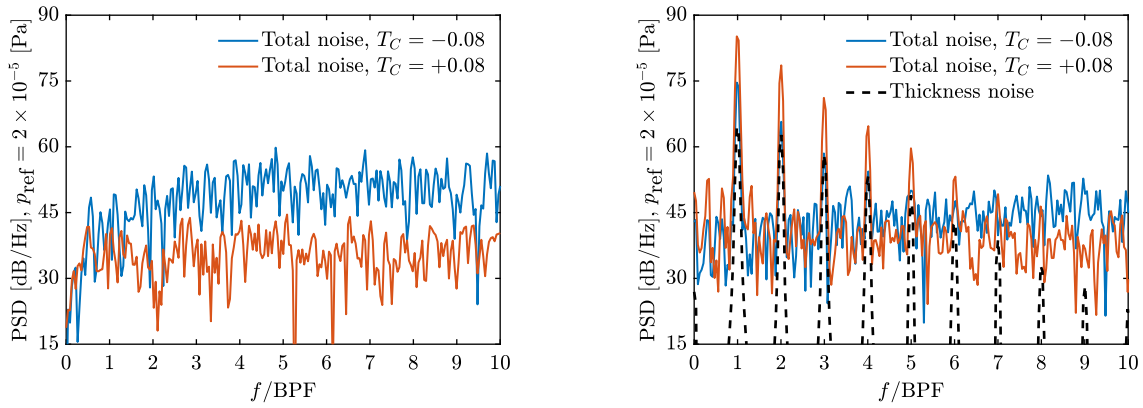

(a) Upstream along propeller axis ($\theta = 0°$)

(b) Propeller plane ($\theta = 90°$)

Fig. 22 Power spectrum density at $\theta = 0$ and 90° for absolute thrust level of $|T_C| = 0.08$

2. Noise Source Map

To further understand the difference between the noise sources in positive and negative thrust conditions, a post-processing tool from 3DS named OptydB-PFNOISESCAN was used. This tool calculates the noise contribution per unit surface area emitted towards a given microphone at every time step, and then Fourier transforms the unsteady surface field to provide output for a given frequency range. The noise contribution of the surfels is calculated in terms of power density, i.e., Pa^2/m^2 and then the resulting value is converted into dB by taking the log, resulting in the units of

dB/m^2. It should be noted that this tool uses the assumption of a compact source, which is a reasonable assumption for the first two BPFs ($M_o c/\lambda < 0.1$) for the given operating conditions ($M_\infty = 0.29, M_{ht} = 0.74$). Nine time instances of the obtained results are shown for one of the blades in figure 23 and figure 24 for $\theta = 0°$ and $90°$ respectively. For $\theta = 0°$, the frequency range was chosen to be 1 - 2 BPF, given the considerable difference in PSD between the two operating conditions seen in figure 22a and constraints imposed by the assumption of a compact source. Similarly, for $\theta = 90°$, the first BPF was chosen to compare the location of tonal noise sources at the given operating conditions based on figure 22b.

Figure 23a and 23c show the noise source maps of the front and back sides of the propeller respectively for a microphone located along the propeller axis ($\theta = 0°$) for $T_C = +0.08$ ($\beta_{0.7R} = 37.57°$). Similarly, figures 23b and 23d show the noise source maps of the front and back sides of the propeller respectively for the same microphone location for $T_C = -0.08$ ($\beta_{0.7R} = 20°$). As the microphone is located along the propeller axis, the noise source contribution is independent of the circumferential position in figure 23. As can be noticed from the figure, broadband noise is dominant for this observer location (figure 22a). Since the inflow turbulence is negligible, the two main sources of broadband noise are trailing-edge noise and flow separation. For the front side of the propeller (figure 23a), the noise mainly comes from the trailing edge. The strong noise sources near the trailing edge can be related to the trailing-edge separation seen in figure 13a. Similarly, on the back side of the propeller, the noise sources are observed at the inboard sections corresponding to the separation bubble seen in figure 13a along with trailing-edge noise sources located relatively outboard.

In contrast, the extensive flow separation on the back side of the propeller in the negative thrust condition (as shown in figure 13b) leads to a dominant broadband noise contribution from the whole back surface of the blade, see figure 23d. Again the inboard region with the attached flow in figure 13b features negligible noise generation radiated to the given microphone. With the increase in local Mach number and pressure amplitude (due to the increased dynamic pressure) in the radial direction, the extent of flow separation also increases from the root to the tip, enhancing the strength of the broadband noise source. For the conventional regime, i.e., positive thrust condition, the front side is the dominant source of broadband noise. In contrast, the back side is the dominant broadband noise source in the negative thrust condition.

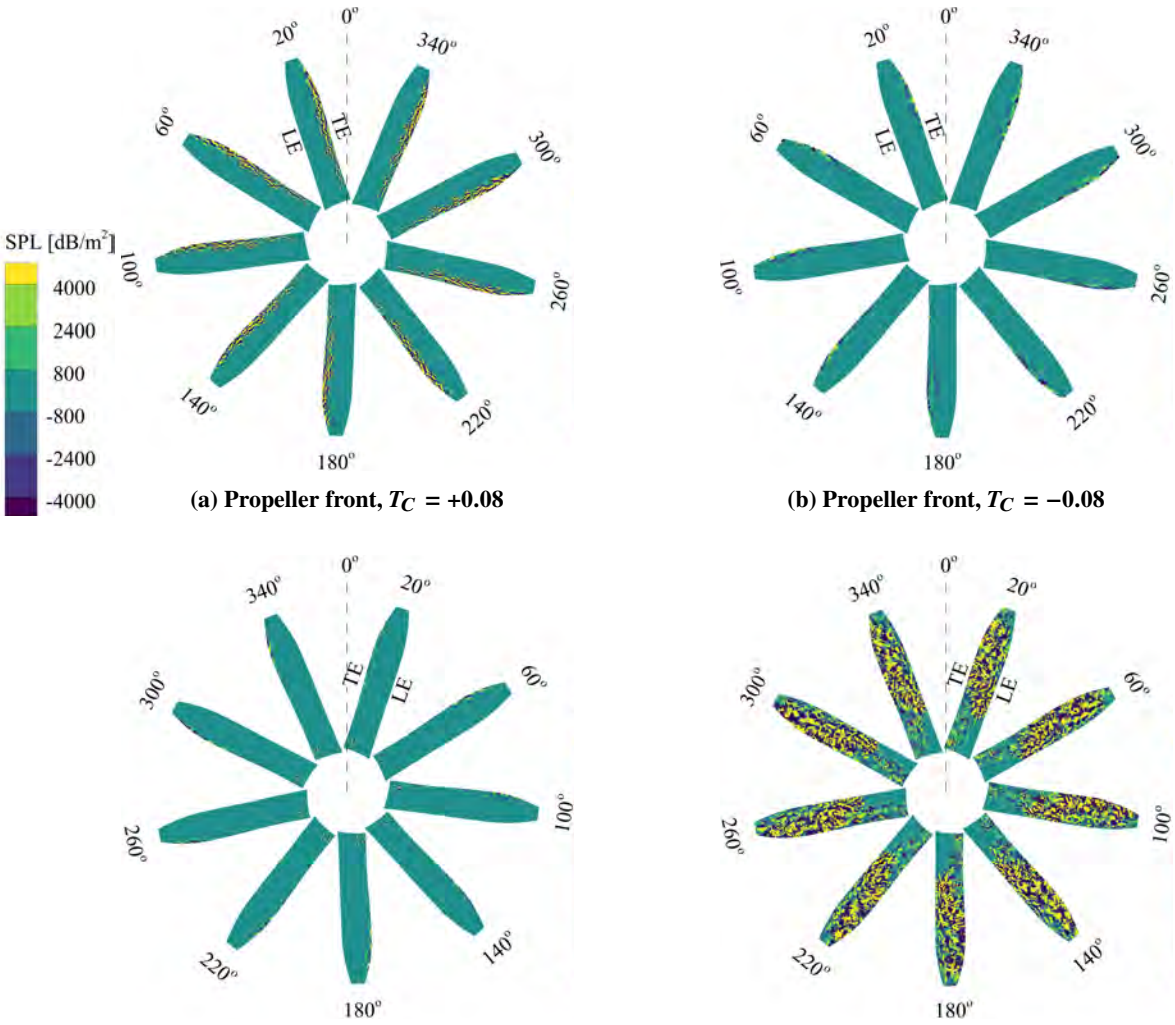

(a) Propeller front, $T_C = +0.08$ **(b) Propeller front, $T_C = -0.08$**

(c) Propeller back, $T_C = +0.08$ **(d) Propeller back, $T_C = -0.08$**

Fig. 23 Noise source map (1 - 2 BPF) on a single propeller blade for an observer located along the propeller axis ($\theta = 0°$) at positive and negative thrust conditions

To compare the distribution of tonal noise source for the two operating conditions, the noise source map for $\theta = 90°$ at the first BPF is shown in figure 24. Because the microphone is located in the propeller plane along the 0° line depicted in the figure, the source contribution varies with the circumferential position. This is a consequence of the varying distance between the blade surface and the microphone due to the rotation of the blade surface. Due to the increase in local Mach number and pressure amplitude (due to the increased dynamic pressure) in the radial direction, the outboard part of the blade has the most dominant contribution to the noise in the propeller plane in the conventional positive thrust regime on both the front and the back side of the propeller (figures 24a and 24c). In the negative thrust case as well, a clear dominant noise source can be seen on the outboard part of the blade on the front side of the propeller (figure 24b) contributing to the tonal noise. However, on the back side of the propeller, random fluctuations are superimposed on a circumferential variation of the source amplitude (figure 24d). This indicates the presence of a combination of tonal and

broadband noise. The tonal noise in the positive thrust condition is higher than in the negative thrust case in figure 24 because of higher torque in the positive thrust case, as explained previously.

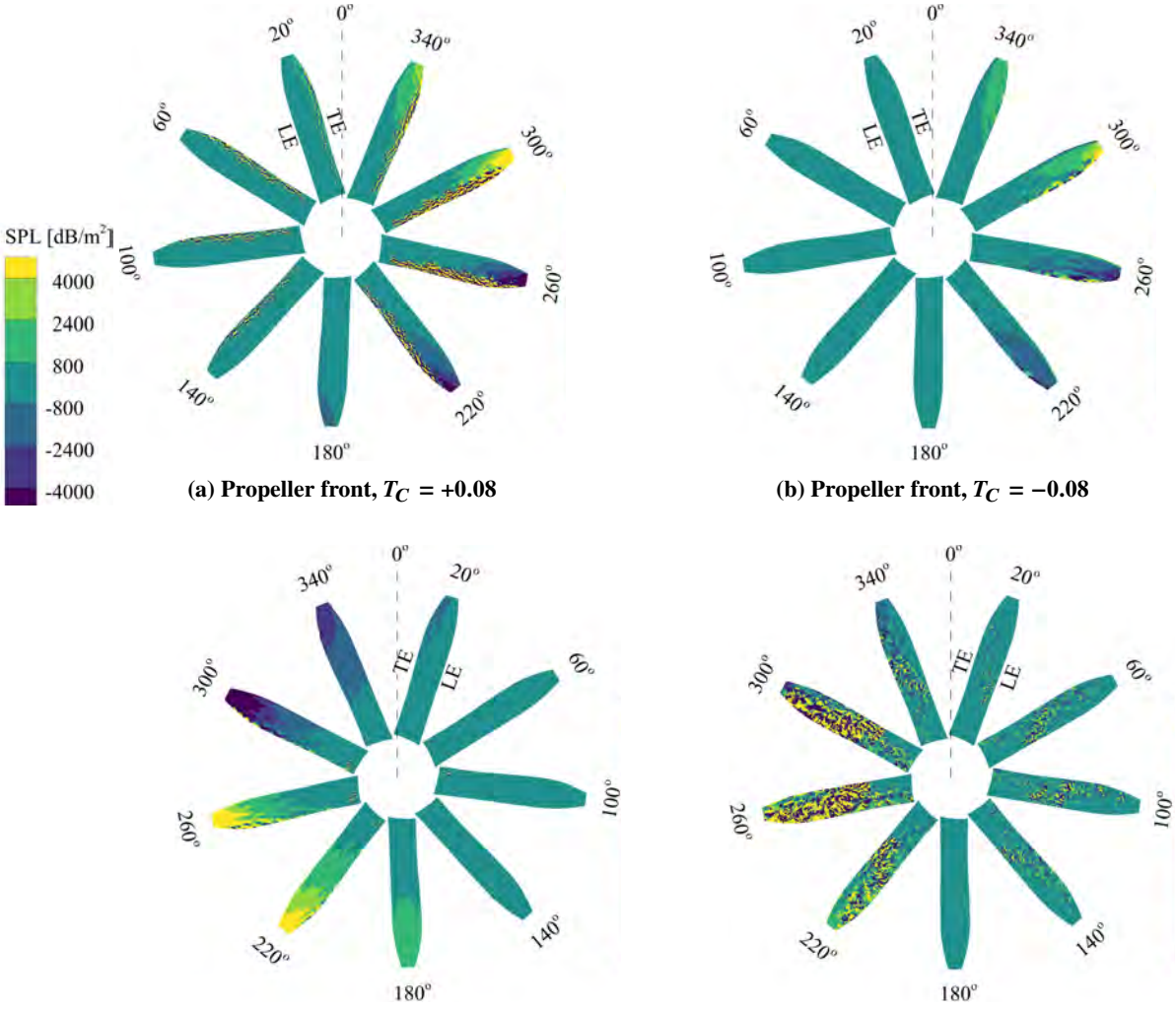

(a) Propeller front, T_C = +0.08 **(b) Propeller front, T_C = −0.08**

(c) Propeller back, T_C = +0.08 **(d) Propeller back, T_C = −0.08**

Fig. 24 Noise source map (1st BPF) on a single propeller blade for an observer located in the propeller plane (θ = 90°) at positive and negative thrust conditions

3. Effect of Thrust Coefficient on OSPL

This section evaluates the effect of the thrust setting on the OSPL. Figure 25a shows the variation of OSPL with the absolute thrust coefficient for both positive and negative thrust regimes using the FWH analogy along the propeller axis (θ = 0°) and in the vicinity of the propeller plane (75° ≤ θ ≤ 105°). The tonal noise in the vicinity of the propeller plane has been decomposed further by using Hanson's model into thrust, torque, and thickness noise, see figure 25b. In figure 25a, the dash-dotted lines show the noise levels along the propeller axis (θ = 0°), where the main contribution comes from the broadband noise sources. The solid lines show the maximum OSPL level between 75° - 105°, where the OSPL is expected to be dominated by tonal noise (see figure 22b). The dashed-black line shows the level of thickness

noise for the given operating condition. The OSPL for the positive thrust condition increases from 71 dB to 80 dB along the propeller axis (dash-dot orange line) when the thrust coefficient increases from 0.01 to approximately 0.12. This is a result of the increase in the broadband noise caused by an increase in trailing-edge separation (figure 13a) with the increase in T_C. Even with the trailing-edge separation, the broadband-dominated noise of the positive thrust regime is considerably lower than that of the negative thrust regime (dash-dot blue line) at all the thrust levels (as expected). The noise along the propeller axis for the negative thrust conditions has a higher positive slope than the positive thrust regime. After a certain thrust level, the broadband-dominated noise level exceeds the tonal-dominated noise levels and becomes the dominant source of the noise. This is a consequence of the significant increase in the broadband noise levels caused by the increasing separation as the magnitude of negative thrust increases.

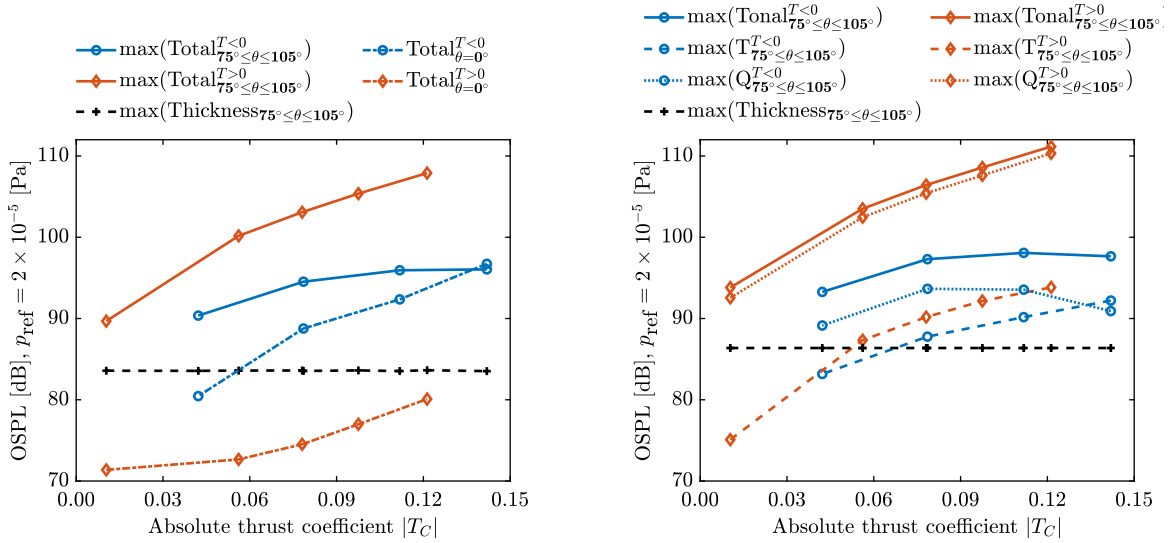

(a) FWH analogy **(b) Hanson's model**

Fig. 25 Effect of thrust coefficient on the noise sources in positive and negative thrust regimes for a propeller operating at a constant rotational speed (M_∞ = 0.29, M_{ht} = 0.74)

On the other hand, the tonal-dominated noise for the positive thrust regime (solid orange line) is considerably higher than the tonal-dominated noise for the negative thrust regime (solid blue line). In the vicinity of the propeller plane, the negative thrust condition with a thrust coefficient of $T_C = -0.04$ produces approximately similar noise as produced in the positive thrust regime at $T_C = +0.01$. The positive thrust regime has a much steeper slope along the whole range of thrust levels than the negative thrust regime (figure 25). In contrast, there is a little increase in the noise near the propeller plane for $|T_C| \geq 0.08$ in the negative thrust regime. These trends can be explained by decomposing the tonal noise into thrust, torque, and thickness noise using Hanson's model is shown in figure 25b. Hanson's model predicts similar trends as the FWH analogy for the noise in the given directivity range. In the vicinity of the propeller plane, the noise due to torque (dotted orange line) is the dominant noise source for the whole thrust range in the positive thrust regime. The same is true for the negative thrust regime up to the maximum regeneration point. As a result,

even though the absolute thrust magnitude in the negative thrust condition ($T_C = -0.04$) is approximately four times higher than the positive thrust condition ($T_C = +0.01$), the tonal noise levels are similar due to the similar magnitude of P_C ($|P_C| = 0.02$), see figure 14a. As in the positive thrust regime, the torque increases with the increasing thrust magnitude, and the tonal noise levels also increase. However, in the negative thrust regime, the operating conditions with $T_C = -0.08$ and -0.11 have similar values of P_C (figure 14a), resulting in similar tonal noise levels. After the maximum regeneration point, the magnitude of the negative torque starts to decrease, whereas the magnitude of the negative thrust continues to increase. As a result, noise due to thrust becomes the dominant noise source after a certain point; see figure 25b. However, such an operating condition probably would not be relevant for an aircraft due to the high magnitude of the negative thrust coefficient.

4. Main Inferences for Landing Using Negative Thrust Settings

Three main inferences can be drawn from the trends observed in figure 25. Firstly, it can be concluded that for a given absolute thrust level, the negative thrust regime can be expected to have lower noise in the propeller plane than the positive thrust regime based on two facts: a) For a given thrust level, the noise due to thrust in positive thrust condition can be expected to be always higher than the noise due to negative thrust due to more outboard loading; b) As concluded in the earlier work [7] as well, the torque required to generate a given thrust level can be expected to be always higher than the torque regenerated at the same absolute thrust level in the negative thrust regime (for a conventional propeller design). As a result, the sum of the noise due to both thrust and torque is expected to be lower in the negative thrust regime compared to the positive thrust regime for a given absolute thrust; therefore, the resulting tonal noise is also expected to be lower. Secondly, it can be concluded that for a conventional propeller, the negative thrust regime is expected to be noisier along the propeller axis than the positive thrust regime, irrespective of the thrust or torque level. Lastly, the noise due to torque is expected to be the dominant noise source in the operating conditions (moderate thrust levels) relevant for a landing using negative thrust. When the negative torque is below the torque required to operate the propeller in a conventional landing, the noise near the propeller plane can be expected to be either lower or similar to the noise generated by the propeller in a conventional landing. A similar torque level in the two regimes is achieved at a higher absolute thrust in the negative thrust regime compared to the conventional positive thrust regime. It essentially means that a steeper descent is possible without increasing the tonal noise (without considering the effects of inflow angle on the tonal noise). Moreover, the steeper descent means that the vicinity of the airport is exposed to the noise for a shorter time and generally at larger distances. This would lead to reduced noise hindrance even at a constant source noise level.

V. Conclusions

A numerical investigation has been carried out using the Lattice-Boltzmann method coupled with a very large-eddy model to understand the aerodynamics and far-field noise characteristics of an isolated propeller operating in positive and negative thrust regimes. The setup has been validated by comparison against experimental data for two operating conditions (J = 0.60, and 1.10). In the case of the positive thrust condition (J = 0.60), the LBM simulations are able to predict the thrust accurately (within 1%). However, the power prediction is off by about 10% due to the underprediction of the drag. The underprediction of drag is expected to occur because of a separation bubble on the blade surface, which makes the prediction of the reattachment location difficult and thus leads to higher uncertainty on the drag. Due to the limitations in simulating separated flow, the negative thrust regime (J = 1.10) simulations underpredict the power and overpredict the thrust by 10%. The comparison of the radial distribution of total pressure, and axial and tangential velocity distributions in the slipstream showed that LBM-VLES simulations are able to capture the gradients in the radial and axial directions despite the differences in the predicted integrated performance. As the LBM-VLES simulations performed in this paper tend to underpredict and overpredict the power for positive and negative thrust regimes, respectively, it can be concluded that the simulations tend to be conservative in the prediction of tonal noise for the positive thrust conditions and overpredict the tonal noise for the negative thrust regime given that the noise due to the torque is dominant at low to moderate thrust settings.

A propeller operating at a constant rotational speed but varying pitch angle was used to investigate the far-field noise characteristics with a freestream Mach number of 0.29 and helicoidal tip rotational Mach number of 0.74. Such a configuration ensures that the thickness noise stays constant as the loading is changed with the variation of pitch setting. The resulting absolute thrust coefficient lies in the range of 0.01 - 0.12 for the positive thrust regime and between 0.04 - 0.14 for the negative thrust regime. As expected, thrust shows a monotonic decreasing trend with the increase in pitch angle in the negative thrust regime. Power reaches a maximum at a unique pitch setting (for the studied propeller at 15°). The blade loading distributions show that the peak in the radial distribution of thrust is located inboard (0.7R) compared to the spanwise location of maximum loading (0.85R) for the positive thrust regime. Moreover, most of the negative power comes from the inboard part of the blade (up to 0.6R) compared to the positive thrust regime, where the maximum power loading is around 0.85R. The flow separation around the blades in the negative thrust regime increases average fluctuations from 0.7% at $T_C \approx -0.04$ to 1.5% at $T_C \approx -0.14$ in the integrated thrust. In comparison, the fluctuations are below 0.5% for all thrust settings in the positive thrust regime. Further, the blade loading in the negative thrust regime shows the amplitude of fluctuations of up to 18% for inboard sections and up to 30% near the blade tip compared to the time-averaged loads. The analysis of the slipstream flowfields shows that an aerodynamic body immersed in a slipstream at a negative thrust setting will experience reduced dynamic pressure and opposite tangential velocity compared to those experienced at a positive thrust setting.

The analysis of the far-field noise characteristics shows that a conventional propeller operating in the negative thrust

regime can be expected to produce more broadband noise than in positive thrust conditions at all practical thrust settings. The tonal noise in the positive thrust regime is higher than in the negative thrust regime for a given absolute thrust. This difference arises from two sources. Firstly, the higher torque leads to higher noise due to torque in the positive thrust regime. Secondly, the higher absolute loading on the inboard blade segments results in a lower noise due to thrust in the negative thrust regime, even though the absolute thrust level is the same. As the noise due to torque is the dominant noise source for low to moderate thrust settings, a steeper and quieter descent compared to a conventional descent is possible using negative thrust as long as the negative torque produced is equal to or lower than the torque required to operate the propeller in a conventional landing (without considering the effect of inflow angle on propeller noise). Additional reduction in noise hindrance is expected due to the steeper descent leading to shorter exposure time to the community noise.

Acknowledgments

The research leading to these results is part of the FUTPRINT50 project. This project has received funding from the European Union's Horizon 2020 Research and Innovation programme under Grant Agreement No 875551. This work made use of the Dutch national e-infrastructure with the support of the SURF Cooperative using grant no. EINF-2733. The authors would like to thank Robert Nederlof for providing the experimental data for the validation of the simulations.

References

[1] Veldhuis, L. L. M., *Propeller wing aerodynamic interference*, Ph.D. Dissertation, Delft University of Technology, Netherlands, 2005. URL http://resolver.tudelft.nl/uuid:8ffbde9c-b483-40de-90e0-97095202fbe3.

[2] Hartman, E. P., "Negative Thrust and Torque Characteristics of an Adjustable-pitch Metal Propeller," *Annual Report-National Advisory Committee for Aeronautics*, Vol. 19, 1933, p. 421. URL http://hdl.handle.net/2060/19930091538.

[3] Hedrick, W. S., and Douglass, W. M., "An Experimental Investigation of the Thrust and Torque Produced by Propellers Used as Aerodynamic Brakes," Tech. Rep. NACA-WR-A-27, National Advisory Committee for Aeronautics, 1944. URL http://hdl.handle.net/2060/19930093338.

[4] Thomas, J. L., and Hansman, R. J., "Community Noise Reduction Assessment of Using Windmilling Drag on Approach by Hybrid Electric Aircraft," *AIAA Aviation 2020 Forum*, AIAA Paper 2020-2877, June 2020. https://doi.org/10.2514/6.2020-2877.

[5] Eržen, D., Andrejašič, M., Lapuh, R., Tomažič, J., Gorup, Č., and Kosel, T., "An Optimal Propeller Design for In-Flight Power Recuperation on an Electric Aircraft," *2018 Aviation Technology, Integration, and Operations Conference*, AIAA Paper 2018-3206, June 2018. https://doi.org/10.2514/6.2018-3206.

[6] Sinnige, T., Stokkermans, T. C. A., van Arnhem, N., and Veldhuis, L. L. M., "Aerodynamic Performance of a Wingtip-Mounted

Tractor Propeller Configuration in Windmilling and Energy-Harvesting Conditions," *AIAA Aviation 2019 Forum*, AIAA Paper 2019-3033, June 2019. https://doi.org/10.2514/6.2019-3033.

[7] Goyal, J., Sinnige, T., Avallone, F., and Ferreira, C., "Aerodynamic and Aeroacoustic Characteristics of an Isolated Propeller at Positive and Negative Thrust," *AIAA Aviation 2021 Forum*, AIAA Paper 2021-2187, June 2021. https://doi.org/10.2514/6.2021-2187.

[8] Nederlof, R., Ragni, D., and Sinnige, T., "Experimental Investigation of the Aerodynamic Performance of a Propeller at Positive and Negative Thrust and Power," *AIAA AVIATION 2022 Forum*, AIAA Paper 2022-3893, June 2022. https://doi.org/10.2514/6.2022-3893.

[9] Szydlowski, J., and Costes, M., "Simulation of Flow Around a Static and Oscillating in Pitch NACA 0015 Airfoil Using URANS and DES," *Heat Transfer Summer Conference*, Vol. 2, Parts A and B, July 2004, pp. 891–908. https://doi.org/10.1115/HT-FED2004-56437.

[10] Shelton, A., Abras, J., Jurenko, R., and Smith, M., "Improving the CFD Predictions of Airfoils in Stall," *43rd AIAA Aerospace Sciences Meeting and Exhibit*, AIAA Paper 2005-1227, 2005. https://doi.org/10.2514/6.2005-1227.

[11] Hanson, D. B., "Helicoidal surface theory for harmonic noise of propellers in the far field," *AIAA Journal*, Vol. 18, No. 10, 1980, pp. 1213–1220. https://doi.org/10.2514/3.50873.

[12] Farassat, F., and Succi, G. P., "A review of propeller discrete frequency noise prediction technology with emphasis on two current methods for time domain calculations," *Journal of Sound and Vibration*, Vol. 71, No. 3, 1980, pp. 399–419. https://doi.org/10.1016/0022-460X(80)90422-8.

[13] Casalino, D., Hazir, A., and Mann, A., "Turbofan broadband noise prediction using the Lattice Boltzmann Method," *AIAA Journal*, Vol. 56, No. 2, 2018, pp. 609–628. https://doi.org/10.2514/1.J055674.

[14] Gonzalez-Martino, I., and Casalino, D., "Fan tonal and broadband noise simulations at transonic operating conditions using lattice-Boltzmann methods," *2018 AIAA/CEAS Aeroacoustics Conference*, 2018, p. 3919. https://doi.org/10.2514/6.2018-3919.

[15] Bres, G., Pérot, F., and Freed, D., "Properties of the lattice Boltzmann method for acoustics," *15th AIAA/CEAS Aeroacoustics Conference (30th AIAA Aeroacoustics Conference)*, 2009, p. 3395. https://doi.org/10.2514/6.2009-3395.

[16] Marié, S., Ricot, D., and Sagaut, P., "Comparison between lattice Boltzmann method and Navier–Stokes high order schemes for computational aeroacoustics," *Journal of Computational Physics*, Vol. 228, No. 4, 2009, pp. 1056–1070. https://doi.org/10.1016/j.jcp.2008.10.021.

[17] Succi, S., *The lattice Boltzmann equation: for fluid dynamics and beyond*, Oxford university press, 2001. https://doi.org/10.1063/1.1537916.

[18] Shan, X., Yuan, X.-F., and Chen, H., "Kinetic theory representation of hydrodynamics: a way beyond the Navier–Stokes equation," *Journal of Fluid Mechanics*, Vol. 550, 2006, pp. 413–441. https://doi.org/10.1017/S0022112005008153.

[19] Casalino, D., Romani, G., Zhang, R., and Chen, H., "Lattice-Boltzmann calculations of rotor aeroacoustics in transitional boundary layer regime," *Aerospace Science and Technology*, Vol. 130, 2022, p. 107953. https://doi.org/10.1016/j.ast.2022.107953.

[20] Romani, G., Grande, E., Avallone, F., Ragni, D., and Casalino, D., "Performance and noise prediction of low-Reynolds number propellers using the Lattice-Boltzmann method," *Aerospace Science and Technology*, Vol. 125, 2022, p. 107086. https://doi.org/10.1016/j.ast.2021.107086, sI: DICUAM 2021.

[21] Casalino, D., Grande, E., Romani, G., Ragni, D., and Avallone, F., "Definition of a benchmark for low Reynolds number propeller aeroacoustics," *Aerospace Science and Technology*, Vol. 113, 2021, p. 106707. https://doi.org/10.1016/j.ast.2021.106707.

[22] Chen, H., Zhang, R., and Gopalakrishnan, P., "Lattice Boltzmann collision operators enforcing isotropy and Galilean invariance," , Feb. 21 2017. URL https://patents.google.com/patent/CA2919062A1/en.

[23] Chen, H., Chen, S., and Matthaeus, W. H., "Recovery of the Navier-Stokes equations using a lattice-gas Boltzmann method," *Physical review A*, Vol. 45, No. 8, 1992, p. R5339. https://doi.org/10.1103/PhysRevA.45.R5339.

[24] Yakhot, V., and Orszag, S. A., "Renormalization group analysis of turbulence. I. Basic theory," *Journal of scientific computing*, Vol. 1, No. 1, 1986, pp. 3–51. https://doi.org/10.1007/BF01061452.

[25] Teixeira, C. M., "Incorporating turbulence models into the lattice-Boltzmann method," *International Journal of Modern Physics C*, Vol. 9, No. 08, 1998, pp. 1159–1175. https://doi.org/10.1142/S0129183198001060.

[26] Wilcox, D. C., "Turbulence Modelling for CFD 3rd Edition," *La Canada CA: DCW industries*, 2006.

[27] Launder, B. E., and Spalding, D. B., "The numerical computation of turbulent flows," *Numerical prediction of flow, heat transfer, turbulence and combustion*, Elsevier, 1983, pp. 96–116. https://doi.org/10.1016/B978-0-08-030937-8.50016-7.

[28] Casalino, D., "An advanced time approach for acoustic analogy predictions," *Journal of Sound and Vibration*, Vol. 261, No. 4, 2003, pp. 583–612. https://doi.org/10.1016/S0022-460X(02)00986-0.

[29] Turner, J. M., and Kim, J. W., "Quadrupole noise generated from a low-speed aerofoil in near-and full-stall conditions," *Journal of Fluid Mechanics*, Vol. 936, 2022, p. A34. https://doi.org/10.1017/jfm.2022.75.

[30] Avallone, F., van den Ende, L., Li, Q., Ragni, D., Casalino, D., Eitelberg, G., and Veldhuis, L., "Aerodynamic and Aeroacoustic Effects of Swirl Recovery Vanes Length," *Journal of Aircraft*, Vol. 56, No. 6, 2019, pp. 2223–2235. https://doi.org/10.2514/1.C035552.

[31] O'meara, M., and Mueller, T. J., "Laminar separation bubble characteristics on an airfoil at low Reynolds numbers," *AIAA journal*, Vol. 25, No. 8, 1987, pp. 1033–1041. https://doi.org/10.2514/3.9739.

[32] Ol, M., McCauliffe, B., Hanff, E., Scholz, U., and Kähler, C., "Comparison of laminar separation bubble measurements on a low Reynolds number airfoil in three facilities," *35th AIAA fluid dynamics conference and exhibit*, 2005, p. 5149. https://doi.org/10.2514/6.2005-5149.

[33] Temmerman, L., and Leschziner, M. A., "Large eddy simulation of separated flow in a streamwise periodic channel constriction," *Second Symposium on Turbulence and Shear Flow Phenomena*, Begel House Inc., 2001. https://doi.org/10.1615/TSFP2.2300.

[34] Temmerman, L., Leschziner, M. A., Mellen, C. P., and Fröhlich, J., "Investigation of wall-function approximations and subgrid-scale models in large eddy simulation of separated flow in a channel with streamwise periodic constrictions," *International Journal of Heat and Fluid Flow*, Vol. 24, No. 2, 2003, pp. 157–180. https://doi.org/10.1016/S0142-727X(02)00222-9.

[35] Kurtz, D., and Marte, J., "A review of aerodynamic noise from propellers, rotors, and lift fans," Tech. Rep. 32-1462, Jet Propulsion Laboratory, Jan. 1970. URL https://ntrs.nasa.gov/citations/19700005920.

[36] Williams, J. F., and Hawkings, D., "Theory relating to the noise of rotating machinery," *Journal of Sound and Vibration*, Vol. 10, No. 1, 1969, pp. 10–21. https://doi.org/10.1016/0022-460X(69)90125-4.

Highlights

1. First in-detailed aeroacoustic analysis of propeller operation at negative thrust conditions.
2. 2-6 times higher fluctuations in integrated thrust in negative thrust conditions compared to the positive thrust conditions.
3. Flow separation becomes the dominant noise source instead of the loading/thickness noise in negative thrust conditions.
4. Propeller operation at negative thrust enables steeper and quieter descent compared to the conventional approach.

Isolated Propeller Aeroacoustics at Positive and Negative Thrust

Jatinder Goyal*[,a], Francesco Avallone†[,b], Tomas Sinnige‡[,a]
[a] *Delft University of Technology, Kluyverweg 1, Delft 2629 HS, The Netherlands*
[b] *Politecnico di Torino, Corso Duca degli Abruzzi 24, Torino 10129, Italy*

Using propellers in negative thrust conditions can potentially result in many benefits, such as a steeper descent, a reduced landing run, reduced community noise, energy regeneration, etc. However, the aerodynamics and aeroacoustics of propellers in this regime are not well understood. This paper presents an aeroacoustic analysis of an isolated propeller operating in both positive and negative thrust conditions, using scale-resolved lattice-Boltzmann very large eddy simulations and the Ffowcs Williams & Hawkings analogy. The propeller was operated at a constant tip Mach number so that any differences in tonal noise between positive and negative thrust conditions were due to changes in blade loading. Results showed that the flow separation around the blades in the negative thrust case led to a 2 to 6 times higher standard deviation in integrated thrust compared to the positive thrust case. The blade loading in the negative thrust case shows the amplitude of fluctuations up to 18% for inboard sections and up to 30% near the blade tip compared to the time-averaged loads. The noise in the propeller plane is 10 dB higher in the positive thrust regime than in the negative thrust regime at a given absolute thrust level of $|T_C| = 0.08$. The lower noise at negative thrust is caused by two factors: the lower magnitude of the negative torque compared to the positive torque at a given thrust level and the shift of the blade loading inboard in the negative thrust condition due to the stall of the blade tip. Along the propeller axis, the negative thrust regime has 13-15 dB higher noise because of the increased broadband noise generated by the flow separation. In the negative thrust case, the noise along the propeller axis (89 dB) and propeller plane (92 dB) are comparable. However, this is not the case for the propulsive case. The comparison of noise in the vicinity of the propeller plane showed that using the propellers in negative thrust conditions allows for a steeper and quieter descent compared to a conventional descent; as long as the magnitude of the negative torque produced is equal to or less than the torque required to operate the propeller in a conventional landing.

*PhD candidate, Wind Energy Section, Faculty of Aerospace Engineering; J.Goyal@tudelft.nl.
†Assistant professor, Department of Mechanical and Aerospace Engineering; francesco.avallone@polito.it.
‡Assistant professor, Flight Performance and Propulsion Section, Faculty of Aerospace Engineering; T.Sinnige@tudelft.nl.

Nomenclature

B	number of propeller blades
c	section chord, m
c_o	speed of sound in dry air at 15° C, m/s
c_d	$D'/q_\infty c$, sectional drag coefficient
C_f	τ_w/q_∞, skin-friction coefficient
c_l	$L'/q_\infty c$, sectional lift coefficient
C_P	$P/\rho_\infty n^3 D_\mathrm{p}^5$, propeller power coefficient
c_q	$Q'/\rho_\infty n^2 D_\mathrm{p}^4$, sectional torque coefficient
C_T	$T/\rho_\infty n^2 D_\mathrm{p}^4$, propeller thrust coefficient
c_t	$T'/\rho_\infty n^2 D_\mathrm{p}^3$, sectional thrust coefficient
C_{P_t}	total-pressure coefficient, $(p_\mathrm{t} - p_\infty)/q_\infty$
D	propeller diameter, m
D'	sectional drag force, N/m
f	frequency, Hz
J	V_∞/nD_p, propeller advance ratio
L'	sectional lift force, N/m
L/D	lift-to-drag ratio
M_ht	$\sqrt{M_\infty^2 + M_\mathrm{tip}^2}$, helicoidal tip rotational Mach number
M_rot	$\Omega r/c_\mathrm{o}$, local radial rotational Mach number
M_tip	$\Omega R/c_\mathrm{o}$, tip rotational Mach number
M_∞	Freestream Mach number
n	propeller rotation speed, Hz
P	propeller power, W
p	static pressure, Pa
P'_C	$P'/\rho_\infty V_\infty^3 D_\mathrm{p}$, sectional power coefficient based on freestream dynamic pressure
p_ref	reference sound pressure, Pa
p_t	total pressure, Pa
P_C	$P/\rho_\infty V_\infty^3 D_\mathrm{p}^2$, propeller power coefficient based on freestream dynamic pressure
Q	torque, Nm
q	$\rho V^2/2$, dynamic pressure, Pa
R	propeller radius, m
r	radial coordinate, m
Re_c	Reynolds number based on chord of the propeller blade
T	propeller thrust, N
t	section thickness, m
T'_C	$T'/\rho_\infty V_\infty^2 D_\mathrm{p}$, sectional thrust coefficient based on freestream dynamic pressure
T_C	$T/\rho_\infty V_\infty^2 D_\mathrm{p}^2$, propeller thrust coefficient based on freestream dynamic pressure
V_∞	freestream velocity, m/s
V_a	axial velocity, m/s
V_t	tangential velocity, m/s
V_eff	sectional effective velocity, m/s
x	Axial coordinate, m
y^+	dimensionless wall distance
BPF	$B \cdot n$, blade passing frequency, Hz
N	No. of elements on a VR level
OSPL	overall sound pressure level, dB
PSD	power spectrum density, dB/Hz

Greek Symbols

α	angle of attack, deg
$\beta_{0.7R}$	blade pitch angle at 70% of the radius, deg
η_p	TV_∞/P, propeller efficiency
η_t	P/TV_∞, turbine efficiency
Ω	$2\pi n$, rotational speed in rad/s
ϕ	phase angle, deg
ρ	air density, kg/m^3
σ	standard deviation

τ_w	wall shear stress, Pa	∞	freestream
θ	axial directivity angle, deg	FWH	Ffowcs Williams & Hawkings
Subscripts/Superscripts		HM	Hanson's model
$'$	per unit span		

I. Introduction

The increasing need for sustainable aviation has triggered many new technologies in the field of aviation. The use of fuel cells, hydrogen combustion, and electric architectures are a few examples of these technologies. These technologies are generally coupled with open rotors because of their high propulsive efficiency (up to moderate Mach number and at low cruise altitudes) [1] to increase the system's overall performance. One additional benefit of electric propulsion is that propellers can be operated at a negative thrust settings that can be beneficial for achieving steeper descent, reduced landing run, better maneuverability [2, 3], reduced community noise [4], and regeneration of energy.

A propeller can produce negative thrust by adjusting the blade pitch and/or the rotational speed so that angles of attack at the blade sections become such that negative lift is produced (figure 1). The generation of negative thrust is accompanied by the production of torque, which can be converted to electrical energy to power the electrical systems onboard. Pipistrel has already proven the feasibility of the concept by optimizing a propeller simultaneously for both propulsive and regenerative regimes, leading to 19% energy savings for a small electric trainer aircraft [5]. Though propellers operating at negative thrust were already investigated in 1933 and 1944 to study their effectiveness as aerodynamic brakes [2, 3], the concept did not gain much attention. It became relevant again with the advent of electric flight and its potential as a control device for the descent/landing phase.

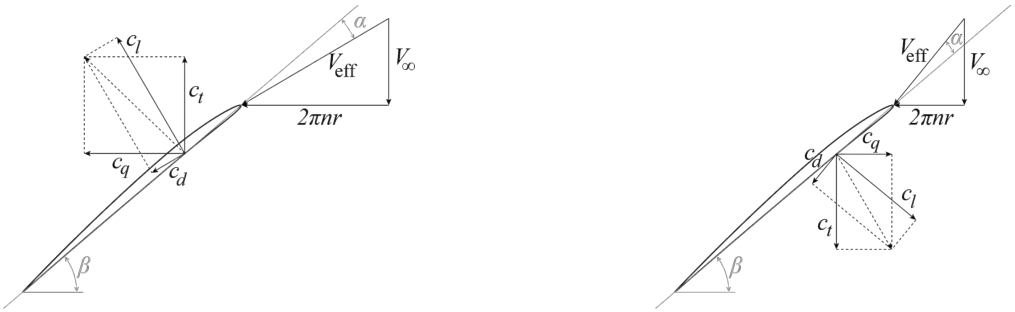

(a) Positive thrust mode **(b) Negative thrust mode**

Fig. 1 Velocity triangles at a fixed-pitch propeller blade section in positive and negative thrust modes [6]

For a typical aircraft configuration, the propeller design is expected to be dominated by the propulsive phases, i.e., climb and cruise. Therefore, operation in the negative thrust mode will represent an off-design condition. In previous papers [6–8], the aerodynamic phenomena of a conventional unducted propeller in the negative thrust regime have been investigated using RANS simulations and experiments. These studies have shown that negative thrust conditions lead to

almost fully separated flow around the blades of a conventional propeller. Due to limitations in terms of the extent of instrumentation, the experiments give limited information about the flow characteristics near the propeller blades and in the slipstream. Also, RANS simulations face difficulty in accurately predicting the flow separation due to the limitations of turbulence modeling [9, 10]. Therefore, higher-fidelity numerical simulations are needed to overcome these challenges. Such simulations can also provide information about the unsteadiness of the flowfield, which is expected to be relevant for aerodynamic and aeroacoustic interaction with a lifting surface immersed in the propeller slipstream.

Further, the literature on the aeroacoustics of propellers operating in the negative thrust regime is almost nonexistent. To the authors' best knowledge, only two studies [4, 7] exist that investigated the aeroacoustics of negative thrust propellers. In the ref. [4], the rotor aeroacoustics were not investigated in detail; instead, the main focus was the potential impact on community noise. In the ref. [7], only tonal noise characteristics were investigated using an analytical model (Hanson's model [11]), and no assessment was made for the broadband noise. As the propeller operates in the stall or near stall conditions in the negative thrust regime, it is expected that the relative importance of the tonal and broadband noise will change along with noise directivity and noise level compared to the propulsive regime. The flow separation on the blades could lead to a dominant broadband noise and even structural vibrations and associated structure-borne noise. However, no paper on these research gaps can be found in the literature.

This paper aims to investigate the aerodynamics and far-field acoustic characteristics of a conventional propeller operating in the negative thrust regime using lattice-Boltzmann (LB) very large-eddy simulations (VLES) coupled with the Ffowcs Williams and Hawkings (FWH) integral solution based on Farassat's formulation 1A [12]. The numerical setup has been validated using experimental data from ref. [8]. An analysis has been done at a constant freestream and tip rotation Mach number by varying propeller pitch to characterize the aerodynamics and aeroacoustics of the propeller at equal Mach number and Reynolds number in both positive and negative thrust regimes.

II. Computational Setup

The numerical setup was validated with the experimental data from ref. [8]. The data available from the experiments dictated the geometry and operating conditions used during the validation. For the subsequent analyses, the operational conditions were modified to be more similar to those experienced in free flight. The rotor geometry is given here first. Then, the methodology is explained, along with the computational setup.

A. Rotor Geometry

The rotor used in this study is TUD-XPROP, which is a scaled version of a propeller for a previous-generation regional turboprop aircraft. The rotor has a diameter of 0.4064 m and a hub diameter of 0.092 m. The nacelle of the rotor extended up to approximately $1.6D$ downstream. Originally, the propeller had six blades; however, only three

blades were used for this study due to limitations of the experimental facility [8]. The propeller can be seen in figure 2a along with its geometry parameters in figure 2b.

(a) Isolated propeller with three blades installed on a sting

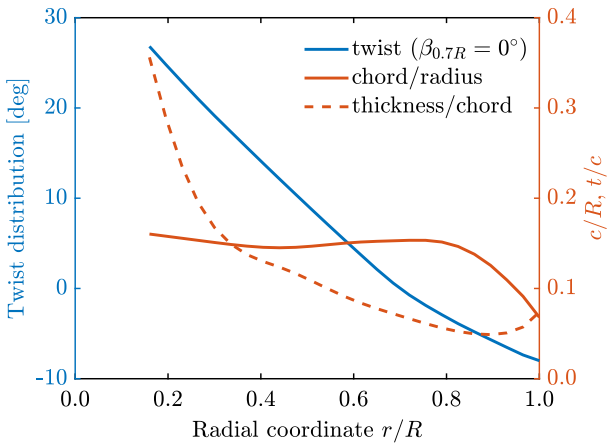

(b) Propeller blade geometry

Fig. 2 Propeller setup and geometry

B. Methodology

LB-VLES simulations have been chosen for this study for two main reasons. The first reason is the method's past proven record for capturing the tonal and broadband noise in similar applications [13, 14]. Secondly, due to the low dissipation and dispersion [15, 16], the LB-VLES simulations were deemed suitable for this study. A detailed description of the LBM can be found in the refs. [17] and [18]. For the simulations, the beta version of the commercial solver PowerFLOW 6-2021 by 3DS Simulia has been used, which has been introduced in ref. [19]. This beta version is especially suitable for the current application as it does not require a zig-zag trip to switch to the scale-resolving solver. Using a zig-zag trip can modify the flow separation and the broadband noise behavior [20, 21], which is relevant for this research and, therefore, a change in behavior due to the artificial introduction of turbulence is not desired. The volume of the domain is discretized using a Cartesian mesh. In total, 19 discrete velocities are used in three dimensions (D3Q19) for this study, including a third-order truncation of the Chapman-Enskog expansion. An explicit time integration approach is used to solve the equations at the Courant-Friedrichs-Lewy (CFL) number of 1 for stability. The particle distribution is obtained using a collision term based on a unique Galilean invariant [22], and equilibrium distribution of Maxwell-Boltzmann [23]. A very-large eddy simulation (VLES) model is implemented in PowerFLOW to take into account the effect of the subgrid unresolved scales of turbulence, which uses $k - \epsilon$ renormalization equations [24] to compute the turbulent relaxation time. The no-slip boundary condition on walls is approximated using a pressure-gradient extended wall model [25, 26]. The model is based on an extension of the generalized law-of-the-wall model [27] to take into account the effect of the pressure gradient on the boundary layer development.

A hybrid CFD/CAA approach has been used in this study to compute the far-field noise. Such an approach is an

ideal solution to avoid excessive computational costs related to resolving the propagation of acoustic waves to the far field. The FWH analogy was solved based on the forward-time solution [28] of Farassat's formulation 1A [12] using the post-processing software SIMULIA PowerACOUSTIC. This formulation includes surface integrals, i.e., acoustic monopoles (thickness noise) and dipoles (loading noise) terms. The volume integral, i.e., quadrupole term, is neglected in this formulation which accounts for the non-linear effects in the volume surrounding the integration surface. The quadrupole term was assumed to be negligible for the operating conditions considered in this paper as the convective Mach number of the propeller wake is less than 0.3 [29].

C. Computational Volume and Boundary Conditions

The computational domain is a cube with a domain size of $128D$ in all three directions (figure 3a). The boundary conditions were specified as a velocity inlet combined with a pressure outlet and slip walls. It was made sure that the total pressure profile was uniform at the inlet. Due to the large size of the domain, the impact of the boundary conditions on the solution is expected to be minimal. The no-slip condition was used for the propeller blades, spinner, and nacelle. For sliding mesh, a volume of revolution was defined around the propeller blades and spinner. In the radial direction, a clearance of $0.1R$ was defined between the blade tip and the outer edge of the rotating domain. Similarly, in the axial direction, a clearance of $0.05R$ was defined between the spinner edge and the edge of the rotating domain. In total, 13 variable resolution (VR) regions were used based on the ref. [30]. The cell volume changes by a factor of 8 between different VR regions. The finest three VR regions (VR13-11) were used around the propeller to accurately capture the flow around the propeller blades, as marked in figure 3b. VR10 was used in the sliding domain and downstream of the sliding domain up to $0.5R$. Further downstream, VR10 is used in a hollow cylinder to capture the strong gradients of tip vortices. VR9 was used in the cylinder encapsulating the propeller blades, spinner, and blade with a radius of $1.2R$ and extended $1R$ upstream and $3.5R$ downstream of the propeller. Other VR regions (1-8) were there to ensure that the domain was large enough to minimize any spurious acoustic reflections from the boundaries of the domain. Further, an acoustic sponge was used to absorb any remaining acoustic reflections coming from the boundaries by exponentially varying the kinematic viscosity per unit temperature from 0.005 $m^2/(s.K)$ at $15R$ up to 0.5 $m^2/(s.K)$ at $30R$ as shown in figure 3a. As the acoustic sponge starts at a $15R$ distance from the propeller, its effect on the aerodynamic results is assumed to be minimal.

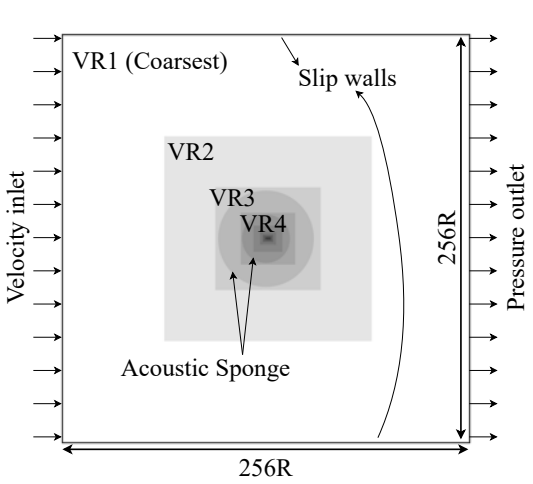

(a) Full computational domain

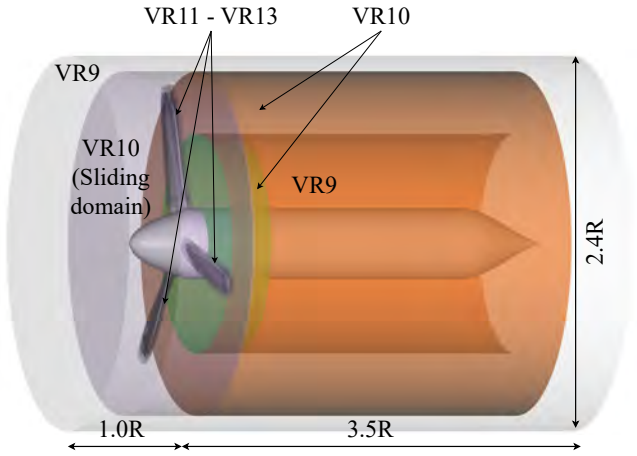

(b) Zoomed view of domain showing the distribution of VR regions near the propeller

Fig. 3 Computational domain and boundary conditions along with the VR regions

III. Grid Dependence Study and Comparison with Experiments

For the grid dependence study, two operating conditions have been chosen with a pitch angle of 15° at $0.7R$ of the blade, for which extensive experimental data were available for validation [8]. The two conditions were chosen as the most challenging ones to reproduce numerically. The first one is a positive thrust condition with a moderate thrust at an advance ratio (J) of 0.60. The given pitch angle is not optimal for propulsive operation and leads to separation near the trailing edge [7]. Therefore, if the grid results are converged for such an operating condition, it can be safely assumed to be converged for other positive thrust conditions with fully attached flow. However, the grid convergence in the positive thrust regime does not ensure the convergence in the negative thrust regime because of significant flow separation around the blades in that condition[6, 7]. The second condition is the negative thrust condition at $J = 1.10$, close to the maximum power output point. The details of these operating conditions can be found in table 1.

Table 1 Operating conditions for grid dependence study

J	V_∞ [m/s]	n [Hz]	M_{ht}	max Re_c
0.60	30	123.03	0.47	3.5×10^5
1.10	30	67.11	0.27	2.0×10^5

Five different grids were compared for the grid dependence study with fine equivalent voxels varying from 1 million to 100 million, based on the previous study by Avallone et al. [30]. The fine equivalent elements represent the number of elements (N) weighted by the time stepping rate, which is proportional to the mesh resolution level (VR level) and is

calculated as follows:

$$\text{Fine equivalent} = \frac{\text{N(finest scale)}}{2^0} + \frac{\text{N(2nd finest scale)}}{2^1} + \frac{\text{N(3rd finest scale)}}{2^2} + ... + \frac{\text{N(coarsest)}}{2^{\text{(n grid levels-1)}}}$$

The details of the grids can be found in table 2, where resolution is defined as the number of fine equivalent voxels per characteristic length. The characteristic length is chosen to be chord at $0.7R$ blade span, which is approximately 31 mm.

Table 2 Grids used for the grid dependence study

		Positive thrust ($J = 0.60$)			Negative thrust ($J = 1.10$)		
Grid name	Grid label	Fine equivalent voxels	Resolution	$y^+_{0.7R,0.5c}$ (Front side)	Fine equivalent voxels	Resolution	$y^+_{0.7R,0.5c}$ (Front side)
very coarse	5	1,231,315	76	108	1,694,093	87	54
coarse	4	8,229,841	152	55	5,244,431	130	37
medium	3	26,780,737	228	34	23,134,459	217	22
fine	2	62,314,804	304	24	62,029,252	304	15
very fine	1	120,353,406	380	16	92,072,521	347	12

The setup was defined such that the blade-passing period of the propeller was an integral multiple of the time-step, which helps to avoid interpolation error in phase-locked and per-rotation averaged measurements. As the rotational speeds of the propeller are different at the chosen operating conditions, the chosen time-step is also different, resulting in a different resolution and mesh sizes. The flow was simulated for twelve revolutions for the medium grid (Grid 3) and used for seeding all the other resolutions. All the other resolutions were simulated for ten revolutions. For all the grids, the last eight revolutions were used for the measurements after ensuring that the transient period was over.

A. Convergence and Validation Study of Aerodynamic Properties

The integrated performance parameters, thrust coefficient C_T and power coefficient C_P, were used to verify the convergence of the integrated performance of the propeller and were compared with the experimental values. Further, the radial distributions of the time-averaged total pressure coefficient have been used to verify the convergence of the slipstream flowfield. Additional validation of the setup has been performed by comparing the phase-locked axial and tangential velocity fields in the slipstream with the experimental data.

1. Integral Performance Parameters

The figure 4 shows the C_T and C_P time-averaged over the last eight revolutions for the different grids compared to the experimental value. The uncertainty of the experimental data is indicated using the shaded areas around the mean results. The standard deviation of the simulated thrust values is also shown using the shaded areas with an averaging period of six revolutions to provide a measure of the load fluctuations over the averaged rotations. The trends of the grid-dependence study have been supported with the help of skin friction contours and shearlines along the blade surface shown in figure 5 for the fine grid (Grid 2). The streamlines are also shown around three blade sections at radial coordinates of $0.3R$, $0.6R$, and $0.9R$, respectively.

In the positive thrust condition shown in Figure 4a, the experimental thrust coefficient has an uncertainty of 2.5%, and the power coefficient has an uncertainty of 1.5%. The standard deviation of the simulated values is almost negligible, indicating the steadiness of the loads on the propeller blades. It is observed that C_T stays almost constant for Grid 4, Grid 3, and Grid 2 (coarse, medium, and fine, respectively). However, for Grid 1 (very fine), the thrust coefficient is increased by approximately 4% compared to Grid 2, 3, and 4. This trend can be explained as follows. As the propeller is operating at a comparatively low Reynolds number (3.5×10^5 based on the propeller chord at $0.7R$), a leading-edge separation bubble exists on both sides of the propeller blade as can be seen in figure 5a. The blade sections between $0.4R$ - $0.7R$ radial coordinate are on the verge of the trailing-edge separation on the pressure side, as indicated by the outward motion of shearlines at these locations. However, the prediction of the location of the separation bubble along the chord is very sensitive to the resolution of the boundary layer (y^+) besides the other parameters, such as incoming turbulence, surface roughness, and subgrid-scale modeling [31–34]. For such cases, having $y^+ \leq 1$ would be the ideal solution. However, as octree meshes are used in PowerFLOW, it becomes practically challenging to reach such y^+ values. Upto Grid 2, the y^+ values are greater than 20 on almost the whole blade surface on the suction side (front), see Table 2. However, the y^+ values are below 20 for Grid 1, which improves the prediction of laminar to turbulence transition [19], leading to a better thrust match with the experimental value for Grid 1 (very fine). The differences in the predicted trailing and leading edge separations along the blade span between different grids result in fluctuations in power coefficient (C_P) values between Grid 3, 2, and 1. The C_T predictions by LBM simulations are in good agreement with the experimental thrust for all the grids except Grid 5. However, the prediction of C_P is off by 10-11%., indicating that the drag is underpredicted by the LBM simulation leading to a low power value.

For the negative thrust condition shown in Figure 4b, the uncertainty in experimental measurements and the standard deviation of simulation values are less than 1%. The convergence of thrust and power is achieved for the fine grid (Grid 2) with 10% underprediction in thrust and 10% overprediction in power compared to the experiment. The significant difference in the simulated integrated performance compared to the experimental data comes from the fact that there is a leading-edge separation bubble on the suction side (back) around the blade sections starting from the root until the radial coordinate of $0.85R$, see figure 5b. Further outboard, the blade sections are fully separated. It is known from literature

[31–34] that even the separation-bubble length is very sensitive to subgrid-scale modeling and grid quality, making it extremely difficult to capture this condition accurately in the numerical simulation. Moreover, the low Reynolds number in this operating condition (2.0×10^5 based on the propeller chord at $0.7R$) results in a trailing-edge separation on the pressure side (front) of the propeller blade. As there is a significant difference in the extent of flow separation between the two regimes (figure 5), Grid 2 was considered good enough to understand the relative change in aerodynamic and aeroacoustic characteristics between the positive and negative thrust regimes.

The slipstream characteristics have been compared with the experimental data in the next subsection to scrutinize further the results obtained from LBM simulations. The very coarse grid (Grid 5) has been omitted in further comparisons to keep the discussion clear and concise.

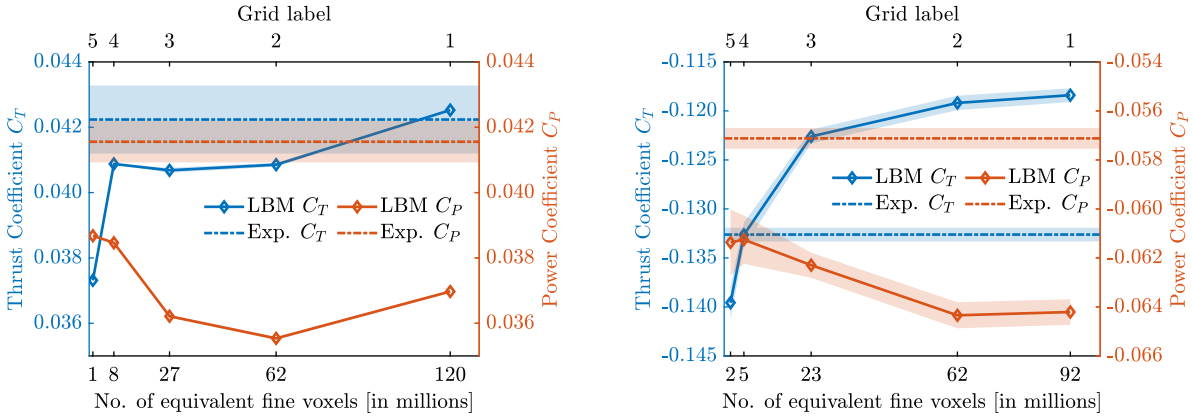

(a) Positive thrust condition (J = 0.60) **(b) Negative thrust condition (J = 1.10)**

Fig. 4 Effect of mesh refinement on the predicted integrated thrust and power

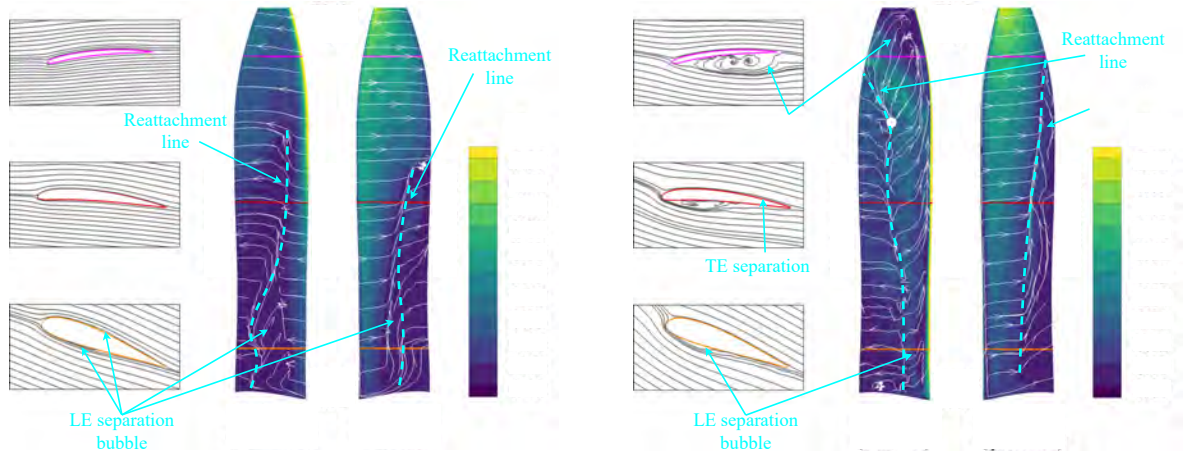

(a) Positive thrust Condition (J = 0.60) **(b) Negative thrust Condition (J = 1.10)**

Fig. 5 Visualization of flow around the propeller blade using skin friction coefficient and shear lines (fine grid)

2. Slipstream

The radial distributions of the time-averaged total pressure coefficient obtained from LBM simulations in the slipstream at $0.15R$ downstream of the propeller (figure 6) have been compared with the experimental data [8] to evaluate the validity of LBM simulations. For $J = 0.60$ in figure 6a, The total pressure coefficient profile is similar for different grids except between the radial coordinate of $0.5R$ - $0.7R$. Besides the fluctuating peak values at the radial coordinate of $0.6R$ between different grids, the medium grid shows different radial gradients between $0.5R$ to $0.6R$. This is expected to be a consequence of the presence of a leading-edge separation bubble along with the trailing-edge separation onset as shown in figure 5a. At this operating condition, the blade tip is negatively loaded due to local negative angles of attack (figure 6a), as explained by ref. [8]. The experimental data shows a negative total pressure coefficient for $0.92 \leq r/R \leq 1$. However, in the simulations, the total pressure coefficient is negative only between $0.98 \leq r/R \leq 1$, resulting in a lower power requirement for a given thrust. The simulations underestimate the maximum value of the total pressure distribution, which is offset by overestimation in the outboard sections, resulting in a thrust value close to the experimental value. Thus the blade loading distribution obtained from the simulations is expected to differ from that obtained in the experiments.

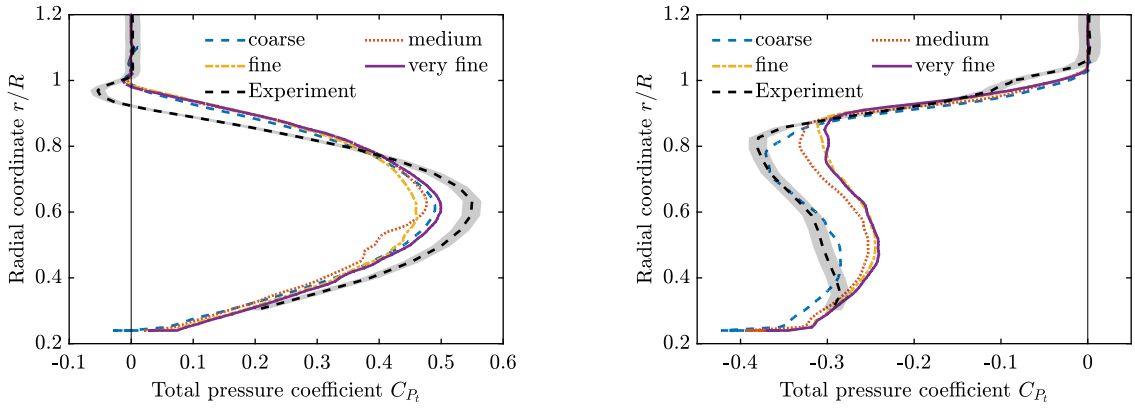

(a) Positive thrust condition ($J = 0.60$) **(b) Negative thrust condition ($J = 1.10$)**

Fig. 6 Radial distributions of time-averaged total pressure coefficient at $0.15R$ downstream of the propeller centre

Figure 6b shows the time-averaged total pressure profile for the negative thrust condition ($J = 1.10$). Looking at the convergence behavior, it is evident that the slipstream converges to a similar profile for fine and very fine grids. Except near the root (below the radial coordinate of $0.4R$), the total pressure distributions are similar in terms of gradients in the radial direction between simulations and experiments. Quantitatively, the total pressure distribution over the 10% most outboard blade radius matches with the experiment. At 40%-90% of blade radius, there is an overprediction of the total pressure, which agrees with the underprediction of the negative thrust observed in figure 4b. As the blade tip is completely separated (figure 5b), it is comparatively easier to predict in numerical simulations than a separated region

with reattachment. It results in a good agreement for the outboard blade span for all the grids. However, the blade span between the root and the radial coordinate of $0.85R$ has separation at the leading edge with reattachment near the trailing edge. As the reattachment location is sensitive to the grid, it results in differences between the simulation and the experiment [31–34]. The gradients of total pressure coefficient profiles in the radial direction are almost insensitive to the choice of the considered grids for both positive and negative thrust regimes, except for the medium grid between $0.5R$ - $0.6R$ for the positive thrust condition. Based on these comparisons, the fine grid was considered a good choice for this study and has been used for further comparison with the phase-locked PIV data [8].

The simulated phase-locked axial and tangential velocity fields have been compared with particle image velocimetry (PIV) data at 0° phase angle (ϕ) with respect to the propeller blade. The definition of the phase angle is shown in figure 7. Figure 8 and 9 show the comparison of phase-locked axial and tangential velocities for the positive ($J = 0.60$) and negative thrust condition ($J = 1.10$), respectively. In these figures, the contours of axial and tangential velocity components in the slipstream of the propeller are shown on the right part of the figure, along with the radial line plots at three different axial locations shown on the left. The contours on the top are obtained from PIV data, while those on the bottom are obtained from the current numerical simulations. The first radial line is close to the propeller blades ($x/R = 0.10$) for both operating conditions. The remaining two axial positions have been chosen such that one cuts the tip vortex, and the other is between two tip vortices. These radial lines are located at $x/R = 0.37$ and 0.60 for positive thrust and at $x/R = 0.40$ and 0.70 for negative thrust. The chosen axial positions are different between the two operating conditions due to their different advance ratios leading to a different pitch between the tip vortices (i.e., different helix angles of the slipstream).

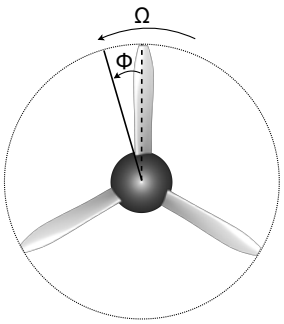

Fig. 7 Definition of phase angle (ϕ)

In figures 8a and 8b, the velocity gradients near the tip vortices are larger in LBM simulations compared to the PIV data, and the tip vortices are shifted slightly outwards in the LBM results compared to the PIV data. These differences could originate from the slightly different blade loading. Such differences would lead to a difference in the local velocity in the slipstream, which means that the flow structures would also convect downstream at different velocities. Since the contours are shown at a fixed streamwise position in figures 8a and 8b, their position relative to the flow structures would

differ, resulting in a relatively large offset in induced velocities. Other reasons could be a possible uncertainty in the blade position or minor inaccuracies in the calibration of the PIV setup leading to a slight displacement of the data with respect to the actual physical coordinates. The line plots show that the gradients in the radial direction are adequately captured by LBM simulations, though the peak is slightly underpredicted, which is consistent with observations from figure 6.

Figure 9 shows the same comparison for the negative thrust condition. The edge of the slipstream is at a higher radial coordinate in the LBM results compared to the PIV data, as seen in the contours and the left-down corner line plot ($x/R = 0.7$). Again the gradients in the radial direction from the LBM data are in agreement with the PIV data. LBM simulations overpredict the peak of phase-locked axial velocity compared to experiments at $x/R = 0.1$ (figure 9a), which contradicts the time-averaged total pressure profile seen in figure 6b and the time-averaged axial velocity results shown in figure 10a. This apparent inconsistency is suspected to be a consequence of uncertainty in the phase-locked blade position in the experiment. To validate this hypothesis, a new comparison with the phase-locked PIV data at $x/R = 0.1$ is shown with arbitrary phase angles of 1°, 2°, and 5° in figure 10b. The LBM simulation no longer overpredicts the peak at $x/R = 0.1$; instead, there is an underprediction that agrees with figure 10a, supporting the validity of the hypothesis.

Based on the comparison of the total pressure coefficient and axial and tangential velocities in the propeller slipstream, it has been proven that the fine grid (Grid 2) is able to predict the slipstream characteristics in terms of gradients in the radial and axial direction. Thus the fine grid is deemed suitable for the further comparison of the aerodynamic characteristics of the positive and negative thrust regimes.

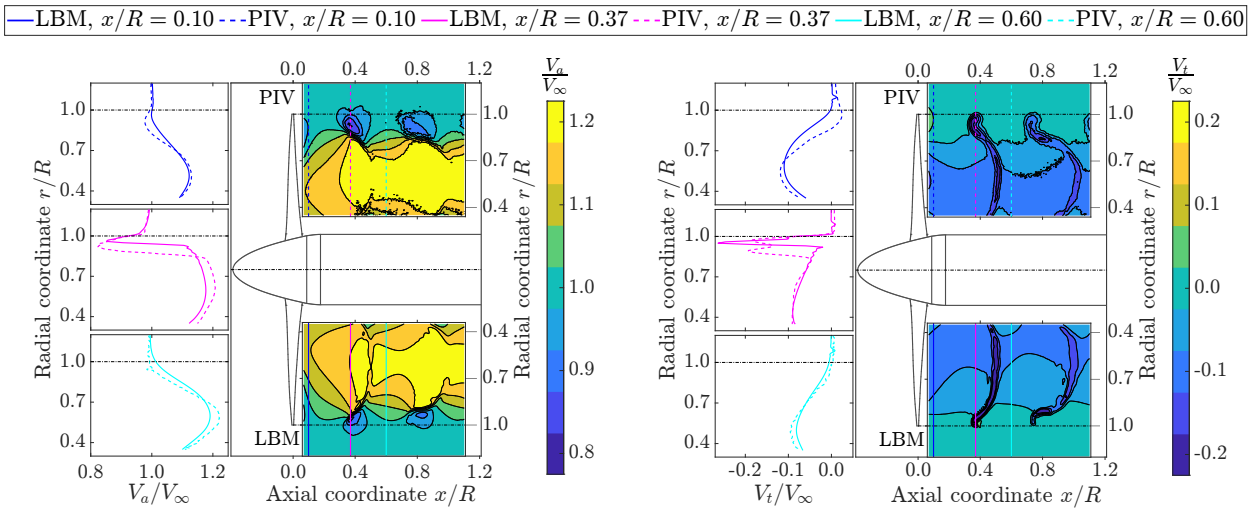

(a) Axial velocity **(b) Tangential velocity**

Fig. 8 Comparison of the phase-locked slipstream from PIV data and LBM simulations for the positive thrust condition at $\phi = 0°$ ($J = 0.60$, fine grid)

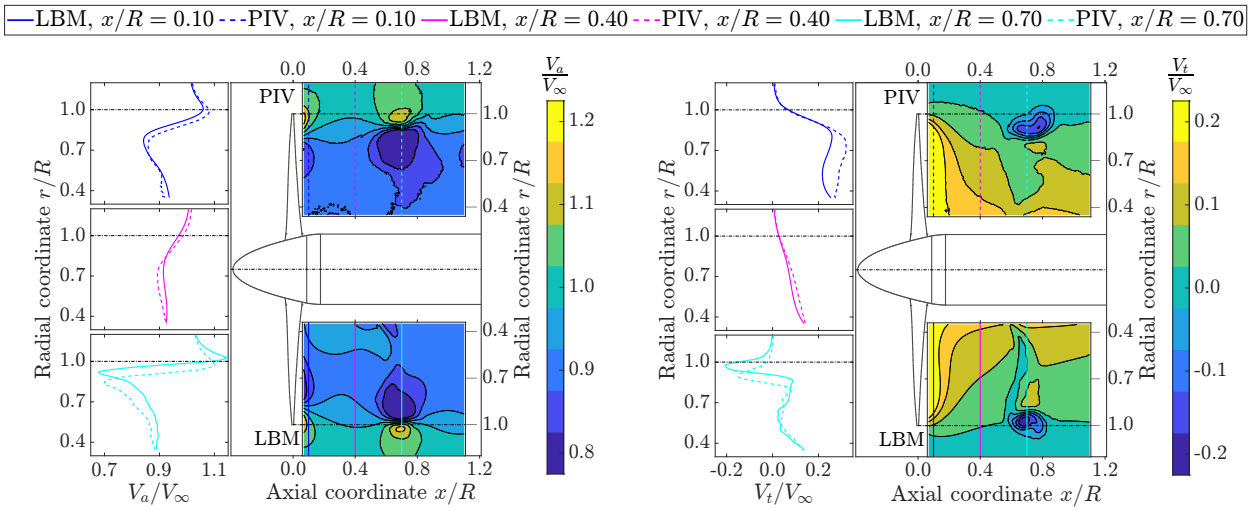

(a) Axial velocity **(b) Tangential velocity**

Fig. 9 Comparison of the phase-locked slipstream from PIV data and LBM simulations for the negative thrust condition at $\phi = 0°$ ($J = 1.10$, fine grid)

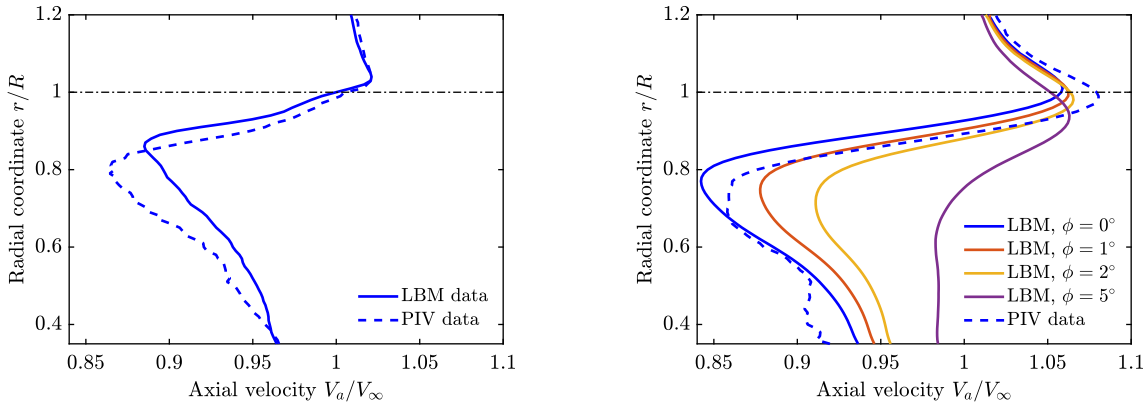

(a) Time-averaged **(b) Phase-locked**

Fig. 10 Time-averaged and phase-locked axial velocity profile at $x/R = 0.10$ for the negative thrust condition ($J = 1.10$, fine grid)

B. Convergence Study of Far-field Aeroacoustics

As the dominant noise sources are anticipated to be within the first 10 BPFs [35], the aeroacoustic convergence has been determined by comparing the directivity patterns of overall sound pressure level (OSPL) for the range of 0.5 - 10 BPF. As LBM simulations work with a cartesian mesh, the three blades of the propeller have different discretization resulting in a different blade loading. This difference was up to ±4% for the positive thrust condition ($J = 0.60$) compared to the blade-averaged loading and up to ±1% for the negative thrust condition ($J = 1.10$). This difference in the blade loading leads to tonal noise at a frequency of (1/3) times the BPF in the power spectrum density (figure 12b); therefore, the lowest frequency is chosen to be 0.5 BPF to eliminate the contribution from this numerical noise source.

The OSPL was calculated using the FWH analogy on a ring with a radius of $20R$, with the axis aligned with the propeller plane and the center coinciding with the propeller center to ensure that the observer is in the far field. The OSPL directivity patterns for both configurations are shown in figure 11. The trends are shown for half of the ring ($\theta = 0^\circ - 180^\circ$) because of the axisymmetric inflow condition, where $\theta = 0^\circ$ lies along the propeller axis in front of the propeller and $\theta = 90^\circ$ lies in the propeller plane. Additionally, the power spectrum density (PSD) is shown for the fine grid (Grid 2) in figure 12 for two locations - propeller plane ($\theta = 90^\circ$) and propeller axis ($\theta = 0^\circ$).

For the positive thrust condition (figure 11a), the OSPL between 45° and 150° is almost identical between the different grids with differences below 1 dB as a consequence of similar blade loading along the blade span. For the negative thrust condition (figure 11b), the difference in OSPL for different grids is below 1 dB at all the directivity angles except the coarse grid. In the propeller plane, tonal noise is the most dominant noise source, as seen in figure 12b. Since there are minute differences in blade loading between different grids, as previously shown in figure 6, the match of OSPL levels in the propeller plane between different grids is an expected trend. In the propeller plane, the first three BPFs are dominant for the positive thrust condition compared to only the first BPF in the negative thrust condition; see figure 12b. The 1/3 BPF caused by the different meshing of the three blades of the propeller is about 25-30 dB lower than the first BPF and thus did not affect the interpretation of the aeroacoustic results.

The broadband noise is expected to be the most dominant source along the propeller axis [35], which is indeed the case (figure 12a) for the given operating conditions. In the positive thrust condition, the main sources of broadband noise are expected to be trailing-edge noise and vortex shedding due to flow separation (figure 5a). The prediction of broadband noise levels is sensitive to the resolution of the relevant turbulent scales. The coarse grid does not sufficiently resolve these turbulent scales, resulting in low (broadband) noise along the propeller axis. However, the medium and the other grids are fine enough to capture these effects, as visible in OSPL levels. The OSPL increases from the medium to the fine grid due to the better resolution of the turbulence on the latter. A further refinement in the grid results in a decrease of 3 dB along the propeller axis from the fine grid to the very fine grid. Therefore, there is an oscillatory convergence. For noise along the propeller axis, prediction within 3 dB is considered enough for this study. Flow separation is the main source of broadband noise for the negative thrust condition. Due to strong flow separation in this condition (figure 5b), the turbulent scales are expected to be larger than for the positive thrust case. The medium and finer grids predict similar noise levels along the propeller axis with differences below 1 dB.

In the positive thrust condition, the noise in the propeller plane is about 12 dB higher than the noise along the propeller axis, which is an expected trend for conventional operation. However, the trend is reversed for the negative thrust condition, i.e., the noise along the propeller axis is 11-12 dB higher than the noise in the propeller plane. This change in directivity is because of two reasons: a) the flow separation in the negative thrust condition significantly increases the broadband noise compared to the positive thrust condition (4-7 dB along the propeller axis); b) lower tonal noise in the negative thrust condition compared to the positive thrust condition (20 dB in the propeller plane), because

of the lower blade-tip rotational Mach number and the lower absolute blade loading.

From the above comparisons, it is observed that the fine grid (Grid 2) is able to determine the changes in the noise source characteristics between the positive and negative thrust regimes. Hence, it is considered good enough for further analysis.

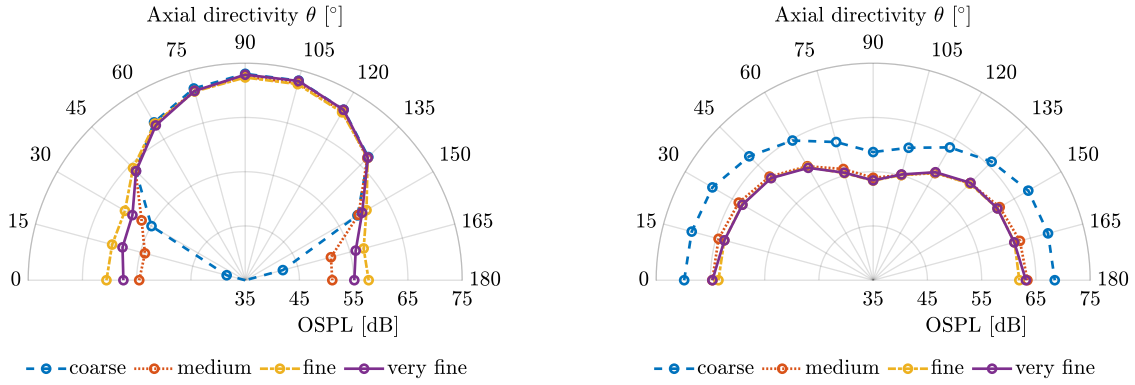

(a) Positive thrust condition (J = 0.60) **(b) Negative thrust condition (J = 1.10)**

Fig. 11 Effect of different grids on the OSPL directivity patterns

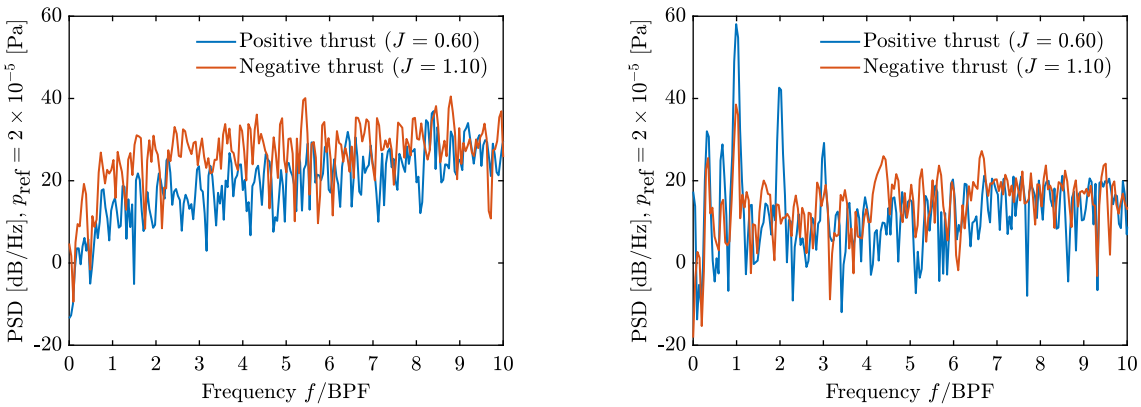

(a) Upstream along propeller axis (θ = 0°) **(b) Propeller plane (θ = 90°)**

Fig. 12 Power spectrum density at θ = 0 and 90° for positive thrust and negative thrust conditions (fine grid)

IV. Results

A propeller operating at a constant speed was used to study the far-field aeroacoustics of the negative thrust regime compared to the conventional positive thrust regime. Given the constant helical tip Mach number, the thickness noise does not change between the operational modes; therefore, it is easier to identify the changes in various noise sources due to the change in thrust and power (both direction and magnitude). The operational conditions were chosen based on a preliminary mission analysis of an ATR-42 aircraft with a relatively steep descent (5.5°). The resulting freestream Mach

number was 0.29. The helicoidal tip Mach number was set to 0.74 to achieve reasonable similarity with a full-scale turboprop propeller. For this study, the simulations were performed at 0° angle of attack with respect to the propeller so that there was no periodic unsteady loading on the blades. In a realistic configuration, this would be an additional noise source. However, it was decided to eliminate this noise source in this study for ease of interpretation of the results. The pitch angle of the blade was changed from 10° to 45° with a step of 5° to vary the propeller loading. As the propeller is operated at a fixed advance ratio, there was only a single operating point at which the propeller operated at its peak efficiency for the selected advance ratio. However, this was deemed acceptable because a difference in tip Mach number would affect the comparison more significantly than the obtained differences in propeller efficiency. An additional pitch setting with $\beta_{0.7R} = 37.57°$ was evaluated to match the absolute thrust obtained at $\beta_{0.7R} = 20°$, which has been used to evaluate the changes in noise sources due to the change in the operating regime (negative to positive thrust condition). The choice of $\beta_{0.7R} = 20°$ as the reference for comparing the two regimes at an absolute thrust level was based on the earlier-mentioned preliminary mission analysis of an ATR-42 aircraft.

A. Aerodynamic Performance

Figure 13 shows the differences in the instantaneous flow features around the propeller blades between the positive and negative thrust regimes for $T_C = \pm 0.08$ at 37.57° and 20° pitch settings respectively. These figures show the skin friction coefficient contours and shearlines at the blade surface for the two conditions. In addition, streamlines are shown around three blade sections located at $0.3R$, $0.6R$, and $0.9R$. Figure 13a shows that the flow is attached along the whole blade span on the back side of the propeller for $T_C = +0.08$, except for the inboard sections that exhibit the presence of a separation bubble. The front side of the propeller shows a separation bubble at the mid-chord position, which can also be seen in the streamlines around the $0.3R$ blade section. This separation bubble is present from the root until around $0.35R$ and moves towards the trailing edge with increasing radial coordinate. For the blade sections present outboard of $0.35R$, the separation bubble extends up to the trailing edge resulting in trailing-edge separation as seen in the streamlines around the blade sections at $0.6R$ and $0.9R$.

For the negative thrust condition ($T_C = -0.08$), the flow is attached on the front (pressure) side of the propeller, except near the trailing edge on the inboard sections (around $0.5R$- $0.8R$), see figure 13b. There is a trailing edge separation at these blade sections, as also indicated by the streamlines around the $0.6R$ blade section. On the back side of the propeller, the flow is attached only for a small portion of the chord near the leading edge, as indicated by the separation line. This leading-edge separation is a consequence of the operation of the blade sections at high negative angles of attack (as shown using streamlines around $0.3R$, $0.6R$ and 0.9). This trend is consistent with previous studies [6, 7].

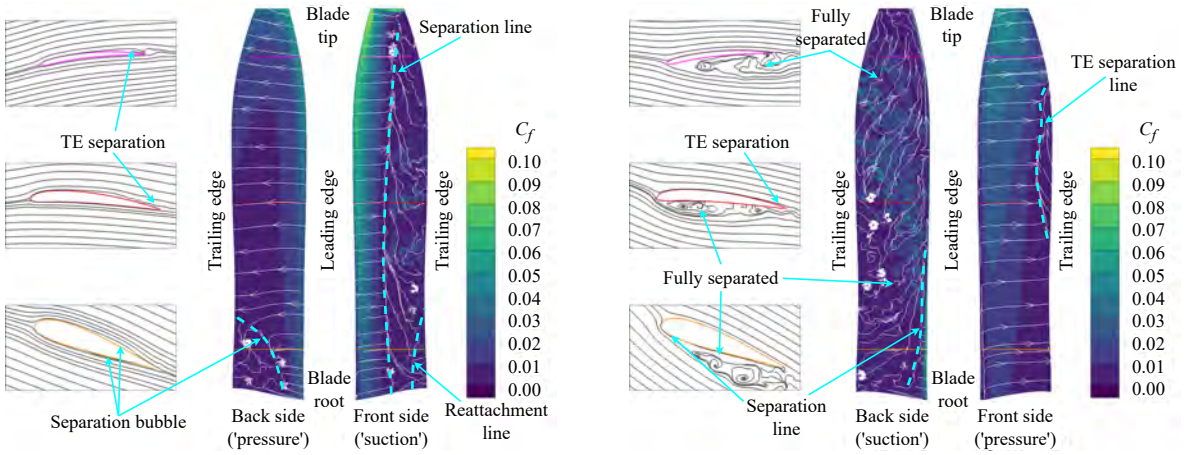

(a) $T_C = +0.08, \beta_{0.7R} = 37.57°$ **(b) $T_C = -0.08, \beta_{0.7R} = 20.00°$**

Fig. 13 Visualization of instantaneous flow around the propeller blade using skin friction coefficient and shear lines for $T_C = \pm 0.08$

1. Time-Averaged Performance Analysis

Figure 14 shows the effect of the varying pitch on the propeller performance. As the advance ratio and freestream Mach number are constant for the analysis, the inflow angle is also constant (31.4° at $r/R = 0.7$, ignoring induction), see figure 15. Therefore, the lower the pitch angle, the more negative the angle of attack (AoA). Similarly, the higher the pitch angle, the higher the AoA. For the pitch angles up to 30°, the blade section at $r/R = 0.7$ operates at negative angles of attack. As the pitch angle is increased from 10° to 30°, the negative angles of attack at blade sections are reduced, which in turn reduces drag and negative lift. As both lift and drag contribute to the negative thrust, a monotonic trend of T_C is seen in figure 14a. On the other hand, the negative power magnitude is reduced by reducing the negative lift and increased by reducing the drag. The opposite nature of these effects results in a maximum power obtainable at a certain pitch for a given operating condition, around 15° in this case, as shown in figure 14a. The transition from negative to positive power occurs around 27.5° (figure 14a). In the positive thrust regime, the drag component opposes the lift component in the thrust direction, whereas both components contribute positively to the power. As the pitch is increased from 30° to 45°, the positive angles of attack increase at the blade sections, increasing lift and drag. Therefore, a monotonic trend is obtained for power in the positive thrust regime. As the flow is still attached around most of the blade for the considered operating conditions (figure 13a), the increase in lift is more than the increase in drag, resulting in an increase of T_C with the increase in pitch angle.

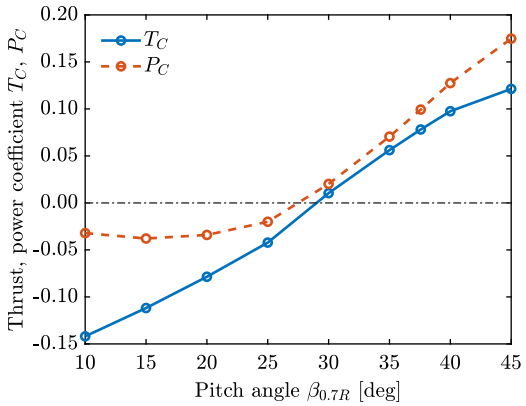

(a) Effect of pitch setting on thrust and power coefficient

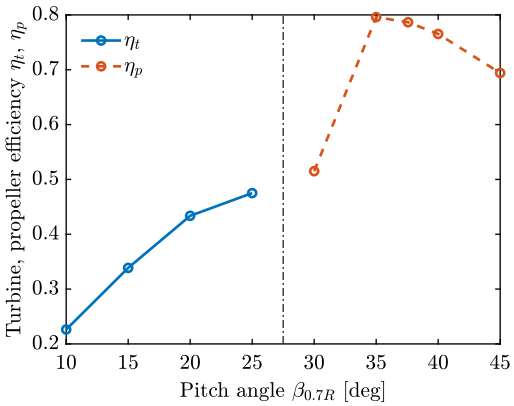

(b) Effect of pitch setting on turbine and propeller efficiency

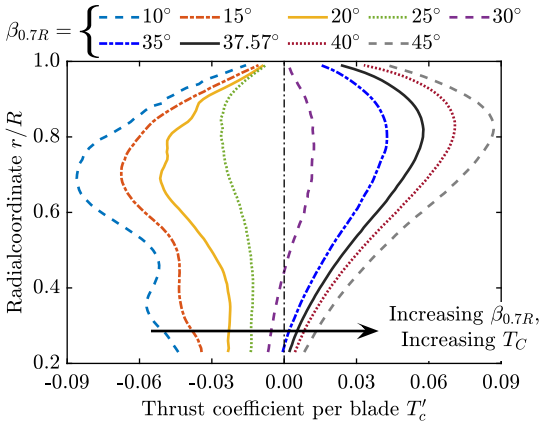

(c) Thrust distribution along the blade span

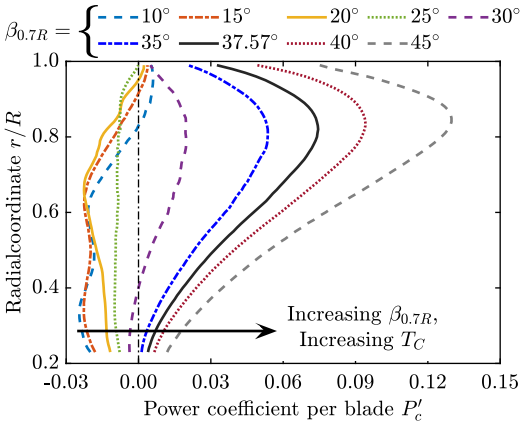

(d) Power distribution along the blade span

Fig. 14 Effect of pitch change on propeller performance at $M_\infty = 0.29$, $M_{ht} = 0.74$ (Time-averaged)

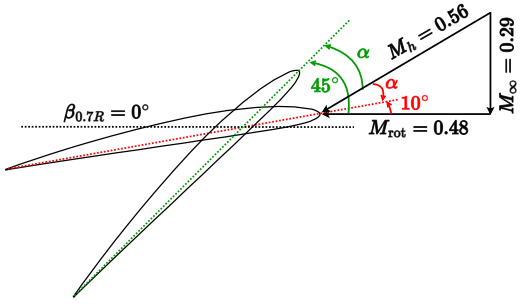

Fig. 15 Velocity triangle for the constant operating condition at different pitch settings at $r/R = 0.7$ (ignoring induction)

Figure 14b shows the variation in the efficiency of the propeller as a function of the pitch setting. Different definitions of efficiency are used for the positive and negative power regimes. The turbine efficiency (η_t), the inverse of the propeller efficiency, has been used for the negative thrust regime. It relates to the shaft power regenerated per unit of negative-propulsive power (TV_∞) produced, while the propeller efficiency (η_p) relates to the propulsive power (TV_∞)

produced per unit of shaft power consumed. A higher turbine efficiency does not necessarily mean higher absolute power regeneration, which can be observed in the current case. The 25° pitch setting gives the highest turbine efficiency (figure 14b), while the 15° pitch setting results in maximum negative power magnitude (figure 14a). At the 25° pitch setting, the flow is still attached on the inboard part of the blade and is separated only on the outboard part. However, as the pitch angle is reduced to 20°, the flow is separated around a larger part of the blade span, resulting in a larger drag increase compared to the lift increase. This results in a larger increase in the negative thrust magnitude compared to the increase in the negative power magnitude resulting in reduced turbine efficiency. As the pitch angle is reduced even further, there is no increase in the regenerated power; however, there is a significant increase in the negative thrust, further steepening the turbine efficiency slope. At 30° pitch, the propeller operates at a very inefficient positive thrust condition due to inboard sections operating in the negative thrust regime (figure 14c). As the pitch angle is increased to 35°, the propeller efficiency increases significantly (80%). With the further increase of pitch angle, the blade sections operate at higher loading and a sub-optimal L/D ratio, especially at 45° pitch, where the efficiency drops to 69%.

The thrust distribution along the blade span in figure 14c shows that the inboard part of the blade has a higher loading in the negative thrust regime than the positive thrust regime. The higher loading near the root is a consequence of higher absolute AoA at negative thrust conditions leading to higher lift and drag. The loading peak is around a radial coordinate of $0.7R$ in the negative thrust operations, in contrast to the positive thrust regime, where the maximum is around $0.85R$. The flow separation around the blade tip shifts the peak inwards in the negative thrust regime; that is why the loading peak is located around $0.8R$ at 25° pitch, which shifts to $0.7R$ at 10° with the increase in flow separation. A local maximum is observed in the thrust distribution around $0.45R$ for the 10° and 15° pitch settings. The local lift magnitude in the negative thrust cases is negatively influenced by the flow separation (reduced Cl) and positively influenced by the increasing dynamic pressure with the increasing radial coordinate. Around $0.45R$, the decrease in the lift due to the flow separation is more than the corresponding increase in dynamic pressure due to the increasing rotational speed with the increasing radial coordinate. Though the drag also adds to the negative thrust magnitude, the major contribution comes from the lift (around 80%). Therefore, the local decrease in the lift magnitude results in a local maximum in the thrust distribution at the radial coordinate of $0.45R$ for 10° and 15° deg pitch settings seen in the figure 14c. The loading distribution for the 30° pitch setting shows that the inboard part of the blade operates in the negative thrust regime with AoA lower than the zero lift AoA. In contrast, the outboard part of the blade operates in the positive thrust regime with AoA higher than the zero lift AoA, resulting in a small positive thrust and power overall.

Figure 14d shows the power distribution along the blade span for different pitch settings. For the positive thrust conditions, the radial loading distribution resembles that of a minimum-induced loss design, with a peak around a radial coordinate of $0.85R$. For the negative thrust conditions, a completely different distribution is obtained where most of the contribution comes from the inboard section with a relatively flat distribution up to the radial coordinate of $0.6R$. The power at outboard sections drops to zero and even goes to positive values at the tip. The positive power at the

tip, along with the negative thrust, indicates that the tip is separated to the extent that the power is consumed by that specific part of the blade (instead of being extracted from the flow) to drag the tip along with the rest of the blade. As the pitch angle is decreased from 25° to 10°, the increased flow separation around the blade tip increases the fraction of the span operating at positive power. The negative power magnitude increases along the whole span from 25° to 20° pitch. The further decrease in pitch from 20° to 15° only redistributes the power along the blade span. The power contribution from the inboard part of the blade increases and from the outboard part decreases with the decrease of the pitch angle, resulting in almost similar power levels at 15° and 20° pitch settings as already seen in figure 14a. A further decrease from 15° to 10° results in a decrease in negative power magnitude from the outboard sections; however, there is a negligible increase in power from the inboard sections, resulting in a lower negative power magnitude overall. The local maxima around $0.45R$ can also be seen in the power distribution of the 10° pitch setting, which results from a decrease in local lift magnitude, as explained before.

2. Unsteady Aerodynamic Performance Analysis

As the propeller is operating at 0° inflow angle, the blade loading is expected to be axisymmetric. That is indeed the case for the positive thrust regime as shown in figure 16a, in which the radial distribution of instantaneous thrust coefficient (T_c') along the blade span is shown as a function of circumferential position. However, the same is not true for the negative thrust regime, as shown in figure 16b. It should be noted that the sign of the instantaneous thrust coefficient (T_c') has been reversed in figure 16b to make the comparison easier with figure 16a. The thrust distribution for the 20° pitch angle shows significant fluctuations over the rotation (amplitude of up to 18% for inboard sections and up to 30% for the blade tip compared to the time-averaged loads). These fluctuations are the result of the flow separation on the back side (suction) of the propeller (figure 13b). The high amplitude and frequency of these fluctuations in the negative thrust regime make the blade loads dynamic rather than static. These changes in the loading may have an impact on the structural integrity of the propeller blades in the negative thrust regime.

The effect of the load fluctuations on the integrated thrust performance (from all blades together) is shown in figure 17a for a total of six rotations. In the positive thrust regime, the fluctuations in the integrated thrust coefficient are below ±1% of time-averaged thrust coefficient, in contrast to the negative thrust regime fluctuations, which are up to ±3%. The fluctuation in the integrated thrust might lead to additional requirements in the power train due to the excitation of the shaft. The amplitude of these fluctuations depends upon the negative thrust level (or the pitch setting in this case). As the negative thrust level increases (i.e., a decrease in pitch angle in this case), the flow separation around the blades increases, leading to an increase in load fluctuations. Figure 17b shows the standard deviation of the integrated thrust normalized with the time-averaged thrust value. The average fluctuation amplitude increases from 0.7% to 1.5% as the negative T_C increases from -0.04 to -0.14. In the positive thrust regime, the sudden increase of the average fluctuation amplitude to 1.2% for $T_C = 0.01$ results from the low normalizing value (T_C). In contrast to the

negative thrust regime, the amplitude of fluctuation is below 0.5% for all the positive thrust conditions. Eventually, the fluctuations in the positive thrust regime would increase once significant flow separation is encountered (at higher pitch settings); however, those settings are considered irrelevant in the current study.

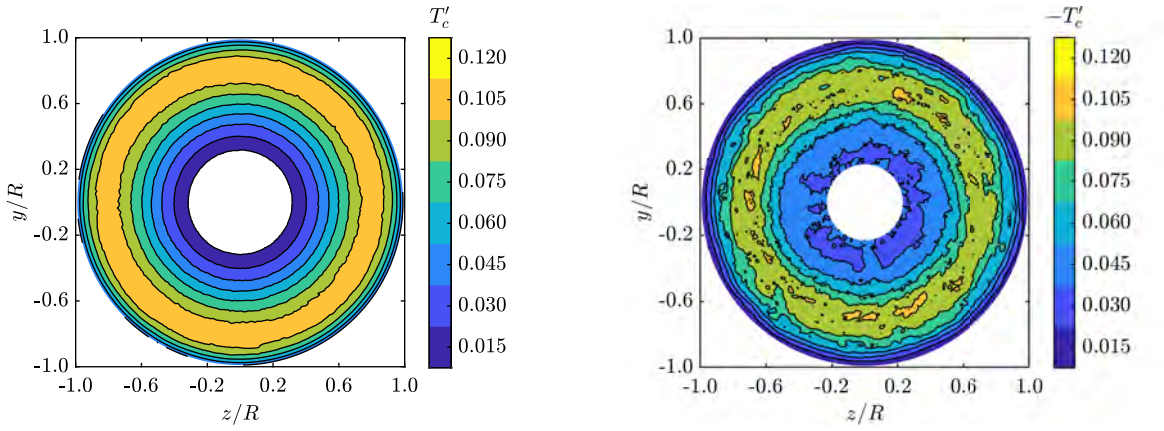

(a) T_C = +0.08, $\beta_{0.7R}$ = 37.57° **(b) T_C = −0.08, $\beta_{0.7R}$ = 20°**

Fig. 16 Radial distribution of instantaneous thrust coefficient (T_c')along the propeller blade span over a rotation as a function of circumferential position for T_C = ±0.08 at J = 1.34, M_∞ = 0.29

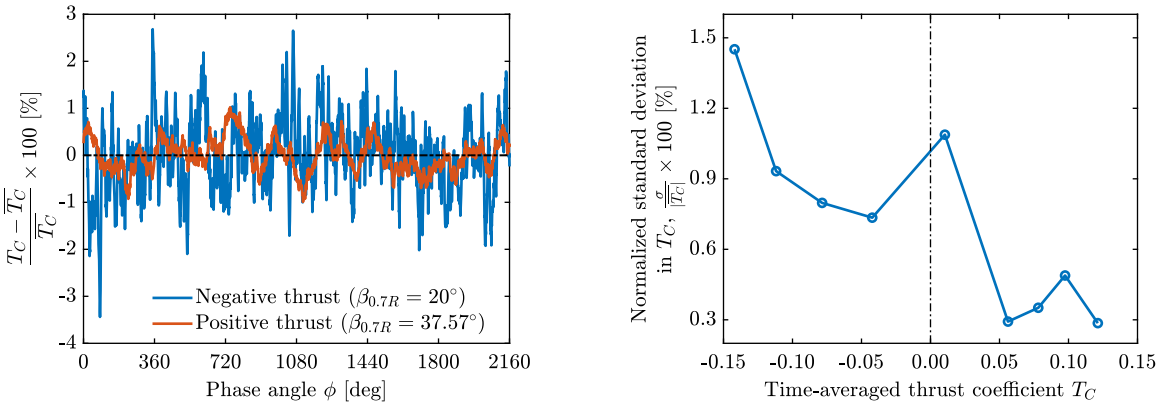

(a) Variation in integrated thrust over multiple rotations for $|T_C|$ = 0.08 **(b) Normalized standard deviation in thrust over six rotations for different pitch settings**

Fig. 17 Time-accurate integrated thrust performance at J = 1.34, M_∞ = 0.29

3. Slipstream

The slipstream in a negative thrust condition is expected to have significantly different characteristics than in a conventional positive thrust condition. The time-accurate data in the slipstream was available from simulations with a 5° resolution for one propeller rotation leading to 72 time instances. From each time instance, three slices aligned with the three propeller blades were extracted. The resulting 216 slices were averaged (given their expected symmetry for uniform inflow) to obtain the final phase-locked results. The phase-locked axial and tangential velocity contours in the

propeller slipstream have been compared in figures 18 and 19 at an absolute thrust level of $|T_C| = 0.08$, corresponding to pitch angles of 20° and 38.93° for negative and positive thrust respectively. Figure 18a and 19a show the contours of the mean of the phase-locked velocities and figures 18b and 19b show contours of the standard deviation of the phase-locked velocities. In these figures, the slipstream contours on the top side of the nacelle show the negative thrust condition, and the slipstream in the positive thrust condition is shown on the bottom side.

As expected, the operation at negative thrust results in decreased axial velocity in the slipstream compared to the freestream condition, whereas the positive thrust results in increased axial velocity. This difference in the axial velocity causes an axial shift of the tip vortex between the two conditions; see figure 18a. Also, the radial gradients where the tip vortex cuts the measurement plane are much higher in the positive thrust case than in the negative thrust condition. As the radial gradients due to the tip vortex at $x/R \approx 1.0$ are diffused over a larger region in the negative thrust case, the region with a higher standard deviation is also spread over a larger region compared to the positive thrust case, as can be seen in figure 18b. These plots also highlight the difference in the shape of the blade wake and tip vortex between the two thrust conditions. In the positive thrust condition, the blade wake is downstream of the tip vortex due to the increased axial velocity. However, the axial velocity is reduced in the negative thrust condition, leading to the tip vortex being downstream of the blade wake.

From the results shown in figure 18, three main inferences can be drawn regarding the nature of fluctuations experienced by a wing surface immersed in such a slipstream. Firstly, an aerodynamic surface immersed in a slipstream at a negative thrust setting would experience reduced dynamic pressure resulting in a reduction in local lift. In contrast, an aerodynamic surface immersed in a slipstream at a positive thrust would experience an increase in local lift. Secondly, as the vortices in the negative thrust regime are expected to be closer to each other due to reduced pitch between the tip vortices (figure 18a), this results in more pressure fluctuations over a wing immersed in a slipstream with negative thrust condition than the positive thrust condition over a given axial distance. Lastly, as can be noticed in figure 18b, the fluctuations due to the tip vortex are concentrated over a small region compared to the negative thrust condition. Therefore, a wing immersed in a slipstream at a positive thrust condition would experience high-amplitude periodic impingement of the tip vortex. On the other hand, a wing immersed in a slipstream at a negative thrust condition would experience comparatively low-amplitude periodic impingement scattered over a comparatively larger area. These inferences will be tested in the follow-up work with the installed configuration.

Figure 19 shows the tangential velocity in the slipstream. This study defines the tangential velocity as positive in the clockwise direction. As expected, the direction of the propeller-induced swirl is in the direction of the rotation of the propeller (anti-clockwise) in the conventional positive thrust regime, see figure 19a. In contrast, as the direction of the torque is reversed in the negative thrust condition, the direction of the propeller-induced swirl is also reversed, i.e., opposite to the propeller rotation. Therefore, the interaction effects with a body immersed in the propeller slipstream operating at negative thrust would be reversed compared to the effects in the positive thrust condition. Moreover, the

gradients in the axial direction near the propeller plane are stronger in the negative thrust condition compared to the positive thrust condition. These differences between the two regimes originate from the differences in blade loading distribution resulting in a different vortex system leading to different inductions in the slipstream. Figure 19b shows the contours of the standard deviation of the phase-locked tangential velocity in the propeller slipstream. The trends are similar to those shown in figure 18b, i.e., the strong fluctuations in the tangential velocity are concentrated in the region where the tip vortex cuts the measurement plane. Similar to figure 18b, figure 19b also shows that the high fluctuation region (around $x/R = 1.0$) is spread over a larger region in the negative thrust condition compared to the positive thrust condition.

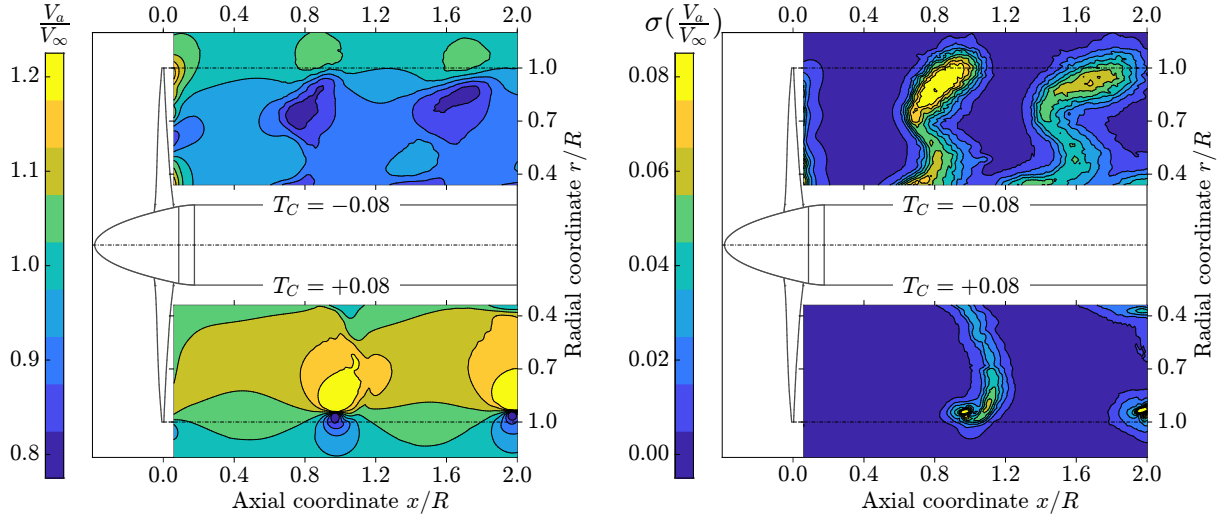

(a) Averaged phase-locked axial velocity

(b) Standard deviation of phase-locked axial velocity

Fig. 18 Comparison of axial velocity contours in negative ($\beta_{0.7R} = 20°$) and positive ($\beta_{0.7R} = 38.93°$) thrust condition at absolute thrust level of $|T_C| = 0.08$ (Phase-locked)

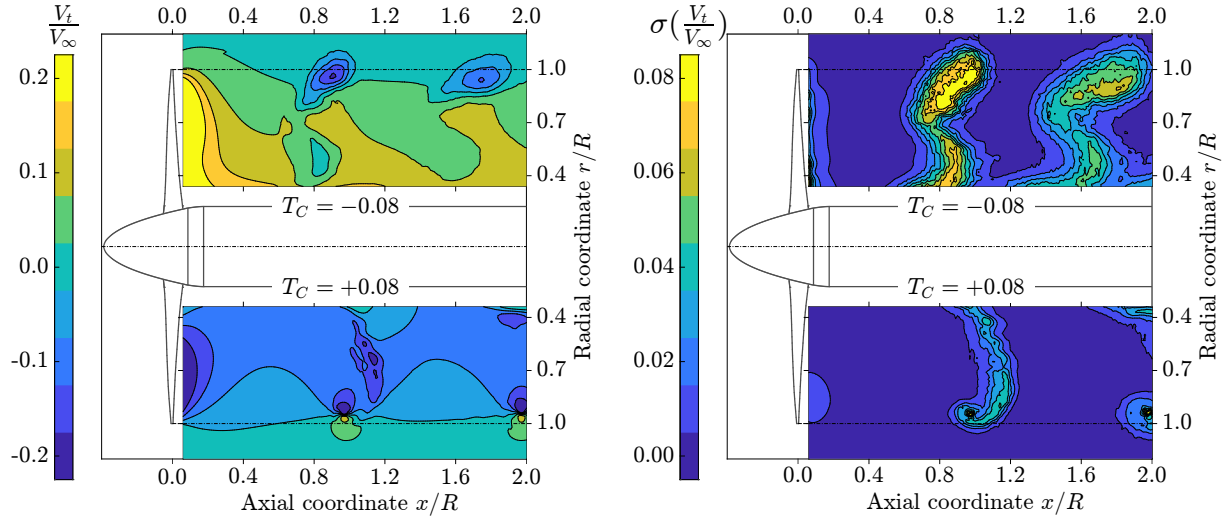

(a) Averaged phase-locked tangential velocity **(b) Standard deviation of phase-locked tangential velocity**

Fig. 19 Comparison of tangential velocity contours in negative ($\beta_{0.7R}$ = 20°) and positive ($\beta_{0.7R}$ = 38.93°) thrust condition at absolute thrust level of $|T_C|$ = 0.08 (Phase-locked)

Figure 20 shows the radial distributions of time-averaged axial and tangential velocity in the slipstream at $1R$ downstream of the propeller center. The axial location for the comparison was based on its relevance for an installed case. The radial distributions of axial velocity in figure 20a display the expected increase in velocity with the increase in thrust for the positive thrust conditions with pitch settings between 30° and 45°. Similarly, the negative thrust conditions show an expected decrease in axial velocity with the increasingly negative thrust value. The radial distributions of axial velocity for 10° and 15° show a local maximum similar to the one seen in the blade loading distributions in figure 14c. In the positive thrust regime, the strong radial gradients of the axial velocity near $r/R = 1$ result from the high spanwise gradients of the loading distribution seen in figure 14c. In contrast, as the spanwise loading gradients are comparatively lower in the negative thrust regime near $r/R = 1$, the corresponding radial gradients of the axial velocity are also lower. The slope steepens with an increase in the magnitude of the negative thrust due to the increase in the corresponding spanwise loading gradients. The increasing blade loading at the inboard sections with the decreasing pitch settings results in decreasing axial velocities in the wake at the corresponding radial coordinates in figure 20a.

As expected, the tangential velocities are opposite in negative thrust conditions compared to the positive thrust condition due to the opposite direction of torque, see figure 20b. High loading at the inboard blade sections in the negative thrust regime results in high tangential velocities at the corresponding radial coordinates in the wake. With the increasing radial coordinate, though the dynamic pressure increases, the power coefficient stays almost constant (figure 14d), resulting in decreasing tangential velocities in the wake. Hence explaining the large radial gradients observed in the negative thrust conditions in figure 20b. In contrast, in positive thrust conditions, the power coefficient increases with the increasing radial coordinate resulting in almost constant tangential velocities in the wake at a given

axial location, as can be seen in figure 20b. At the radial coordinate of 0.9, the power coefficient becomes positive in the negative thrust conditions resulting in negative tangential velocities. From these trends, it becomes clear that a wing immersed in the slipstream of a negative thrust condition will perceive a changed effective angle of attack compared to a positive thrust condition.

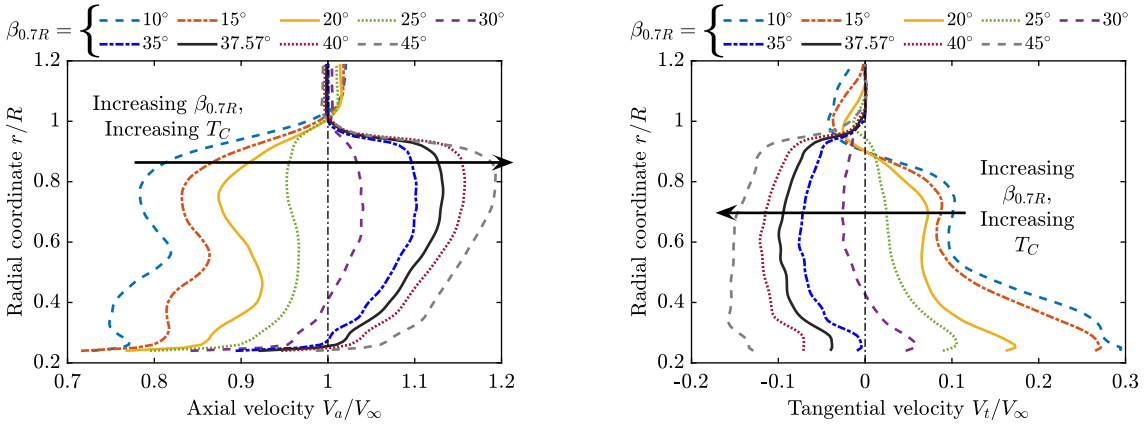

(a) Axial velocity **(b) Tangential velocity**

Fig. 20 Radial distributions of time-averaged axial and tangential velocity in the propeller slipstream at 1*R* downstream of the propeller center

B. Far-field Acoustic Characteristics

The changes in the aerodynamics of the negative thrust regime compared to the conventional positive thrust regime are expected to modify the resulting acoustic emissions. The tonal noise is sensitive to both blade loading and thickness, making it difficult to isolate the changes in the noise sources between the two regimes (positive and negative thrust). Building upon the previous section's discussion, the current section also analyzes the cases with the fixed tip Mach number (different thrust settings achieved through variation in blade pitch setting). This strategy allows studying the changes in the noise characteristics solely due to the change in the blade loading characteristics and not due to a change in thickness noise. The convection effects have been neglected in this analysis as the main interest is in the change of noise mechanism.

1. Far-field Noise Directivity and Power Spectrum Density (PSD)

Figure 21a shows the resulting far-field noise directivity at a distance of 20*R*. The noise directivity has been calculated in two ways. The dash lines with markers are obtained by propagating the pressure signal captured at the blade surface to the far field using the FWH analogy. Therefore, these lines represent the total noise generated by the propeller blades, i.e., the sum of tonal and broadband noise. The solid lines (without markers) are obtained by feeding the time-averaged blade loading shown in figures 14c and 14d to Hanson's model [11] to calculate the tonal noise due to the time-averaged blade loading. The noise can be decomposed into two components using the FWH analogy: loading

noise and thickness noise, based on their respective integral terms [36]. The advantage of using Hanson's model is that it further decomposes the loading noise into the noise due to the thrust and torque.

The dashed black line shows the thickness noise obtained from the FWH analogy, whereas the dotted black line shows the thickness noise obtained using Hanson's model. The FWH analogy gives the total noise obtained from the high-fidelity simulations, whereas Hanson's model gives further insight into the loading noise sources. Comparing the noise levels obtained from the two approaches shows that Hanson's model overpredicts the tonal noise by 2-3 dB for both positive and negative thrust conditions, which originates from the simplifications inherent in Hanson's model [11]. The thickness noise is also overpredicted by 3 dB in the propeller plane. As broadband noise is the primary source of the noise near the propeller axis, the total noise level (predicted by FWH analogy) is higher than the tonal noise levels (predicted by Hanson's model) for $0^\circ \leq \theta < 30^\circ$ and $150^\circ < \theta \leq 180^\circ$. For approximately $30^\circ \leq \theta \leq 150^\circ$, Hansons's model agrees qualitatively with the FWH analogy and can be used to understand the relative importance of different tonal noise sources. Therefore, this analysis with the Hanson model has been used to gain more insight into these noise sources.

The positive thrust condition has 10 dB higher noise in the propeller plane than the negative thrust condition, which is also reflected in the power spectrum density plot shown in figure 22b. This difference in the tonal noise is expected to originate from two sources: a) higher noise due to torque in the positive thrust condition (due to higher torque, see figure 14d); b) differences in blade loading distribution between the two conditions as seen in figure 14c. These sources of difference between the loading noise at positive and negative thrust have been analyzed further by decomposing the loading noise into noise produced by thrust and torque using Hanson's model, see figure 21b. Though the absolute thrust level is the same for both conditions, the more outboard loading in the positive thrust condition leads to a 4 dB higher noise due to thrust. Despite the constant absolute thrust level, the magnitude of the torque is approximately three times higher in the positive thrust condition than in the negative thrust condition. The higher torque amplitude results in up to 12 dB higher noise in the positive thrust condition than in the negative thrust condition. As evident from figure 21b, noise due to torque is the dominant noise for the positive thrust condition for the given operating condition. In contrast, the noise produced by thrust and torque is comparable in the negative thrust condition. For both regimes, the noise due to thrust has two lobes, with the front lobe interfering destructively with the noise due to torque and the back lobe interfering constructively with the noise due to torque, irrespective of thrust direction. This interference trend between noise produced by thrust and torque agrees with the previous studies [7, 35]. As noise levels produced by thrust and torque are comparable in the negative thrust condition, the destructive interference results in a decreased loading noise in front of the propeller plane, as can also be seen in the FWH analogy results in figure 21a. In the positive thrust condition, the noise due to thrust has a small effect on the overall loading noise.

Along the propeller axis ($0^\circ \leq \theta \leq 30^\circ$ and $150^\circ \leq \theta \leq 180^\circ$), the negative thrust condition results in 13-15 dB higher noise than the positive thrust condition along the propeller axis; see the FWH analogy results in figure 21a. This

is an expected result of the increased flow separation in the negative thrust condition compared to the positive thrust condition, as seen in figure 13. The increased broadband noise can also be seen in the power spectrum density plot shown in figure 22a.

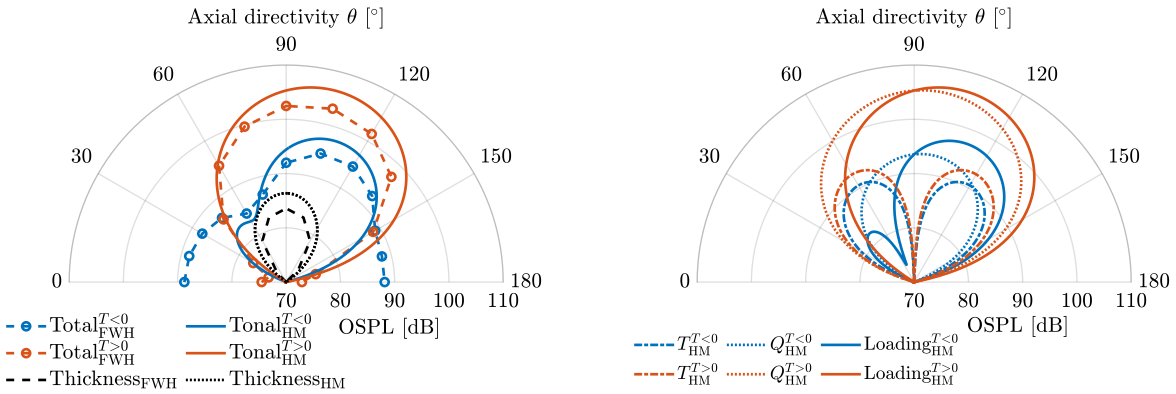

(a) Noise directivity at positive and negative thrust based on FWH analogy and Hanson's model

(b) Contribution of noise produced by thrust and torque to the loading noise based on Hanson's model

Fig. 21 Far-field noise directivity of the propeller in positive and negative thrust regimes at absolute thrust level of $|T_C| = 0.08$

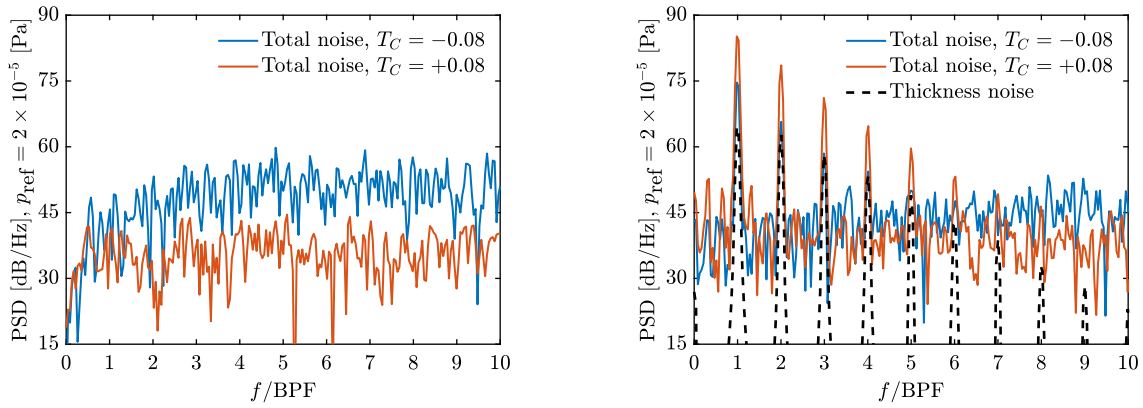

(a) Upstream along propeller axis ($\theta = 0°$)

(b) Propeller plane ($\theta = 90°$)

Fig. 22 Power spectrum density at $\theta = 0$ and 90° for absolute thrust level of $|T_C| = 0.08$

2. Noise Source Map

To further understand the difference between the noise sources in positive and negative thrust conditions, a post-processing tool from 3DS named OptydB-PFNOISESCAN was used. This tool calculates the noise contribution per unit surface area emitted towards a given microphone at every time step, and then Fourier transforms the unsteady surface field to provide output for a given frequency range. The noise contribution of the surfels is calculated in terms of power density, i.e., Pa^2/m^2 and then the resulting value is converted into dB by taking the log, resulting in the units of

dB/m^2. It should be noted that this tool uses the assumption of a compact source, which is a reasonable assumption for the first two BPFs ($M_o c/\lambda < 0.1$) for the given operating conditions ($M_\infty = 0.29, M_{ht} = 0.74$). Nine time instances of the obtained results are shown for one of the blades in figure 23 and figure 24 for $\theta = 0°$ and $90°$ respectively. For $\theta = 0°$, the frequency range was chosen to be 1 - 2 BPF, given the considerable difference in PSD between the two operating conditions seen in figure 22a and constraints imposed by the assumption of a compact source. Similarly, for $\theta = 90°$, the first BPF was chosen to compare the location of tonal noise sources at the given operating conditions based on figure 22b.

Figure 23a and 23c show the noise source maps of the front and back sides of the propeller respectively for a microphone located along the propeller axis ($\theta = 0°$) for $T_C = +0.08$ ($\beta_{0.7R} = 37.57°$). Similarly, figures 23b and 23d show the noise source maps of the front and back sides of the propeller respectively for the same microphone location for $T_C = -0.08$ ($\beta_{0.7R} = 20°$). As the microphone is located along the propeller axis, the noise source contribution is independent of the circumferential position in figure 23. As can be noticed from the figure, broadband noise is dominant for this observer location (figure 22a). Since the inflow turbulence is negligible, the two main sources of broadband noise are trailing-edge noise and flow separation. For the front side of the propeller (figure 23a), the noise mainly comes from the trailing edge. The strong noise sources near the trailing edge can be related to the trailing-edge separation seen in figure 13a. Similarly, on the back side of the propeller, the noise sources are observed at the inboard sections corresponding to the separation bubble seen in figure 13a along with trailing-edge noise sources located relatively outboard.

In contrast, the extensive flow separation on the back side of the propeller in the negative thrust condition (as shown in figure 13b) leads to a dominant broadband noise contribution from the whole back surface of the blade, see figure 23d. Again the inboard region with the attached flow in figure 13b features negligible noise generation radiated to the given microphone. With the increase in local Mach number and pressure amplitude (due to the increased dynamic pressure) in the radial direction, the extent of flow separation also increases from the root to the tip, enhancing the strength of the broadband noise source. For the conventional regime, i.e., positive thrust condition, the front side is the dominant source of broadband noise. In contrast, the back side is the dominant broadband noise source in the negative thrust condition.

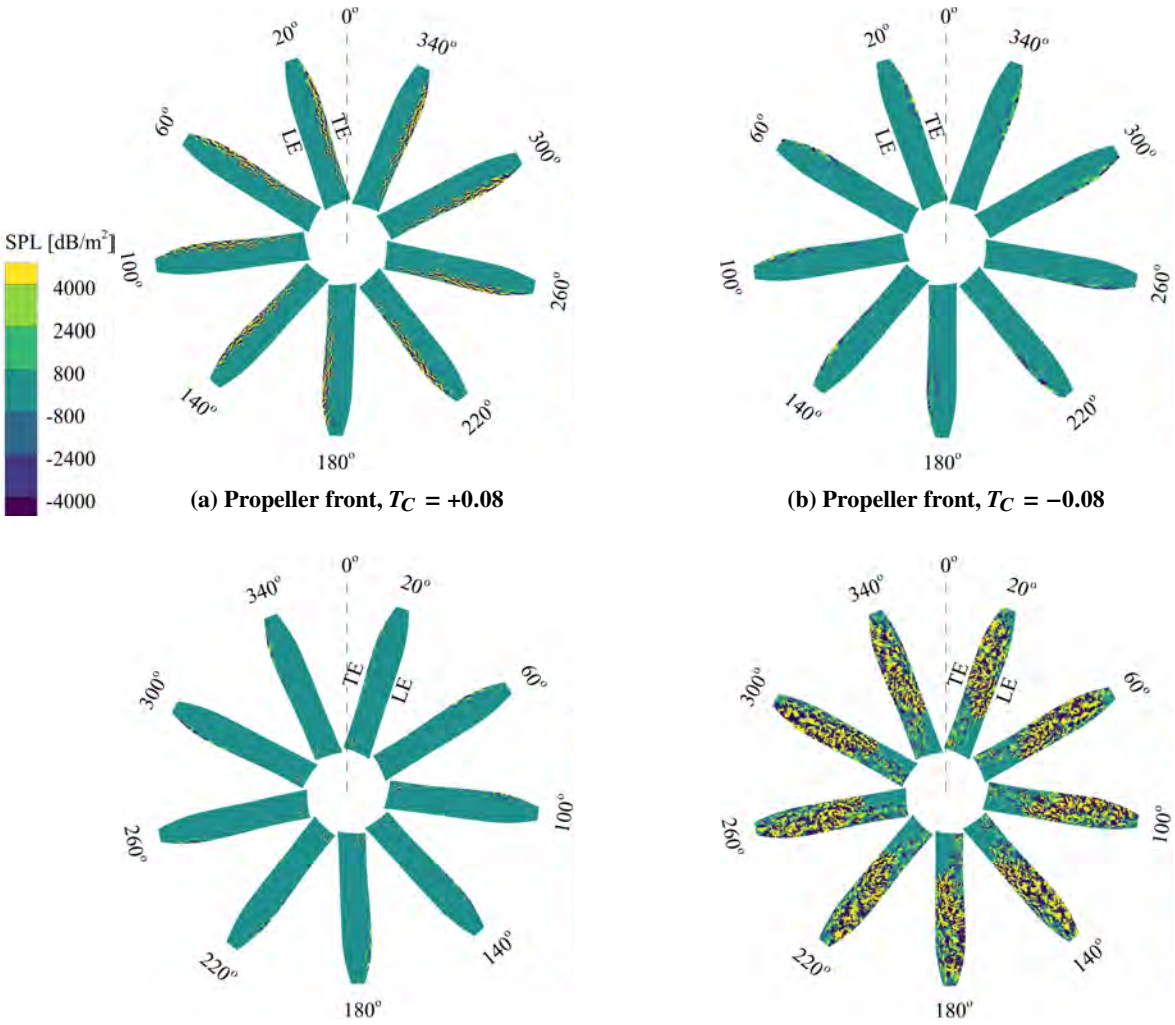

(a) Propeller front, $T_C = +0.08$ **(b) Propeller front, $T_C = -0.08$**

(c) Propeller back, $T_C = +0.08$ **(d) Propeller back, $T_C = -0.08$**

Fig. 23 Noise source map (1 - 2 BPF) on a single propeller blade for an observer located along the propeller axis ($\theta = 0°$) at positive and negative thrust conditions

To compare the distribution of tonal noise source for the two operating conditions, the noise source map for $\theta = 90°$ at the first BPF is shown in figure 24. Because the microphone is located in the propeller plane along the 0° line depicted in the figure, the source contribution varies with the circumferential position. This is a consequence of the varying distance between the blade surface and the microphone due to the rotation of the blade surface. Due to the increase in local Mach number and pressure amplitude (due to the increased dynamic pressure) in the radial direction, the outboard part of the blade has the most dominant contribution to the noise in the propeller plane in the conventional positive thrust regime on both the front and the back side of the propeller (figures 24a and 24c). In the negative thrust case as well, a clear dominant noise source can be seen on the outboard part of the blade on the front side of the propeller (figure 24b) contributing to the tonal noise. However, on the back side of the propeller, random fluctuations are superimposed on a circumferential variation of the source amplitude (figure 24d). This indicates the presence of a combination of tonal and

broadband noise. The tonal noise in the positive thrust condition is higher than in the negative thrust case in figure 24 because of higher torque in the positive thrust case, as explained previously.

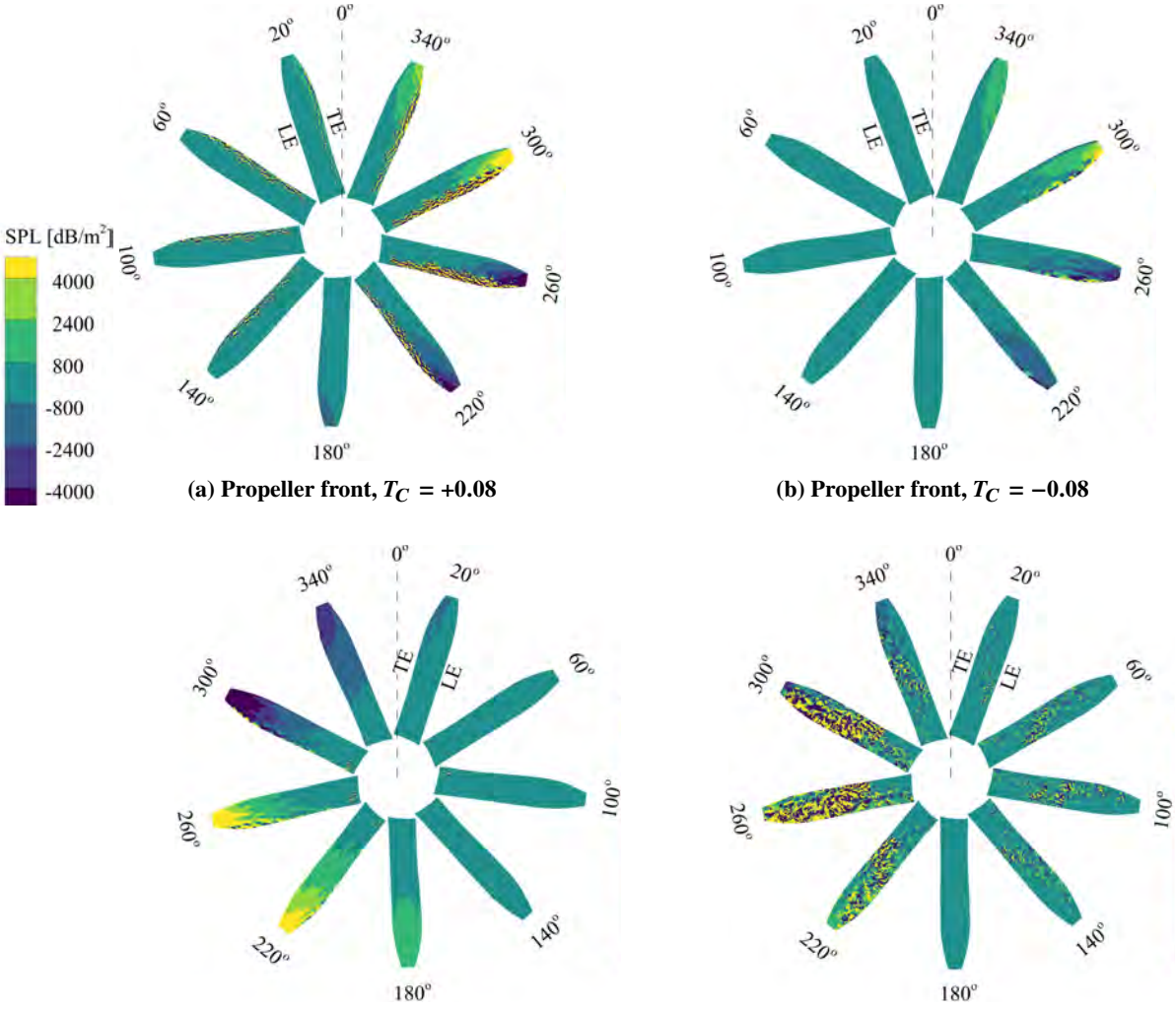

(a) Propeller front, T_C = +0.08 **(b) Propeller front, T_C = −0.08**

(c) Propeller back, T_C = +0.08 **(d) Propeller back, T_C = −0.08**

Fig. 24 Noise source map (1st BPF) on a single propeller blade for an observer located in the propeller plane (θ = 90°) at positive and negative thrust conditions

3. Effect of Thrust Coefficient on OSPL

This section evaluates the effect of the thrust setting on the OSPL. Figure 25a shows the variation of OSPL with the absolute thrust coefficient for both positive and negative thrust regimes using the FWH analogy along the propeller axis (θ = 0°) and in the vicinity of the propeller plane (75° ≤ θ ≤ 105°). The tonal noise in the vicinity of the propeller plane has been decomposed further by using Hanson's model into thrust, torque, and thickness noise, see figure 25b. In figure 25a, the dash-dotted lines show the noise levels along the propeller axis (θ = 0°), where the main contribution comes from the broadband noise sources. The solid lines show the maximum OSPL level between 75° - 105°, where the OSPL is expected to be dominated by tonal noise (see figure 22b). The dashed-black line shows the level of thickness

noise for the given operating condition. The OSPL for the positive thrust condition increases from 71 dB to 80 dB along the propeller axis (dash-dot orange line) when the thrust coefficient increases from 0.01 to approximately 0.12. This is a result of the increase in the broadband noise caused by an increase in trailing-edge separation (figure 13a) with the increase in T_C. Even with the trailing-edge separation, the broadband-dominated noise of the positive thrust regime is considerably lower than that of the negative thrust regime (dash-dot blue line) at all the thrust levels (as expected). The noise along the propeller axis for the negative thrust conditions has a higher positive slope than the positive thrust regime. After a certain thrust level, the broadband-dominated noise level exceeds the tonal-dominated noise levels and becomes the dominant source of the noise. This is a consequence of the significant increase in the broadband noise levels caused by the increasing separation as the magnitude of negative thrust increases.

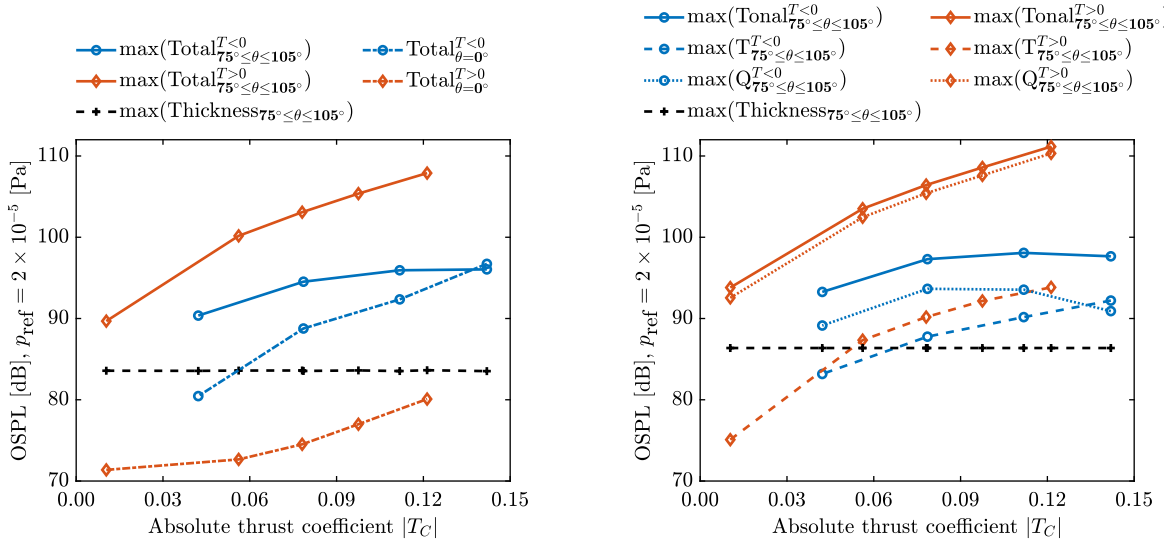

(a) FWH analogy **(b) Hanson's model**

Fig. 25 Effect of thrust coefficient on the noise sources in positive and negative thrust regimes for a propeller operating at a constant rotational speed (M_∞ = 0.29, M_{ht} = 0.74)

On the other hand, the tonal-dominated noise for the positive thrust regime (solid orange line) is considerably higher than the tonal-dominated noise for the negative thrust regime (solid blue line). In the vicinity of the propeller plane, the negative thrust condition with a thrust coefficient of $T_C = -0.04$ produces approximately similar noise as produced in the positive thrust regime at $T_C = +0.01$. The positive thrust regime has a much steeper slope along the whole range of thrust levels than the negative thrust regime (figure 25). In contrast, there is a little increase in the noise near the propeller plane for $|T_C| \geq 0.08$ in the negative thrust regime. These trends can be explained by decomposing the tonal noise into thrust, torque, and thickness noise using Hanson's model is shown in figure 25b. Hanson's model predicts similar trends as the FWH analogy for the noise in the given directivity range. In the vicinity of the propeller plane, the noise due to torque (dotted orange line) is the dominant noise source for the whole thrust range in the positive thrust regime. The same is true for the negative thrust regime up to the maximum regeneration point. As a result,

even though the absolute thrust magnitude in the negative thrust condition ($T_C = -0.04$) is approximately four times higher than the positive thrust condition ($T_C = +0.01$), the tonal noise levels are similar due to the similar magnitude of P_C ($|P_C| = 0.02$), see figure 14a. As in the positive thrust regime, the torque increases with the increasing thrust magnitude, and the tonal noise levels also increase. However, in the negative thrust regime, the operating conditions with $T_C = -0.08$ and -0.11 have similar values of P_C (figure 14a), resulting in similar tonal noise levels. After the maximum regeneration point, the magnitude of the negative torque starts to decrease, whereas the magnitude of the negative thrust continues to increase. As a result, noise due to thrust becomes the dominant noise source after a certain point; see figure 25b. However, such an operating condition probably would not be relevant for an aircraft due to the high magnitude of the negative thrust coefficient.

4. Main Inferences for Landing Using Negative Thrust Settings

Three main inferences can be drawn from the trends observed in figure 25. Firstly, it can be concluded that for a given absolute thrust level, the negative thrust regime can be expected to have lower noise in the propeller plane than the positive thrust regime based on two facts: a) For a given thrust level, the noise due to thrust in positive thrust condition can be expected to be always higher than the noise due to negative thrust due to more outboard loading; b) As concluded in the earlier work [7] as well, the torque required to generate a given thrust level can be expected to be always higher than the torque regenerated at the same absolute thrust level in the negative thrust regime (for a conventional propeller design). As a result, the sum of the noise due to both thrust and torque is expected to be lower in the negative thrust regime compared to the positive thrust regime for a given absolute thrust; therefore, the resulting tonal noise is also expected to be lower. Secondly, it can be concluded that for a conventional propeller, the negative thrust regime is expected to be noisier along the propeller axis than the positive thrust regime, irrespective of the thrust or torque level. Lastly, the noise due to torque is expected to be the dominant noise source in the operating conditions (moderate thrust levels) relevant for a landing using negative thrust. When the negative torque is below the torque required to operate the propeller in a conventional landing, the noise near the propeller plane can be expected to be either lower or similar to the noise generated by the propeller in a conventional landing. A similar torque level in the two regimes is achieved at a higher absolute thrust in the negative thrust regime compared to the conventional positive thrust regime. It essentially means that a steeper descent is possible without increasing the tonal noise (without considering the effects of inflow angle on the tonal noise). Moreover, the steeper descent means that the vicinity of the airport is exposed to the noise for a shorter time and generally at larger distances. This would lead to reduced noise hindrance even at a constant source noise level.

V. Conclusions

A numerical investigation has been carried out using the Lattice-Boltzmann method coupled with a very large-eddy model to understand the aerodynamics and far-field noise characteristics of an isolated propeller operating in positive and negative thrust regimes. The setup has been validated by comparison against experimental data for two operating conditions (J = 0.60, and 1.10). In the case of the positive thrust condition (J = 0.60), the LBM simulations are able to predict the thrust accurately (within 1%). However, the power prediction is off by about 10% due to the underprediction of the drag. The underprediction of drag is expected to occur because of a separation bubble on the blade surface, which makes the prediction of the reattachment location difficult and thus leads to higher uncertainty on the drag. Due to the limitations in simulating separated flow, the negative thrust regime (J = 1.10) simulations underpredict the power and overpredict the thrust by 10%. The comparison of the radial distribution of total pressure, and axial and tangential velocity distributions in the slipstream showed that LBM-VLES simulations are able to capture the gradients in the radial and axial directions despite the differences in the predicted integrated performance. As the LBM-VLES simulations performed in this paper tend to underpredict and overpredict the power for positive and negative thrust regimes, respectively, it can be concluded that the simulations tend to be conservative in the prediction of tonal noise for the positive thrust conditions and overpredict the tonal noise for the negative thrust regime given that the noise due to the torque is dominant at low to moderate thrust settings.

A propeller operating at a constant rotational speed but varying pitch angle was used to investigate the far-field noise characteristics with a freestream Mach number of 0.29 and helicoidal tip rotational Mach number of 0.74. Such a configuration ensures that the thickness noise stays constant as the loading is changed with the variation of pitch setting. The resulting absolute thrust coefficient lies in the range of 0.01 - 0.12 for the positive thrust regime and between 0.04 - 0.14 for the negative thrust regime. As expected, thrust shows a monotonic decreasing trend with the increase in pitch angle in the negative thrust regime. Power reaches a maximum at a unique pitch setting (for the studied propeller at 15°). The blade loading distributions show that the peak in the radial distribution of thrust is located inboard (0.7R) compared to the spanwise location of maximum loading (0.85R) for the positive thrust regime. Moreover, most of the negative power comes from the inboard part of the blade (up to 0.6R) compared to the positive thrust regime, where the maximum power loading is around 0.85R. The flow separation around the blades in the negative thrust regime increases average fluctuations from 0.7% at $T_C \approx -0.04$ to 1.5% at $T_C \approx -0.14$ in the integrated thrust. In comparison, the fluctuations are below 0.5% for all thrust settings in the positive thrust regime. Further, the blade loading in the negative thrust regime shows the amplitude of fluctuations of up to 18% for inboard sections and up to 30% near the blade tip compared to the time-averaged loads. The analysis of the slipstream flowfields shows that an aerodynamic body immersed in a slipstream at a negative thrust setting will experience reduced dynamic pressure and opposite tangential velocity compared to those experienced at a positive thrust setting.

The analysis of the far-field noise characteristics shows that a conventional propeller operating in the negative thrust

regime can be expected to produce more broadband noise than in positive thrust conditions at all practical thrust settings. The tonal noise in the positive thrust regime is higher than in the negative thrust regime for a given absolute thrust. This difference arises from two sources. Firstly, the higher torque leads to higher noise due to torque in the positive thrust regime. Secondly, the higher absolute loading on the inboard blade segments results in a lower noise due to thrust in the negative thrust regime, even though the absolute thrust level is the same. As the noise due to torque is the dominant noise source for low to moderate thrust settings, a steeper and quieter descent compared to a conventional descent is possible using negative thrust as long as the negative torque produced is equal to or lower than the torque required to operate the propeller in a conventional landing (without considering the effect of inflow angle on propeller noise). Additional reduction in noise hindrance is expected due to the steeper descent leading to shorter exposure time to the community noise.

Acknowledgments

The research leading to these results is part of the FUTPRINT50 project. This project has received funding from the European Union's Horizon 2020 Research and Innovation programme under Grant Agreement No 875551. This work made use of the Dutch national e-infrastructure with the support of the SURF Cooperative using grant no. EINF-2733. The authors would like to thank Robert Nederlof for providing the experimental data for the validation of the simulations.

References

[1] Veldhuis, L. L. M., *Propeller wing aerodynamic interference*, Ph.D. Dissertation, Delft University of Technology, Netherlands, 2005. URL http://resolver.tudelft.nl/uuid:8ffbde9c-b483-40de-90e0-97095202fbe3.

[2] Hartman, E. P., "Negative Thrust and Torque Characteristics of an Adjustable-pitch Metal Propeller," *Annual Report-National Advisory Committee for Aeronautics*, Vol. 19, 1933, p. 421. URL http://hdl.handle.net/2060/19930091538.

[3] Hedrick, W. S., and Douglass, W. M., "An Experimental Investigation of the Thrust and Torque Produced by Propellers Used as Aerodynamic Brakes," Tech. Rep. NACA-WR-A-27, National Advisory Committee for Aeronautics, 1944. URL http://hdl.handle.net/2060/19930093338.

[4] Thomas, J. L., and Hansman, R. J., "Community Noise Reduction Assessment of Using Windmilling Drag on Approach by Hybrid Electric Aircraft," *AIAA Aviation 2020 Forum*, AIAA Paper 2020-2877, June 2020. https://doi.org/10.2514/6.2020-2877.

[5] Eržen, D., Andrejašič, M., Lapuh, R., Tomažič, J., Gorup, Č., and Kosel, T., "An Optimal Propeller Design for In-Flight Power Recuperation on an Electric Aircraft," *2018 Aviation Technology, Integration, and Operations Conference*, AIAA Paper 2018-3206, June 2018. https://doi.org/10.2514/6.2018-3206.

[6] Sinnige, T., Stokkermans, T. C. A., van Arnhem, N., and Veldhuis, L. L. M., "Aerodynamic Performance of a Wingtip-Mounted

Tractor Propeller Configuration in Windmilling and Energy-Harvesting Conditions," *AIAA Aviation 2019 Forum*, AIAA Paper 2019-3033, June 2019. https://doi.org/10.2514/6.2019-3033.

[7] Goyal, J., Sinnige, T., Avallone, F., and Ferreira, C., "Aerodynamic and Aeroacoustic Characteristics of an Isolated Propeller at Positive and Negative Thrust," *AIAA Aviation 2021 Forum*, AIAA Paper 2021-2187, June 2021. https://doi.org/10.2514/6.2021-2187.

[8] Nederlof, R., Ragni, D., and Sinnige, T., "Experimental Investigation of the Aerodynamic Performance of a Propeller at Positive and Negative Thrust and Power," *AIAA AVIATION 2022 Forum*, AIAA Paper 2022-3893, June 2022. https://doi.org/10.2514/6.2022-3893.

[9] Szydlowski, J., and Costes, M., "Simulation of Flow Around a Static and Oscillating in Pitch NACA 0015 Airfoil Using URANS and DES," *Heat Transfer Summer Conference*, Vol. 2, Parts A and B, July 2004, pp. 891–908. https://doi.org/10.1115/HT-FED2004-56437.

[10] Shelton, A., Abras, J., Jurenko, R., and Smith, M., "Improving the CFD Predictions of Airfoils in Stall," *43rd AIAA Aerospace Sciences Meeting and Exhibit*, AIAA Paper 2005-1227, 2005. https://doi.org/10.2514/6.2005-1227.

[11] Hanson, D. B., "Helicoidal surface theory for harmonic noise of propellers in the far field," *AIAA Journal*, Vol. 18, No. 10, 1980, pp. 1213–1220. https://doi.org/10.2514/3.50873.

[12] Farassat, F., and Succi, G. P., "A review of propeller discrete frequency noise prediction technology with emphasis on two current methods for time domain calculations," *Journal of Sound and Vibration*, Vol. 71, No. 3, 1980, pp. 399–419. https://doi.org/10.1016/0022-460X(80)90422-8.

[13] Casalino, D., Hazir, A., and Mann, A., "Turbofan broadband noise prediction using the Lattice Boltzmann Method," *AIAA Journal*, Vol. 56, No. 2, 2018, pp. 609–628. https://doi.org/10.2514/1.J055674.

[14] Gonzalez-Martino, I., and Casalino, D., "Fan tonal and broadband noise simulations at transonic operating conditions using lattice-Boltzmann methods," *2018 AIAA/CEAS Aeroacoustics Conference*, 2018, p. 3919. https://doi.org/10.2514/6.2018-3919.

[15] Bres, G., Pérot, F., and Freed, D., "Properties of the lattice Boltzmann method for acoustics," *15th AIAA/CEAS Aeroacoustics Conference (30th AIAA Aeroacoustics Conference)*, 2009, p. 3395. https://doi.org/10.2514/6.2009-3395.

[16] Marié, S., Ricot, D., and Sagaut, P., "Comparison between lattice Boltzmann method and Navier–Stokes high order schemes for computational aeroacoustics," *Journal of Computational Physics*, Vol. 228, No. 4, 2009, pp. 1056–1070. https://doi.org/10.1016/j.jcp.2008.10.021.

[17] Succi, S., *The lattice Boltzmann equation: for fluid dynamics and beyond*, Oxford university press, 2001. https://doi.org/10.1063/1.1537916.

[18] Shan, X., Yuan, X.-F., and Chen, H., "Kinetic theory representation of hydrodynamics: a way beyond the Navier–Stokes equation," *Journal of Fluid Mechanics*, Vol. 550, 2006, pp. 413–441. https://doi.org/10.1017/S0022112005008153.

[19] Casalino, D., Romani, G., Zhang, R., and Chen, H., "Lattice-Boltzmann calculations of rotor aeroacoustics in transitional boundary layer regime," *Aerospace Science and Technology*, Vol. 130, 2022, p. 107953. https://doi.org/10.1016/j.ast.2022.107953.

[20] Romani, G., Grande, E., Avallone, F., Ragni, D., and Casalino, D., "Performance and noise prediction of low-Reynolds number propellers using the Lattice-Boltzmann method," *Aerospace Science and Technology*, Vol. 125, 2022, p. 107086. https://doi.org/10.1016/j.ast.2021.107086, sI: DICUAM 2021.

[21] Casalino, D., Grande, E., Romani, G., Ragni, D., and Avallone, F., "Definition of a benchmark for low Reynolds number propeller aeroacoustics," *Aerospace Science and Technology*, Vol. 113, 2021, p. 106707. https://doi.org/10.1016/j.ast.2021.106707.

[22] Chen, H., Zhang, R., and Gopalakrishnan, P., "Lattice Boltzmann collision operators enforcing isotropy and Galilean invariance," , Feb. 21 2017. URL https://patents.google.com/patent/CA2919062A1/en.

[23] Chen, H., Chen, S., and Matthaeus, W. H., "Recovery of the Navier-Stokes equations using a lattice-gas Boltzmann method," *Physical review A*, Vol. 45, No. 8, 1992, p. R5339. https://doi.org/10.1103/PhysRevA.45.R5339.

[24] Yakhot, V., and Orszag, S. A., "Renormalization group analysis of turbulence. I. Basic theory," *Journal of scientific computing*, Vol. 1, No. 1, 1986, pp. 3–51. https://doi.org/10.1007/BF01061452.

[25] Teixeira, C. M., "Incorporating turbulence models into the lattice-Boltzmann method," *International Journal of Modern Physics C*, Vol. 9, No. 08, 1998, pp. 1159–1175. https://doi.org/10.1142/S0129183198001060.

[26] Wilcox, D. C., "Turbulence Modelling for CFD 3rd Edition," *La Canada CA: DCW industries*, 2006.

[27] Launder, B. E., and Spalding, D. B., "The numerical computation of turbulent flows," *Numerical prediction of flow, heat transfer, turbulence and combustion*, Elsevier, 1983, pp. 96–116. https://doi.org/10.1016/B978-0-08-030937-8.50016-7.

[28] Casalino, D., "An advanced time approach for acoustic analogy predictions," *Journal of Sound and Vibration*, Vol. 261, No. 4, 2003, pp. 583–612. https://doi.org/10.1016/S0022-460X(02)00986-0.

[29] Turner, J. M., and Kim, J. W., "Quadrupole noise generated from a low-speed aerofoil in near-and full-stall conditions," *Journal of Fluid Mechanics*, Vol. 936, 2022, p. A34. https://doi.org/10.1017/jfm.2022.75.

[30] Avallone, F., van den Ende, L., Li, Q., Ragni, D., Casalino, D., Eitelberg, G., and Veldhuis, L., "Aerodynamic and Aeroacoustic Effects of Swirl Recovery Vanes Length," *Journal of Aircraft*, Vol. 56, No. 6, 2019, pp. 2223–2235. https://doi.org/10.2514/1.C035552.

[31] O'meara, M., and Mueller, T. J., "Laminar separation bubble characteristics on an airfoil at low Reynolds numbers," *AIAA journal*, Vol. 25, No. 8, 1987, pp. 1033–1041. https://doi.org/10.2514/3.9739.

[32] Ol, M., McCauliffe, B., Hanff, E., Scholz, U., and Kähler, C., "Comparison of laminar separation bubble measurements on a low Reynolds number airfoil in three facilities," *35th AIAA fluid dynamics conference and exhibit*, 2005, p. 5149. https://doi.org/10.2514/6.2005-5149.

[33] Temmerman, L., and Leschziner, M. A., "Large eddy simulation of separated flow in a streamwise periodic channel constriction," *Second Symposium on Turbulence and Shear Flow Phenomena*, Begel House Inc., 2001. https://doi.org/10.1615/TSFP2.2300.

[34] Temmerman, L., Leschziner, M. A., Mellen, C. P., and Fröhlich, J., "Investigation of wall-function approximations and subgrid-scale models in large eddy simulation of separated flow in a channel with streamwise periodic constrictions," *International Journal of Heat and Fluid Flow*, Vol. 24, No. 2, 2003, pp. 157–180. https://doi.org/10.1016/S0142-727X(02)00222-9.

[35] Kurtz, D., and Marte, J., "A review of aerodynamic noise from propellers, rotors, and lift fans," Tech. Rep. 32-1462, Jet Propulsion Laboratory, Jan. 1970. URL https://ntrs.nasa.gov/citations/19700005920.

[36] Williams, J. F., and Hawkings, D., "Theory relating to the noise of rotating machinery," *Journal of Sound and Vibration*, Vol. 10, No. 1, 1969, pp. 10–21. https://doi.org/10.1016/0022-460X(69)90125-4.

Declaration of interests

☒The authors declare that they have no known competing financial interests or personal relationships that could have appeared to influence the work reported in this paper.

☐The authors declare the following financial interests/personal relationships which may be considered as potential competing interests: